ABSTRACT

MILLER, BRENDAN PAUL. Diffusion of Physisorbed Layers and their Connection to MEMS Effectiveness. (Under the direction of Professor Jacqueline Krim.)

The aim of this work is to connect the physics of surface diffusion of a lubricant to Micro-Electro-Mechanical System (MEMS) lubrication. Some hurdles must be overcome in order to make this connection. One must have a way to experimentally measure surface diffusivity. Length scales must be taken into account since the mechanism of lubrication varies from the macro scale to the micro scale and even to the nano scale. Lastly, a theoretical model of lubrication that can conform to MEMS geometry is needed for an accurate prediction.

In the work presented here, I have used different techniques including a quartz crystal microbalance (QCM), a macroscopic tribometer, a micro tribometer, and an atomic force microscope (AFM) to measure the friction of a lubricant on surfaces relevant to MEMS. The QCM method is different from the others aforementioned since it measures the atomic scale friction of a sliding layer in a contact-free environment directly related to surface mobility. The other three methods are a way to measure lubrication over three different length scales.

A surface lubrication model developed by Prof. Donald Brenner incorporates surface diffusion as a mechanism for lubricating a periodic contact. There is a push and pull between the removal of the lubricant from the periodic contact and the replenishment of the lubricant via surface diffusion. A steady-state center concentration can be computed, which is used to determine whether or not lubrication can occur. This model was fit to magnetic hard disc

drives (MHDDs), MEMS, and macroscopic industrial machines, but will work for any system with a periodic contact relying on surface diffusion as the replenishment mechanism.

Two groups of lubricants were studied in this work. Tricresyl Phosphate (TCP), which is a known high temperature additive to industrial oils, was selected since it possesses a low vapor pressure and has been extensively studied by our group. All of the above mentioned techniques were used to study TCP. The other group of lubricants studied were alcohols, specifically pentanol, ethanol, and trifluoroethanol (TFE). These lubricants were studied exclusively with the QCM technique. Alcohols have been shown to lubricate a MEMS device indefinitely as long as an environment of the alcohol vapor surrounds the contact.

The results shown here can be used to directly predict the effectiveness of a lubricant candidate to a MEMS device. Some extra parameters were determined to affect lubrication including contact stress, adhesion, and wetablitiy. These parameters need to be taken into account for future selection of lubricants.

Diffusion of Physisorbed Layers and their Connection to MEMS Effectiveness

by
Brendan Paul Miller

A dissertation submitted to the Graduate Faculty of
North Carolina State University
in partial fulfillment of the
requirements for the degree of
Doctor of Philosophy

Physics

Raleigh, North Carolina

2009

APPROVED BY:

_____	_____
Prof. Jacqueline Krim Chair of Advisory Committee	Prof. Donald W. Brenner
_____	_____
Prof. John E. Rowe	Prof. Thomas P. Pearl

DEDICATION

To all my family and friends, especially my parents, sisters, and Fiancée. I could not have accomplished this without the support of everyone around me.

BIOGRAPHY

Brendan Miller was born in Lancaster, Pennsylvania to Joseph and Stephanie Miller. He was a very inquisitive child and loved to question his parents about anything he may not fully understand. He grew up playing sports and learned valuable life lessons from them. He loves tennis spawning from playing with his father in the street with a makeshift net. This foundation allowed Brendan to play tennis in high school and eventually college. He played saxophone in the high school marching band despite not having a musical bone in his body. Math and physics came easy to Brendan, but he never knew what he wanted to do with that. People would tell him to be an engineer even though he was not exactly sure what that entitled. He switched to a physics major in the first semester at Bloomsburg University in Pennsylvania. Tennis practices for three hours a day gave him structure in college and helped him achieve a 3.7 GPA. He was convinced by some of the physics professors that he should continue his education at a research institution, where, as a complete surprise to Brendan, they would pay for your education and give you a stipend to live off. Not wanting to join the real world he arrived at North Carolina State University as a master's student. He soon realized his love for physics and wanted to push his education to limit.

He moved to Milwaukee, Wi with his future wife, Maria, after graduation for a post doctoral position at the University of Wisconsin – Milwaukee. He stayed in the tribology field learning new surface science techniques furthering his education for the ultimate goal of being a research scientist in the field of alternate energy.

ACKNOWLEDGMENTS

Thanks to everyone in the MURI grant. The atomic force microscopy was performed by Matthew Brukman here at NC State, and the microtribometry was performed by Kathryn Wahl at NRL. Nimel Theodore performed the macroscopic tribometry at NRL. Nimel also mentored me in the all important final year of my graduate career, and for that I am truly grateful. The characterization of tricresyl phosphate and the self-assembled monolayer was performed at NRL. Discussions with Don Brenner, Doug Irving, and Mike Dugger proved invaluable.

I wish to thank all the members of the Nanotribology lab. They have provided a great environment for helping me with my issues and vice versa. This comradery led to an understanding of not only my own work, but everyone else's work as well. Also, I wish to thank my advisor Jacqueline Krim for taking a chance on someone with nominal lab experience but a lot desire for learning.

This work was funded by the AFOSR Extreme Friction MURI Grant No. FA9550-04-1-0381.

TABLE OF CONTENTS

LIST OF TABLES

LIST OF FIGURES

Chapter 1: Introduction

1.1 Friction

Nanotribology is an exciting, growing field with uses varying from understanding fundamental friction mechanisms to lubricating smaller and smaller contacts in MEMS. The name tribology comes from "tribos", which is the Greek word for "to rub", and is the study of friction and wear. Anytime an object is in motion, there is friction present. Even without motion there is still static friction opposing the onset of motion. The friction that is easily thought of is kinetic friction i.e. the friction occurring when two objects are sliding across each other. This is seen in everyday occurrences from rubbing one's hands together to brakes working to slow a car down. The well known macroscopic equation:

$$F = \mu N \qquad (1.1)$$

is known as Amonton's Law[1], where F is the force of friction opposing motion, μ is the coefficient of friction, and N is the normal force. (1.1) implies that the force of friction is proportional to the applied load and independent of the area of contact. This works well for many macroscopic systems, but as one goes to smaller and smaller scales Amonton's law takes a different turn.

Bowden and Tabor made a revolutionary breakthrough in the 1950's. They discovered that the force of friction is only independent of the *apparent* area of contact, and the friction force is in fact proportional to the *true* area of contact[2]. This phenomenon occurs

since microscopic asperities of most macroscopic contacts are the only parts of the two objects in actual contact. As one increases the normal force the apparent area of contact stays the same, but the true area of contact (which is only a fraction of the apparent area of contact) increases. This new situation can be defined as:

$$F = A_{true}\sigma \qquad (1.2)$$

If A_{true} is the true area of contact and σ is the shear stress.

(1.1) and (1.2) are both phenomenological in nature and do not give any insight into the physical mechanism of friction. It was believed that wear was an unavoidable consequence of sliding contacts and thus the physical mechanism behind friction. Work by Tabor and Israelachvili in the 1970's contradicted this thought and showed experimental evidence of friction occurring in a zero-wear environment[3,4]. They used a surface forces apparatus, shown in Fig. 1.1[5], which consists of two cleaved mica sheets cut atomically flat and slid them across one another while measuring the normal and lateral force. Due to the absence of wear the friction between two contacts must therefore originate from another mechanism. That mechanism has been proposed to be phononic friction (sound or heat wave generation) and additionally electronic friction for electrically conductive materials.

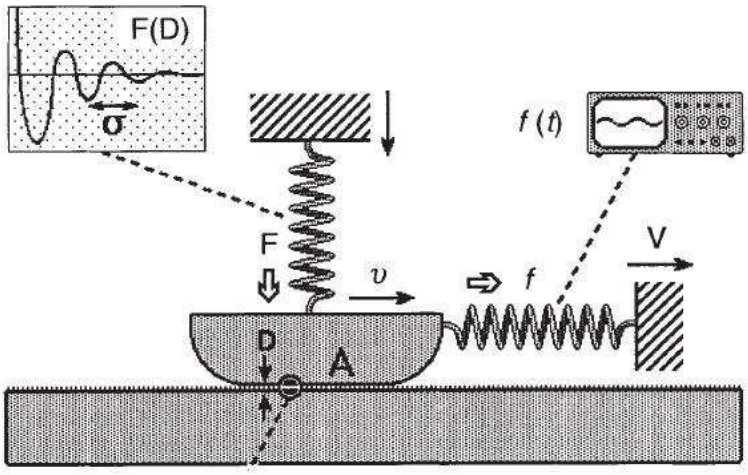

Fig. 1.1 shows a diagram of a surface forces apparatus (SFA) where two atomically flat mica sheets are rubbed together. Measurement of the normal and shear force is allowed via springs. Reproduced from Ref. 5.

Another type of friction is apparent for objects moving through a viscous medium, where the viscosity of the fluid opposes the motion. Instances of viscous friction are a skydiver reaching terminal velocity or a submarine traveling through the water. This force equation can be written as:

$$F = \frac{mv}{\tau} \qquad (1.3)$$

where m and v are the mass and velocity of the object, respectively, and τ is the time that the object's velocity would take to fall to 1/e of its original value if this frictional force was the only acting force. This "τ" will come up again in a surface applicable form and will be referred to as "slip time." The drag coefficient γ equal to m/τ is an important quantity when dealing with the diffusion.

1.2 Diffusion

Diffusion in its simplest form is a net displacement of particles from an area of higher concentration to one of lower concentration by random particle motion and is described by Fick's law[6]. Simply stated Fick's law is defined as

$$J = -D\nabla\phi \tag{1.4}$$

where J is the diffusion flux or the amount of material through an area per unit time, D is the diffusion coefficient, and ϕ is the concentration. The diffusion that this dissertation will deal with is surface diffusion, which is the motion of particles at a solid surface. This process can be thought of as particles hopping between adjacent adsorption sites, shown in Fig. 1.2. Adsorbed atoms have a tendency to rest at the potential energy minima of the underlying solid. The significance of surface diffusion in technological applications ranges from the growth of semiconductor devices for electronics to the refinement of exhaust gases in the automotive industry to the liquid wetting of solid materials to reduce friction[7]. Increasing efforts have been aimed at understanding the physical laws that govern the diffusion of atoms, complex molecules, and particles on solid surfaces.

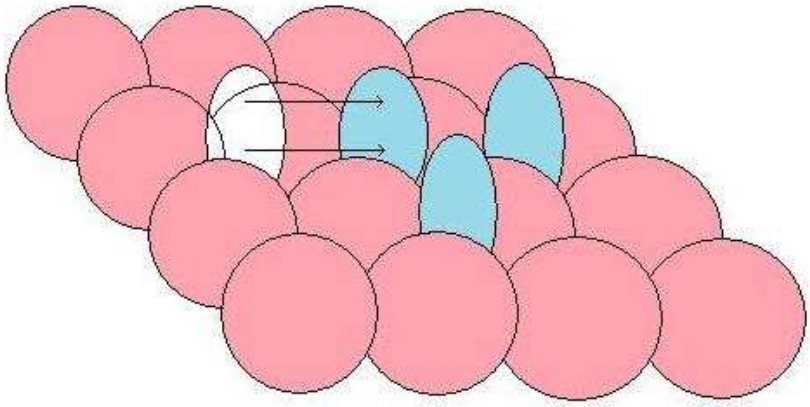

Fig. 1.2 shows the diffusion of an adsorbate from one site (white oval) to another site (blue oval) on a crystalline surface (red circles).

Many of the major fundamentals of surface diffusion under ideal conditions are now well understood due to experimental and computational efforts in recent decades. Some of these experimental methods include scanning tunneling microscopy and field ion microscopy. However, surface diffusion becomes increasingly complicated when the setup consists of non-equilibrium conditions, impurities, or other defects that are typical under real life situations. Numerous experiments have reported that non-equilibrium measurements can produce different results from equilibrium measurements. Also, experiments have shown that impurities can affect surface diffusion i.e. impurities can adsorb preferentially to step edges[7,8], where they may hinder diffusion and initiate non-smooth growth. Surface defects provide preferred adsorption sites for chemi- or physisorbed particles drastically affecting diffusion[9].

Measurements of diffusion reveal a more complete description of adsorbate-substrate interaction and encompass frictional damping and adsorbate-adsorbate interaction. A way to

quantify diffusion is with the diffusion coefficient, *D*, which is measured in area per unit time. An equation for diffusion can be written as:

$$D = D_0 \exp\left(\frac{-E_{diff}}{k_B T}\right) \tag{1.5}$$

where k_B is Boltzmann's constant, T is the temperature, and D_0 is the diffusion prefactor which is the value for D at $T \rightarrow \infty$ or when $k_B T >> E_{diff}$. E_{diff} is the diffusion barrier, which is the range in potential energy laterally. At very low temperatures this equation does not accurately describe diffusion since quantum tunneling dominates. However, when $k_B T$ is on the order of E_{diff}, one obtains for a particle on a 2D plane

$$D = \frac{f_h d^2}{4} \tag{1.6}$$

where f_h is the hopping frequency between sites and d^2 is the mean square site distance. At higher temperatures $k_B T >> E_{diff}$, and Brownian motion occurs where the substrate is not seen by the adsorbates and a 2D gas is observed. Einstein's relation can be written in 2D from Bird[10] as:

$$D = \frac{k_B T}{\eta A} \tag{1.7}$$

where η is the interfacial coefficient of friction and A is the area of contact with the substrate. The friction coefficient η is defined as $\eta = \rho/\tau$ where ρ is the mass per unit area of a particle, cluster of particles, or a 2D film.

Diffusion is, however, highly dependent on not only the mass of the particles, but also the cluster size. A number of theories have thus been reported, which treat progressively

increasing adsorbate coverage that range from treatments of self-diffusion of individual particles[11], (Fig. 1.3a) to self-diffusion of island clusters[12], (Fig. 1.3b) to spreading diffusion within complete monolayers[11,13,14], (Fig. 1.3c) as described next.

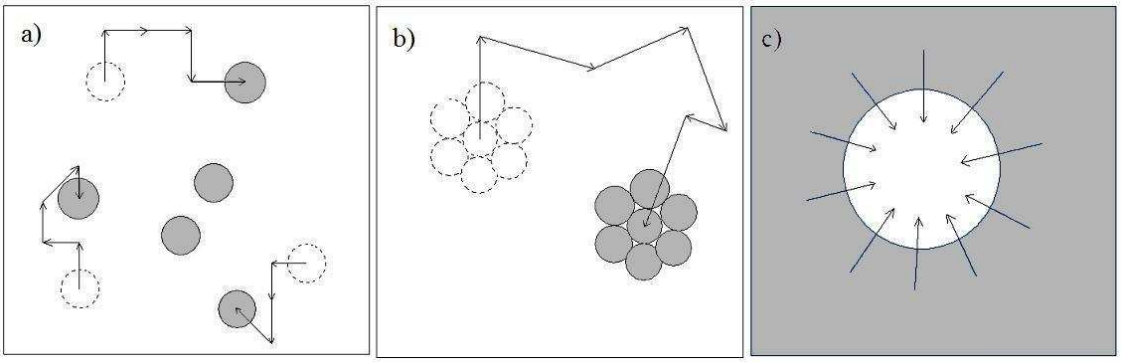

Fig. 1.3 shows a depiction of a) single molecule diffusion, b) island cluster diffusion, and c) spreading diffusion.

The diffusion and spreading coefficients referred to so far are two-dimensional quantities that are defined in an entirely distinct manner from the spreading rate of a macroscopic droplet placed on a surface. Such macroscopic droplets may completely wet, incompletely wet, or not wet surfaces that they are in contact with, and it is common to define a "spreading coefficient" K to gauge whether wetting will occur:

$$K = \gamma_A - \gamma_B - \gamma_{AB} \tag{1.8}$$

The term γ_A is the surface energy or surface tension of the solid, γ_B is the surface tension of the liquid in question, and γ_{AB} is the interfacial tension[15]. If K is positive then the liquid will wet the surface, but if K is negative then it will dewet from the surface. In 1977, Dash employed thermodynamic arguments to demonstrate the correspondence between three types of vapor pressure adsorption isotherms and the three categories of macroscopic wetting

behavior[16]. Dash's correspondence between sub-saturation adsorption behaviors and macroscopic wetting types is depicted in Fig. 1.4 for the cases of (a) "complete", (b) "incomplete" and (c) "nonwetting" behaviors. With increasing coverage adsorbed films may form (a) ever thickening uniform layers, (b) a uniform two-dimensional layer after which all material goes to form a bulk droplet at the bulk saturation vapor pressure, or (c) only trace amounts may condense in advance of bulk droplet formation. Macroscopic wetting characteristics can thus be probed through recording of adsorption data at sub-saturation vapor pressures where droplet formation is *completely inhibited*. A quartz crystal microbalance (QCM) is an ideal tool for studies of film adsorption and wetting at these sub-saturation pressures, including sub-monolayer coverages. The focus here on film spreading and diffusive behavior that is restricted to two dimensions.

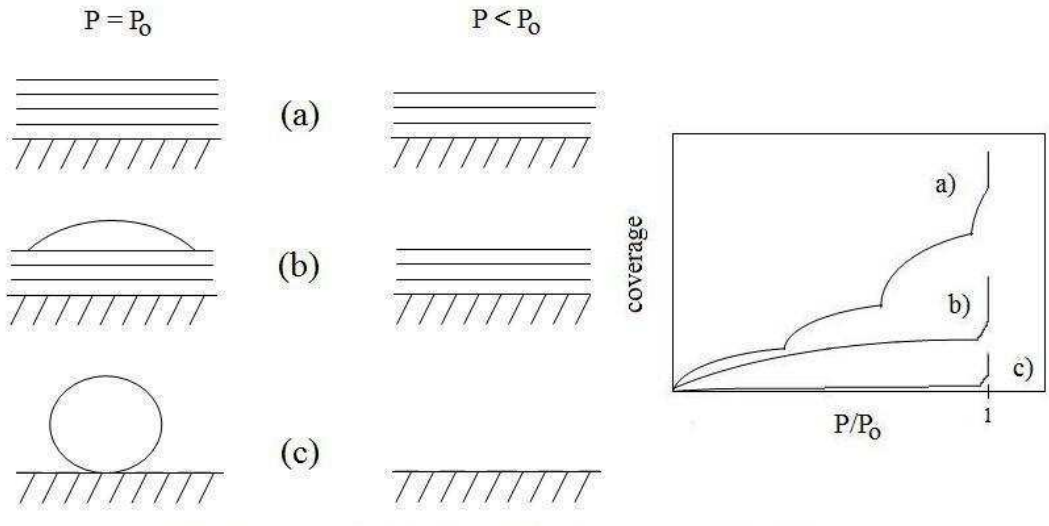

Fig. 1.4 Three types of wetting behavior at and below the saturated vapor pressure P_0, along with their corresponding forms for the vapor pressure isotherm. (a) complete wetting, (b) incomplete wetting and (c) nonwetting.

1.3 Various Diffusion Coefficients

(A) Brownian motion of mobile particles and the windshield wiper effect:

It was recently reported that when a mobile overlayer is present on a metal surface, a MHz transverse oscillation created by a combined quartz crystal microbalance-scanning tunneling microscope (QCM-STM) can produce a clearer tunneling image of the metal surface compared to the same system without oscillation[17]. This observation was attributed to a "windshield wiper" effect in which rapid oscillation at the tip-surface interface created a region below the tip where at least part of the mobile overlayer was wiped away causing a clear image seen in the lower half of Fig. 1.5a. Noise in the STM image for a non-oscillating QCM was attributed to surface diffusion of adsorbate molecules in and out of the region between the tip and substrate. This phenomenon shown in the upper half of Fig. 1.5a is consistent with the fact that the "windshield wiper" effect is absent for non-mobile adsorbates.

To explore the feasibility of this explanation, Brenner and colleagues performed numerical modeling to determine the steady-state concentration of a mobile lubricating overlayer under an oscillating contact due to surface flow[11]. The modeling predicted that a region below the tip with a reduced concentration of mobile overlayer can be maintained by MHz transverse substrate oscillations for a physically realistic range of overlayer diffusion coefficients.

The flow model that Brenner used to describe the QCM-STM dynamics was later extended to an analytic multi-scale expression for effective liquid lubrication of oscillating contacts via surface flow where a fraction of the lubricant is removed from the contact at each cycle[14]. Using a simplified flow model, a unitless scaling quantity *S* was identified that provided a multi-scale measure of the effectiveness of a liquid lubricant replenished via surface flow. The unitless scaling parameter *S* of a reciprocating contact is defined as

$$S = \frac{f\ A_c}{D} \tag{1.9}$$

where f is the repetition frequency that the lubricant is removed, A_c is the contact area scratched free (or partially free) of the lubricant, and D is the lubricant single molecule diffusion coefficient. The lubricant steady-state center concentration C shown in Fig. 1.5b is defined as

$$C(S) = \frac{1}{e^{AS+B}} \tag{1.10}$$

where A and B are quantities dependent on the fraction of lubricant removed per cycle. The red line in Fig. 1.5b is 10% of the lubricant removed and the blue line is 0.1% of lubricant removed per cycle. This model was fit to magnetic hard disc drives (MHDDs), MEMS, and macroscopic industrial machines. It is ideal for liquid lubrication and space application since there is negligible vapor phase and will work for any system with a periodic contact relying on surface diffusion. This model will be used for comparison from hence forward. In order to probe the validity of the approach, Brenner et al used values of the self-diffusion coefficient for a number of systems and found agreement for a large range of length scales.

For the data presented in Fig. 1.5b, realistic values for the frequency and contact area yield 10^{-3} cm^2/s for the removal rate parameter, ($f\,A_c$). A self-diffusion coefficient of 10^{-3} cm^2/s shown however to be vastly insufficient to refill the area scraped free in one cycle, as might be expected intuitively. The self-diffusion coefficient must be approximately 100 – 1000 times greater in order for this to occur. Such values may not be unrealistic for islands of particles, as discussed next.

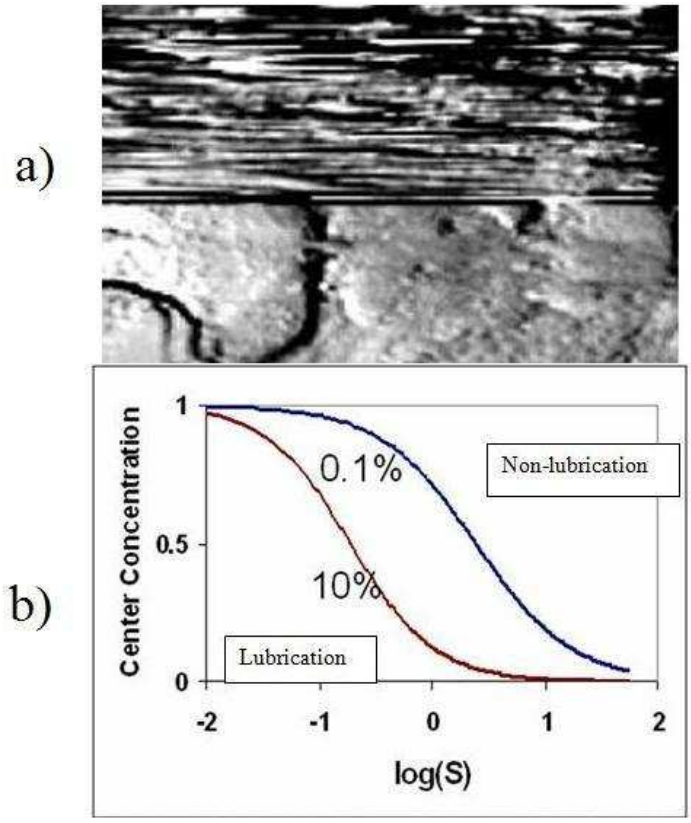

Fig. 1.5 shows the "windshield wiper" effect for a) a non-oscillating QCM (noisy region) and an oscillating QCM (clear region). b) The lubricant steady-state center concentration at the contact for values coinciding to the area of an STM tip and the frequency of a QCM. The red curve corresponds to 10% of the lubricant removed per cycle, and the blue curve corresponds to 0.1% of the lubricant removed per cycle. This was reproduced from Ref. 11.

(B) Brownian motion of islands.

The diffusive and frictional behavior of clusters of particles is distinct from that of their constituent particles, (Fig. 1.3a, b) and can vary dramatically with size. Sliding friction values may drop for clusters of atoms, for example, because the formation of an island generally requires that some or all of the atoms in the layer becomes incommensurate with the substrate. Gold islands of 250 atoms have been routinely observed to diffuse on graphite substrates with surprisingly large diffusion coefficients[18] (D = 1000 cm^2/s and E_d = 0.5 eV compared to single atom values[19] of D = 0.002 cm^2/s and E_d = 0.08 eV) Similar behavior has been reported for other metal clusters as well[20].

Pisov and coworkers have suggested that the diffusive behavior of such islands can be probed by means of QCM via the fluctuation-dissipation relation[12]. In particular, they suggest that the cluster drift mobility can be related to an island diffusion coefficient D_i through the Einstein relation, (1.7) written as $D_i \eta_2 A = k_B T$, to obtain:

$$\tau = \frac{D_i m N}{k_B T} \qquad (1.11)$$

where τ is a measurable quantity of the QCM described in Ch.3, $\rho_2 = mN/A$ is the mass per unit area of an island consisting of N atoms, each with mass m. Island diffusion coefficients which are greater than 10^{-5} cm^2/s should be detectable using a QCM. Given that the islands may be exhibiting self-diffusion at a much greater pace than individual particles, replenishment by means of diffusive motion of islands may become a mechanism for lubrication in cases where the island size is comparable to that of the contact. This mechanism is distinct from the case treated numerically by Brenner and coworkers[11,14] and

that of a spreading film replenishing regions of low density due to internal pressure gradients. An analytic model of the latter phenomenon is described next.

(C) Spreading diffusion of an adsorbed monolayer.

If a small amount of liquid is placed on a surface, then the rate of increase in surface area of the liquid as it spreads into a thin film defines how quickly the area can be replenished. Experimentally obtained values, however, are generally not easy to obtain. Widom and Krim described one such method in 1994, by deriving how the spreading diffusion coefficient D_s can be experimentally determined from slip times and adsorption isotherm information obtained from QCM measurements at sub-saturation vapor pressures[13]. Through substitution of Eq. (6) into Eq. (7) in the paper by Widom and Krim the spreading diffusion coefficient, measured in cm^2/s, is given by:

$$D_S = \tau\left(\frac{\partial\varphi}{\partial\rho_2}\right)_T \qquad (1.12)$$

where ϕ is the film spreading pressure, or the force per unit length exerted on an arbitrary boundary within the film. The spreading pressure can be obtained from adsorption isotherm data, since it can be written in the form:

$$\varphi(P') = \frac{k_B T}{m}\int_0^{P'}\frac{\rho_2(P)}{P}dP \qquad (1.13)$$

where ρ_2 is the mass per unit area adsorbed at pressure P. The spreading diffusion coefficient obtained in this manner provides an intuitive gauge of whether a lubricant is able

to spread back into a contact where it has been scraped off: Simply stated, if D_s= 1 cm^2/s, then a 1 cm^2 area brushed free of an adsorbed film will be replenished by sideways flow in a period of 1 s. For this to occur, it is of course necessary that a reservoir of lubricant be present to resupply the emptied area. This reservoir might be a resupply from the gas phase onto an adjacent area of the surface[21] or perhaps a nearby high surface area region that acts as a sponge or ballast for the film material to flow into the uncovered region.

In the case reported here, the spreading diffusion coefficient D_s, not to be confused with the spreading coefficient K from (1.8), is akin to the rates of spreading seen in the literature. The units of D_s of cm^2/s are equivalent to the rates of spreading and other diffusion coefficients mentioned before. Rates of spreading are seen in the literature to be many orders of magnitude greater than the single particle diffusion coefficient[22,23,24]. These references also show similar measured values of rates of spreading to our experimental results.

Several researchers have in fact developed models for the film replenishment from the vapor phase where lubricant films are scraped off at regular intervals by asperity contacts. Sawyer and Blanchet, for example, developed a model for the lubrication of combined sliding and rolling macroscopic scale based on the condensation of 2D islands of lubricant from the vapor[25]. In related work, Dickrell et al. developed an expression for the vapor lubrication of a reciprocating contact that allows for both time and position dependent film lubrication[26]. Like the Sawyer-Blanchet analysis, the Dickrell et al. expression neglects any contributions from surface flow. While vapor phase replenishment may or may not be a

significant source of lubricant replenishment, depending on the geometry and vapor pressure of the adsorbed film species, sideways surface flow must always be taken into account in a complete treatment of the topic.

1.4 Aims of the Dissertation

A QCM was used to measure the interfacial slip time of various monolayers on surfaces relevant to MEMS i.e. silicon, self-assembled monolayer (SAM), and aluminum. The slip time measured by the QCM was correlated to a diffusion coefficient, through a previously theorized method[12]. The diffusion coefficient is a useful parameter in dealing with MEMS lubrication. The first part of this work deals with the addition of tricresyl phosphate (TCP) to a bound lubricant allowing for surface diffusion of TCP to replenish the contact region. The addition of TCP to a SAM increased the lifetime of a macroscopic tribometer and decreased the coefficient of friction for a nanoscale contact in an atomic force microscope (AFM). Since TCP was seen to possess a higher slip time and therefore higher diffusion coefficient on silicon compared to a SAM, the next logical question is whether or not a liquid layer of TCP will lubricate a silicon contact better without the SAM than with it. This is in comparison to work done by Zabinksi et al. involving bound and mobile phases of a lubricant on a MEMS device[27]. It is experimentally showed here that the addition of TCP to a SAM will extend the lifetime of a tribological contact in agreement with Zabinski. However, TCP lubricated better without the bound SAM differing from Zabinski in this

particular case, but in agreement with a larger diffusion coefficient. All of these results were fit to Brenner's model and showed good agreement but also elucidated some caveats in the model which need to be accounted for when comparing to MEMS. A measurable increase in adhesion with the addition of TCP was witnessed on the nanoscale but not on the macroscale. In addition to the lubrication model, this increase of adhesion and capillary effects in a MEMS contact must be taken into account to ensure lubrication.

The other aspect of this dissertation is the diffusion of various alcohols on these same substrates. Alcohols (specifically propanol and pentanol) have been shown to reduce adhesion in a nanoscale contact[28] and indefinitely extend the lifetime of a MEMS device[29] so long as an environment of alcohol vapor is present. Diffusion coefficients were calculated for the spreading diffusion coefficient D_s from (1.12) and the island diffusion coefficient D_i from (1.13) at full and half monolayer coverages. At full monolayer coverage it is clear to see why alcohols lubricate a MEMS device according to the spreading diffusion coefficient. At half monolayer coverage the island diffusion coefficient drops and values and lubrication is not as obvious.

An alcohol vapor environment is not feasible for many applications of MEMS engineering. The question arises that if the vapor is removed, can the alcohol left on the surface lubricate a device through surface diffusion alone? This work will show that the SAM may be acting as a ballast or sponge holding onto the alcohol post pumpout and allowing surface diffusion of said alcohol into the contact region. Without that SAM, the alcohol will be pumped away completely and the device will fail. An interesting result was

witnessed with trifluoroethanol (TFE) on a SAM which was different than pentanol and ethanol on a SAM. It showed no measurable slip time akin to each of the alcohols on aluminum as well. No slippage or slippage immeasurable by the QCM may translate to a lower surface diffusion coefficient and thus poor lubrication. This supports the notion that without a vapor contribution, TFE will not lubricate a device even with a SAM acting as a reservoir since surface diffusion will be limited.

---

[1] G. Amontons, Mem. Acad. Roy. Sci. 206 (1699).

[2] F.P.D. Bowden and D. Tabor, Friction and Lubrication of Solids, Part I, Oxford University Press, Oxford (1954).

[3] J. N. Israelachvili and D. Tabor, Proc. R. Soc. Lond. A 331, 19 (1972).

[4] J. N. Israelachvili and D. Tabor, Prog. Surf. Membr. Sci. 7, 1 (1973).

[5] B. Bhushan, J. N. Israelachvili, and U. Landman. Nanotribology: friction, wear and lubrication at the atomic scale. Nature, 374:607, (1995).

[6] A. Fick, Phil. Mag. 10, 30 (1855).

[7] J.V. Barth, "Transport of adsorbates at metal surfaces: from thermal migration to hot precursors" Surf. Sci. Rep. 40, 75 (2000).

[8] M. Kalff, G. Comsa, T. Michely, "How Sensitive is Epitaxial Growth to Adsorbates?" Phys. Rev. Lett. 81, 1255 (1998).

[9] M. Giesen, "Step and island dynamics at solid/vacuum and solid/liquid interfaces" Prog. Surf. Sci. 68, 1 (2001).

[10] Bird, R. B., Stewart, W. E., Lightfoot, E. N., "Transport Phenomena," Wiley, New York, (1962).

[11] M. Abdelmaksoud, S.M. Lee, C.W. Padgett, D.L. Irving, D.W. Brenner, J. Krim. Lang. 22, 9606 (2006).

[12] S. Pisov, E. Tosatti, U. Tartaglino and A. Vanossi, Gold Clusters siding on graphite: a possible quartz crystal microbalance experiment? J. Phys. Condens. Matt. 19, 303015 (2007).

[13] A. Widom, J. Krim, Phys. Rev. E. 49, 4154 (1994).

[14] D.W. Brenner, D.L. Irving, A.I. Kingon, C.W. Padgett, J. Krim. Lang. 23, 9253 (2007).

[15] P.G. de Gennes, Rev. Mod. Phys. 57, 827 (1985).

[16] J.G. Dash, Phys. Rev. B 15, 3136 (1977).

[17] B. Borovsky, B.L. Mason, J. Krim, J. Appl. Phys. 88, 4017 (2000).

[18] L. Bardotti, P Jensen, A. Hoareau, M. Treilleux, B. Cabaud, A. Perez, Surf. Sci. 367, 276 (1996).

[19] C.DeW Van Siclen, Phys. Rev. Lett 75, 1574 (1995).

[20] S.C. Wang, G. Erlich, Phys. Rev. Lett 79, 3835 (1999).

[21] A.J. Gellman, Trib. Lett. 17, 455 (2004).

[22] T. Svitova, H. Hoffmann, R.M. Hill, Langmuir 12, 1712 (1996).

[23] A. Chengara, A. Nikolov, D. Wasan, Colloids Surf. A. 206, 31 (2002).

[24] S. Zhu, W.G. Miller, L.E. Scriven, H.T. Davis, Colloids Surf. A. 90, 63 (1994).

[25] W.G. Sawyer, T.A. Blanchet, J. Tribol. 123, 572 (2001); T.A. Blanchet, J.L. Lauer, Y.F. Liew, S.J. Rhee, W.G. Sawyer, Surf. Coat. Technol. 68/69, 446 (1994).

[26] P.L. Dickrell, W.G. Sawyer, J.A. Heimberg, I.L. Singer, K.J. Wahl, A. Erdemir, J. Tribol. 127, 82 (2005).

[27] Eapen, K. C., Patton, S. T., Zabinski, J. S.: Lubrication of MEMS using bound and mobile phases of Fomblin Zdol. Trib Lett 12, 35-41 (2002).

[28] Strawhecker, K., Asay, D. B., McKinney, J., Kim, S. H.: Reduction of adhesion and friction of silicon oxide surface in the presence of n-propanol vapor in the gas phase. Trib. Lett 19, 17-21 (2005).

[29] Asay, D. B., Dugger, M. T., Kim, S. H.: In-situ Vapor-Phase Lubrication of MEMS. Trib Lett 29, 67-74 (2008).

Chapter 2: MEMS Introduction and Literature Review

2.1 Introduction

Microelectromechanical systems (MEMS) have the potential to revolutionize widespread technologies due to their low manufacturing cost and minute power consumption, but tribological issues have slowed progress immensely[30,31,32,33]. As these MEMS devices become smaller and smaller, surface effects like van der Waals and capillary forces dominate, and body forces like gravity and inertia become less significant. Currently, devices which are intended for one-time use, like an accelerometer for airbag deployment, work sufficiently well and are used globally. However, there does not exist a single commercially available device which encompasses surfaces in continual sliding contact. Gears and motors which could enable more complicated movements at the microscale have been rendered useless due to friction and other tribological issues. Conventional lubricants cannot be employed even in theory since the viscosity of the liquid would cause extreme power dissipation canceling one of the main qualities of a MEMS device. Adhesion, specifically stiction (irreversible failure resulting from adhesion) has been shown to be an integral contribution to failure.

There are two types of stiction relevant to MEMS: in-use and release related. Release related stiction, shown in Fig. 2.1, occurs during the release process when the surface tension of the rinse pulls the contacts together, and the restoring force cannot

overcome the adhesive force. In-use stiction occurs when parts come into contact during operation either unintentionally or by design. To eliminate failures from stiction surface modifications are needed. The surface must be made hydrophobic to remove capillary forces, resistive to tribological wear, and stable at high temperatures. Some different proposed solutions to the problem include surface roughening to decrease the area of contact, chemisorbing a solid lubricant to the desired contacts, and utilizing a self-assembled monolayer (SAM) for obtaining a low-surface energy end group.

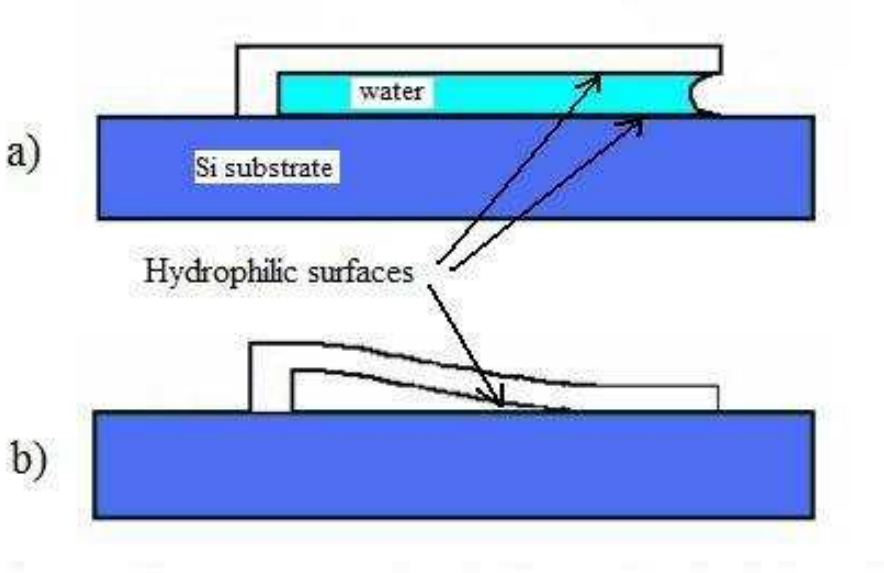

Fig. 2.1 shows an example of release related stiction. a) shows the device as the water evaporates and b) shows the device irreversibly stuck after evaporation.

Surface roughening does not keep adhesion low for enough cycles since tribological degradation occurs over time resulting in either a smooth surface or plowing and wear particle genereation. Hard solid lubricant coatings such as diamond-like carbon

are a promising suggestion, but they have many different issues to work out. Firstly, they do not work well in different environments i.e. graphite works well in air but not vacuum and MoS_2 works well in vacuum but not humid environments. Secondly, solid lubricants change the material properties of the structure which can lead to excess strain causing bending or breaking of the device. Thirdly, they are conductive and can undesirably short out the device. In addition, solid lubricants need to be located at the contacts which cannot always be deposited through line of sight methods. SAMs, while highly effective against release related stiction and easily deposited after the etch phase, have proven ineffective as MEMS lubricants. A bound SAM has no means of replenishment once it is worn away from the contact. Indeed, even the most robust SAMs fail to protect devices from tribological failure for either normal (tapping) contact or sliding (shear) contact[34]. Fig. 2.2 shows a scanning electron microscope (SEM) image of a MEMS friction tester designed at Sandia National Laboratories. Quick failure was characterized as an abrupt stop in the motion of the main shuttle due to the frictional forces and was easily witnessed via an optical microscope. Alternative MEMS lubrication schemes must therefore be developed if progress is to occur.

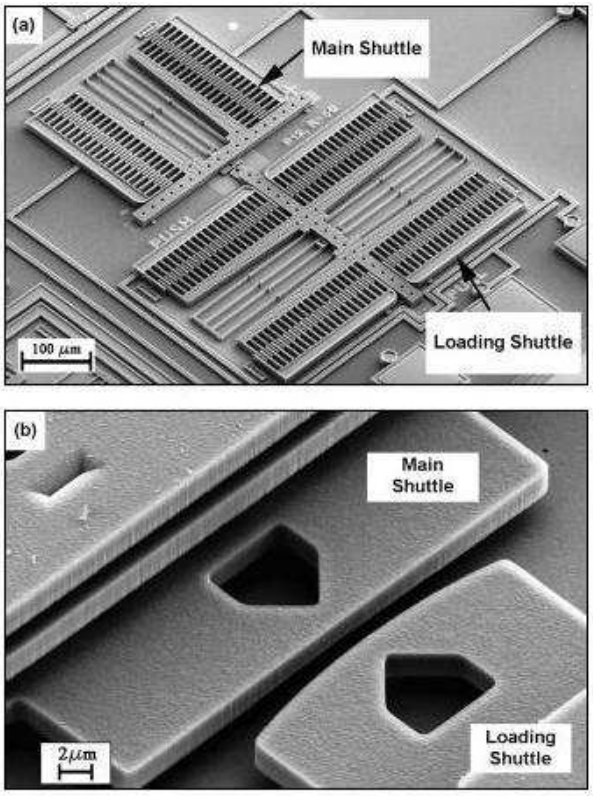

Fig. 2.2 A MEMS friction tester showing a) the comb drive setup and b) the contact used for optically measuring friction coefficients. Reproduced from Ref. 34.

Eapen et al. suggested that the addition of a mobile lubricant in combination with a bound chemisorbed SAM, illustrated in Fig. 2.3, should decrease friction and wear over a longer period of time than either the bound or mobile lubricants alone[35]. The combination of bound and mobile lubricants did indeed extend the lifetime compared to either constituent alone asserting this claim. In that study, the mobile lubricants were delivered to the device surface by liquid immersion. Also, the devices used were large compared to the vast majority of MEMS, and were not affected by release-related capillary effects, so Fig. 2.1 did not apply.

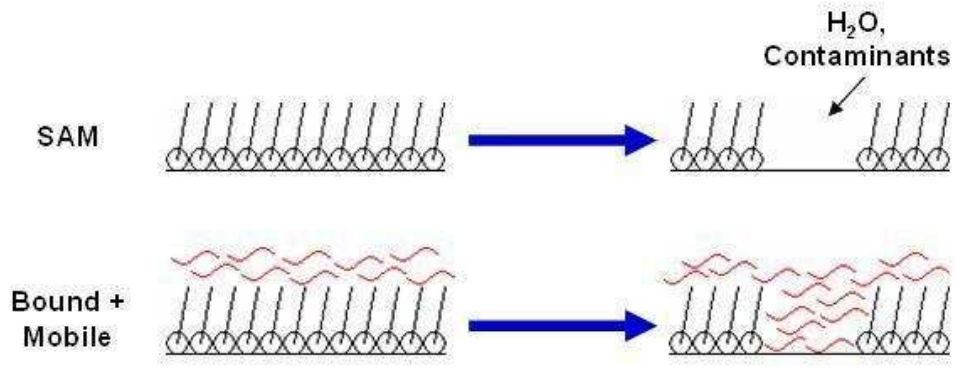

Fig. 2.3 shows the concept of a mobile lubricant (red wavy lines) replenishing the mechanically worn away SAM keeping the device operable for longer periods of time.

Various combinations of dual layer films emerged after the suggestion by Eapen et al[35]. The first was Ren et al. who used steric acid onto a SAM, specifically aminopropyltriethoxysilane (APS)[36]. They witnessed a larger load before failure in a macroscopic tribometry test compared to APS and other SAMs. Perfluoropolyeither (PFPE) was used as the second layer in another dual layer study on APS[37]. These and other comparison studies of dual- and single-layer films were performed, which showed superior wear resistance for the dual layer films using tribometry techniques from the nanoscale to the macroscale[38,39,40]. These layers were all dip-coated and were chemisorbed to one another inhibiting mobility and surface diffusion. Since capillary forces are detrimental to MEMS by causing increased adhesion leading to stiction, this deposition process will not be viable for a wide range of MEMS devices.

One way to prevent capillary bridge formation during lubricant delivery is through vapor phase lubrication such as that proposed by Abdelmaksoud and Krim in

1998[41]. The benefit of a vapor phase lubricant is that the coverage is uniform even with high occluded portions of MEMS devices[42]. In the results presented here a liquid layer is adsorbed to the surface via the vapor phase. Capillary forces are still a concern, however, as the layer can traverse the surface and congregate at contacts. Therefore the amount of adsorbed lubricant was kept to a minimum, and this amount will be further discussed later. Following a deposition of a thin layer of lubricant onto the surface, an appropriate surface diffusion lubricant model was used for different situations regarding the various experimentally determined coefficients discussed previously in chapter 1.

2.2 Prior studies of Tricresyl Phosphate

Illustrated in Fig. 2.4, tricresyl phosphate (TCP), which is a high temperature lubricant additive to industrial oil, has been studied extensively by many research groups including the nanotribology laboratory at North Carolina State University. TCP was seen to form organophosphate lubricants of graphitic carbon on metallic substrates in a matrix of polyphosphate glass after thermal decomposition[43]. This process produced lubricious films for some metals including Fe and Cu but not other metals, including Ni. The thermal decomposition of TCP on Ni is however similar, indicating that this is not the mechanism for lubrication[44]. The addition of TCP was shown to decrease wear for an already effective antiwear additive, oleic acid[45]. Iron phosphates were formed with steel as a counterface on Si_3N_4, and oxides were formed with Si_3N_4-on-Si_3N_4; both were

attributed to decreasing wear. The three TCP isomers (*o*-TCP, *m*-TCP, *p*-TCP) were shown to break down similarly in a tribological contact[46].

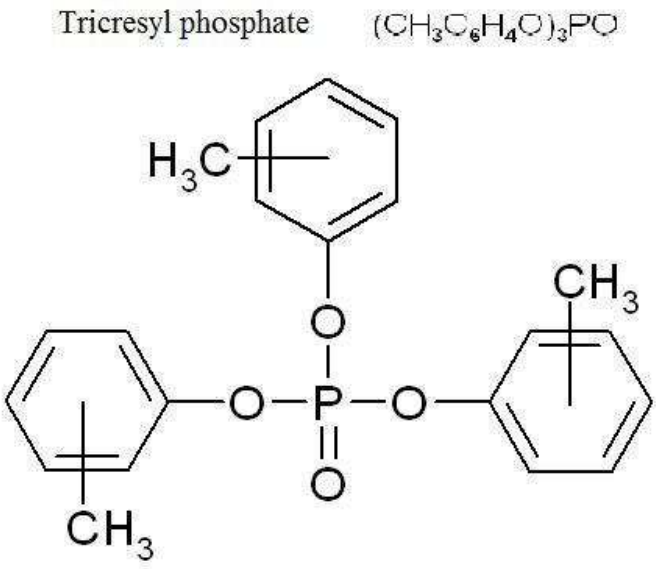

Fig. 2.4 shows the chemical makeup of TCP.

QCM studies using TCP as a vapor phase lubricant on Fe and Cr with and without the presence of O_2 showed a measurable slip time on Fe with O_2 and not with Cr in any case[47,48]. The higher slip times at the atomic scale were linked to good macroscopic tribological performance, and the non-measurable slip times were correlated to poor macroscopic performance. Since then, TCP has been proposed as a lubricant for MEMS due to its high temperature stability and low vapor pressure. QCM studies of TCP on Si and TCP on SAM treated Si were performed showing non-zero values for slip time for each with TCP on Si being the largest[49]. A more in depth study of the mobility of TCP on Si and TCP on a SAM treated surface was performed here using a QCM and other

more traditional tribometers. The value of the slip time of TCP on a SAM was correlated to the computed value of the diffusion coefficient *D* of TCP on a SAM. The value of *D* on Si was inferred from the slip time to fit to Brenner's surface diffusion model to predict the effectiveness of TCP on MEMS.

2.3 Prior studies of alcohols on MEMS

The use of alcohols as a lubricant in the liquid phase stemmed from work showing good lubrication and low wear for silicon oxide and silicon nitride[50]. The idea to reduce adhesion thus increasing tribological properties on the nanoscale originated from atomic force microscope (AFM) studies of n-propanol on silicon oxide[51] and studies of n-alcohols (n=1-12) on SAM treated surfaces[52]. These promising results prompted studies of MEMS friction tester lifetimes using pentanol films at 15% and 95% partial pressure delivered to the surface from the vapor phase[53]. Pentanol allowed the friction tester to run for longer than one billion cycles (compared to a bare silicon device, which fails around six *thousand* cycles in a pentanol free environment) at both partial pressures without failure so long as the device remained exposed to pentanol vapor. The mechanism for lubrication was proposed to be a formation of a high-molecular weight tribo-induced film containing large chains of carbon.

Despite the success of these lubricants, an environment of vapor is needed to replenish the surface of the device for maintaining lubrication, which is not ideal for the

engineering and commercialization of MEMS. In addition, some devices must be open to the surrounding environment to perform their intended task[54]. In the study reported here, the surface diffusion of alcohols was probed to quantify lubricant replenishment and to investigate the possibility of removing the alcohol vapor while still achieving lubrication. The slip time of three different alcohols including pentanol, ethanol, and trifluoroethanol were measured with a QCM on Si, Al, and a SAM-coated surface. The values were measured during an adsorption isotherm and were measured after the vapor was removed. Values for the spreading diffusion coefficient D_s and island diffusion coefficient D_i were inferred from the slip time.

---

[30] Kim, S. H., Asay, D. B., Dugger, M. T.: Nanotribology and MEMS. Nanotoday 2, 22-29 (2007).

[31] Komvopoulos, K.: Adhesion and Friction Forces in Microelectromechanical Systems: Mechanisms, Measurement, Surface Modification Techniques, and Adhesion Theory. J Adhesion Sci Technol 17, 477-517 (2003).

[32] Maboudian, R. Self-assembled monolayers as anti-stiction coatings for MEMS: characteristics and recent developments. Sensors and Actuators A 82, 219–223 (2000).

[33] Mastrangelo, C. H.: Adhesion Related Failure Mechanisms in Micromechanical Devices. Trib Lett 3, 223-238 (1997).

[34] Hook, D. A., Dugger, M. T., Krim. J.: Monolayer Degradation in MEMS friction devices. J App Phys 104, 034303 (2008).

[35] Eapen, K. C., Patton, S. T., Zabinski, J. S.: Lubrication of MEMS using bound and mobile phases of Fomblin Zdol. Trib Lett 12, 35-41 (2002).

[36] S. Ren, S. Yang, Y. Zhao, Micro- and Macro-Tribological Study on a Self-Assembled Dual-Layer Film. Langmuir 19, 2763 (2003).

[37] N. Satyanarayana S.K. Sinha, Tribology of PFPE overcoated self-assembled monolayers deposited on Si surface. J. Phys. D. Appl. Phys. 38, 3512 (2005).

[38] N. Satyanarayana, S.K. Sinha, B.H. Ong, Tribology of a novel UHMWPE/PFPE dual-film coated onto Si surface. Sens. Actuators A 128, 98 (2006).

[39] Y. Mo, M. Zhu, M. Bai, Preparation and nano/microtribological properties of perfluorododecanoic acid (PFDA)–3-aminopropyltriethoxysilane (APS) self-assembled dual-layer film deposited on silicon. Coll. and Surf. A: Physicochem. Eng. Aspects 322, 170 (2008).

[40] B. Yu, L. Qian, J. Yu, Z. Zhou, Effects of Tail Group and Chain Length on the Tribological Behaviors of Self-Assembled Dual-Layer Films in Atmosphere and in Vacuum. Trib. Lett. 34, 1 (2009).

[41] Krim, J., Abdelmaksoud, M.: Nanotribology of Vapor-Phase Lubricants. in Tribology Issues and Opportunities in MEMS, B. Bhushan, ed. 273-284 (Kluwer Academic, Dordrecht, 1998), invited.

[42] Gellman, A. J.: Vapor lubricant transport in MEMS devices. Trib Lett 17, 455-461 (2004).

[43] Forster, N.H., Trivedi, H.K.: Rolling Contact Testing of Vapor Phase Lubricants--Part I: Material Evaluation. Trib. Trans. 40, 421 (1997).

[44] Sung, D., Kim, D., Gellman, A.J.: The surface chemistry of vapor phase lubricants: tricresylphosphate on Ni(100). Trib. Inter. 38, 151 (2005).

[45] Weimin, L., Klaus, E.E., Duda, J.L.: Wear behavior of steel-on-Si_3N_4 and Si_3N_4-on- Si_3N_4 systems with vapor phase lubrication of oleic acid and TCP. Wear 214, 207 (1998).

[46] Sung, D., Gellman, A.J., Thermal decomposition of tricresylphosphate isomers on Fe. Trib. Lett. 13, 9 (2002).

[47] Abdelmaksoud, M., Bender, J., Krim, J.: Bridging the Gap between Macro- and Nanotribology: A Quartz Crystal Microbalance Study of Tricresylphosphate Uptake on Metal and Oxide Surfaces. Phys Rev Lett 92, art. no 176101 (2004).

[48] Abdelmaksoud, M., Bender, J., Krim, J.: Nanotribology of a Vapor-Phase Lubricant: A Quartz Crystal Microbalance Study of Tricresylphosphate (TCP) Uptake on Iron and Chromium. Trib Lett 13, 179-186 (2002).

[49] Neeyakorn, W., Varma, M., Jaye, C., Burnette, J. E., Lee, S. M., Nemanich, R. J., Grant, C. S., Krim, J.: Dynamics of Vapor-Phase Organophosphates on Silicon and OTS. Trib Lett 27, 269-276 (2007).

[50] Gates, R.S., Hsu, S.M.: Silicon Nitride Boundary Lubrication: Lubrication Mechanism of Alcohols. Trib. Trans. 38, 607 (1995).

[51] Strawhecker, K., Asay, D. B., McKinney, J., Kim, S. H.: Reduction of adhesion and friction of silicon oxide surface in the presence of n-propanol vapor in the gas phase. Trib. Lett 19, 17-21 (2005).

[52] Clear, S.C., Nealey, P.F.: Lateral Force Microscopy Study of the Frictional Behavior of Self-Assembled Monolayers of Octadecyltrichlorosilane on Silicon/Silicon Dioxide Immersed in n-Alcohols. Langmuir 17, 720 (2001).

[53] Asay, D. B., Dugger, M. T., Kim, S. H.: In-situ Vapor-Phase Lubrication of MEMS. Trib Lett 29, 67-74 (2008).

[54] McComas, D. J., Miller, G. P., Mitchell, J. N., Pope, S. E., Valek, P. W.: Space applications of microelectromechanical systems: Southwest Research Institute vacuum microprobe facility and initial vacuum test results. Rev Sci Inst 74, 3874-3878 (2003).

Chapter 3: Experimental Details

3.1 Quartz Crystal Microbalance studies of sliding friction and diffusion[55].

Many different experimental techniques were used in this study. QCM data and all sample preparation of Si wafers were performed by myself at NC State. In addition, the macroscopic reciprocating tribometry measurements of tricresyl phosphate (TCP) on Si were performed by myself at the Naval Research Laboratory (NRL). The remaining TCP data reported herein were recorded by MURI team collaborators on samples prepared by myself at NCSU.

The main instrument for data taking in this dissertation is the Quartz Crystal Microbalance (QCM). The QCM has been used as a nanoweighing device for many decades due to the high sensitivity of its resonant frequency enabling measurements of as little as a tenth of a monolayer of adsorption[56]. When a voltage is applied to a piezoelectric, like quartz, it will mechanically deform according to the crystal's orientation with respect to the applied voltage. Since the focus here is on transverse (shear) deformation, the most commonly cut crystal for these purposes is the AT-cut which is oriented at angles of $\theta = 35^0\ 15'$ from normal. When an alternating voltage is applied to the metal electrodes of an AT-cut QCM, it will mechanically oscillate at its fundamental frequency in transverse shear mode at a very high quality factor (Q) of around 10^5. An AT-cut QCM is optimized for frequency stability and low temperature

coefficient at room temperature. Fig. 3.1 shows a diagram of a QCM and a side view of the oscillation. The resonant frequency depends on the thickness of the quartz and can range from 5-10 MHz. This technique assumes a thin, uniformly covered layer which is rigidly attached for a direct proportionality between the negative change in resonant frequency of the QCM to the mass per unit area of the adsorbed film.

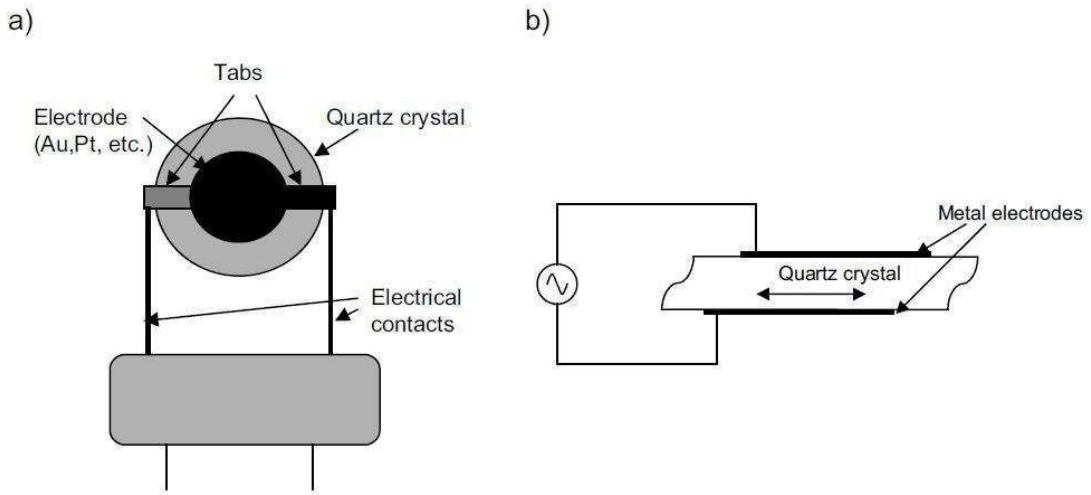

Fig. 3.1 a) top and b) side view of a QCM oscillating in shear mode. Taken from Ref. 57.

3.1.1 Mass Uptake Relationship

Sauerbrey determined a quantitative analysis between the change in its oscillation frequency due to the mass deposited on the QCM electrodes. When an alternating voltage is applied across the electrodes of an AT-cut QCM, standing waves are created from the mechanical shear stress of the piezoelectric if the thickness is an odd integer of

the half wavelength of the induced wave. Then, the fundamental frequency f_0 is given by:

$$f_0 = \frac{v_q}{\lambda} = \frac{v_q}{2t} \qquad (3.1)$$

where v_q is the speed of wave propagation in quartz, λ is the wavelength and t is the thickness of the quartz. Differentiating the logarithm of both sides and using $m_q = \rho_q A t$ one can obtain the change in frequency due to the adsorbed mass per unit area on one side of the crystal:

$$\Delta f = -2 \frac{(m_f / A)}{\rho_q v_q} f_o^2 \qquad (3.2)$$

where ρ_q is mass density of quartz and m_f is the mass of the film substituted for the differential dm_q as long as m_f is much smaller than m_q. The equation is valid as long as the attached film is non-dissipative. An interesting situation arises when the adsorbed film is not rigidly attached.

3.1.2 The Quality Factor

While measuring the change in amplitude of the oscillating signal one can measure the dissipation arising from an adsorbed layer and relate that to the film's sliding friction. This technique was pioneered in 1988 by impedance calculations[57]. It was shown that if the shear stress is below 10^3 N/m^2 between the substrate and the film, then

the layer will slip enough to be detectable by the QCM through frequency and amplitude measurements. This dissipation is related to the quality factor Q mentioned before which is defined as

$$Q = 2\pi \frac{\text{Total Energy in one cycle}}{\text{Energy lost in one cycle}} \tag{3.3}$$

It is clear that the dissipation is related to the inverse quality factor Q^{-1}. There is inherent dissipation from the quartz, and any additional dissipation from an adsorbed film can be added directly

$$\frac{1}{Q} = \frac{1}{Q_q} + \frac{1}{Q_f} \tag{3.4}$$

What follows is a derivation of the acoustic impedance of the situations arising from an adsorbed film and how it can be related to the interfacial slippage, or sliding friction.

3.1.3 Acoustic Impedance of a Viscous Film

Consider a flat surface oscillating in plane with velocity $u = u_0 e^{-iwt}$ with an adsorbed film of thickness d, with bulk density ρ_{3f} and bulk viscosity η_{3f}, lying on top. The oscillatory motion of the surface will cause shear waves to propagate through the film's z-direction normal to the surface. Taking the x-direction to be parallel to the motion of the surface, the Navier-Stokes equation for a viscous, incompressible fluid can describe the adsorbed film by

$$\rho_{3f} \frac{\partial \upsilon_x(z,t)}{\partial t} = \eta_{3f} \frac{\partial^2 \upsilon_x(z,t)}{\partial z^2} \quad (3.5)$$

where the x-direction is in line with the motion of the substrate. The subscript "f" refers to the film ("v" will refer to the vapor), and the subscript "3" refers to the 3D, or bulk values ("2" will refer to the 2D, or surface values). The solution to (3.5) for a frequency *f* under the assumption that the film does not slip at the interface is given by

$$\upsilon_x(z,t) = u(t) \frac{\cos k(d-z)}{\cos(kx)} \quad (3.6)$$

where $k=(1+i)(\omega\rho/2\eta)^{1/2}$ is the dispersion relation. The acoustic impedance, $Z = \sigma_{zy}/v$, can be obtained from the stress tensor component $\sigma_{zy} = \eta(\delta v/\delta z)_{z=0}$ written as

$$Z_f = R_f - iX_f = \eta_{3f} k \tan(kd), \quad where \quad k^2 = i\frac{\omega\rho_{3f}}{\eta_{3f}} \quad (3.7)$$

The real (resistive) component of Z_f relates to the energy dissipation, while the imaginary (reactive) component relates to the inertia of the oscillator.

It has been shown[58] that the total impedance is related to the frequency and quality factor shifts of the QCM by

$$\delta\left(\frac{1}{Q}\right) = \frac{2R_{tot}}{\omega\rho_q t_q}, \qquad \delta\omega = \frac{X_{tot}}{\rho_q t_q} \quad (3.8)$$

where ρ_q and t_q are the density and thickness of quartz. These equations would be a factor of two higher if both sides of the QCM are exposed to the film. In the thin film

limit, where $|kd| \ll 1$, $\tan(kd)$ reduces to *kd* and the real part of Z_f vanishes reducing the acoustic impedance to

$$Z_f = -iX_f = -i\omega\rho_{3f}d = -i\omega\rho_{2f} \quad (3.9)$$

Substituting (3.9) into (3.8) produces the Sauerbrey result for the mass-frequency relationship given by (3.2).

3.1.4 Acoustic Impedance of a 3-Dimensional Gas

When the QCM is exposed to a gaseous environment, the acoustic impedance introduced to the oscillator results from the shear impedance of the gas. If adsorption from the vapor phase occurs, then the acoustic impedance introduced has an additional component from the mass uptake. Consider the case when there is only gas damping and no adsorption. The acoustic impedance to shear wave propagation is given by

$$Z_v = R_v - iX_v = (1-i)\sqrt{\pi\rho_{3v}\eta_{3v}f} \quad (3.10)$$

Substituting (3.10) into (3.8) one can calculate frequency shifts and $\delta(1/Q)$. However, at low pressures, τ_r (time for excess particle momentum to relax after collision with the vibrating crystal) of the gas particles becomes similar to the period of oscillation. The gas cannot be regarded as a simple viscous fluid but must be looked upon as viscoelastic. Its viscosity now becomes a function of frequency where

$$\eta_{3v}^{*} = \frac{\eta_{3v}}{1 + i\omega\tau_r} \quad (3.11)$$

The resistance and reactance of Z_v^* of the viscoelastic gas are

$$R_v^* = \sqrt{\pi\rho_{3v}\eta_{3v} f}\ \sqrt{\frac{\omega\tau_r}{1+(\omega\tau_r)^2}\left(\sqrt{1+\frac{1}{(\omega\tau_r)^2}}+1\right)} \tag{3.12}$$

$$X_v^* = \sqrt{\pi\rho_{3v}\eta_{3v} f}\ \sqrt{\frac{\omega\tau_r}{1+(\omega\tau_r)^2}\left(\sqrt{1+\frac{1}{(\omega\tau_r)^2}}-1\right)}$$

For pressures higher than 300 Torr, $\omega\tau_r \langle\langle 1$, the gas does not behave viscoelastically, so the gas can be regarded as a simple viscous fluid.

3.1.5 Separation of Film and Vapor contributions

Now consider the case of adsorption occurring from the vapor phase. The shear waves produced by the QCM will diffuse through the film and into the surrounding gas. The acoustic impedance in this environment will now have contributions from both the adsorbed film and the vapor. Assuming a no-slip (no energy dissipation) condition at the film-substrate boundary, the acoustic impedance is given by

$$Z_{fv} = Z_{3f} \tanh(\Psi + \gamma d)$$

where,

$$\begin{aligned} \tanh(\Psi) &= \frac{Z_{3v}}{Z_{3f}} \\ Z_{3v} &= (1-i)\sqrt{\pi\rho_{3v}\eta_{3v} f} \\ Z_{3f} &= (1-i)\sqrt{\pi\rho_{3f}\eta_{3f} f} \\ \gamma &= Z_{3v} = (1-i)\sqrt{\frac{\rho_{3f}\omega}{2\eta_{3f}}} \end{aligned} \tag{3.13}$$

Again, assuming a thin film limit of $|kd| \ll 1$, then the acoustic impedance simplifies to

$$Z_{fv} = -i\omega\rho_{2f}\left[1 - \left(\frac{Z_{3v}}{Z_{3f}}\right)^2\right] + Z_{3v} \quad , \quad |kd| \ll 1. \tag{3.14}$$

Since the acoustic mismatch factor $\left[1-\left(\frac{Z_{3v}}{Z_{3f}}\right)^2\right]$ is close to unity in many cases, (3.14) can be additionally simplified to

$$Z_{fv} = -i\omega\rho_{2f} + Z_{3v} = Z_f + Z_v \tag{3.15}$$

The damping effects of both the film and the gas vapor on the QCM can now be broken apart and one can write the frequency and quality factor shifts separately as

$$\delta(\omega) = \delta(\omega)_f + \delta(\omega)_v = \frac{X_f}{\rho_q t_q} + \frac{X_v}{\rho_q t_q} \tag{3.16}$$

$$\delta\left(\frac{1}{Q}\right) = \delta\left(\frac{1}{Q}\right)_f + \delta\left(\frac{1}{Q}\right)_v = 0 + \frac{R_v}{\omega\rho_q t_q}$$

3.1.6 Damping from Interfacial Slippage of an Adsorbed Layer

The effect of film slippage on the mechanical impedance presented to the QCM was calculated[59]. An additional impedance $1/\eta_2$ from a sliding film in parallel to the no-slip case earlier will arise from energy dissipation due to interfacial friction of the film. The total acoustic impedance from a slip condition is then given by

$$\frac{1}{Z_{tot}} = \frac{1}{\eta_2} + \frac{1}{Z_{fv}} \tag{3.17}$$

Solving for the dissipative and reactive terms gives

$$\frac{X_{tot}}{R_{tot}^2 + X_{tot}^2} = \frac{\omega\rho_2 + X_v}{R_v^2 + \left(\omega\rho_2 + X_v\right)^2} \tag{3.18}$$

$$\frac{R_{tot}}{R_{tot}^2 + X_{tot}^2} = \frac{R_v}{R_v^2 + \left(\omega\rho_2 + X_v\right)^2} + \frac{1}{\eta_2}$$

This approach is a small modification to the original derivation by Krim and Widom, where

$$Z_{tot} = Z_v + \frac{Z_f \eta_2}{Z_f + \eta_2} \tag{3.19}$$

was used in place of (3.17). In the low vapor density limit, the two approaches give identical results. However, as the vapor density increases, the Bruschi and Mistura approach gives a 10% - 15% correction to the Krim and Widom approach.

To calculate the slip time, τ, one can solve for η_2 from (3.18) and use the relation

$$\tau = \frac{\rho_{2f}}{\eta_2} \tag{3.20}$$

where τ is the time that the total film momentum takes to fall to 1/e of its original value if the substrate were to stop abruptly. It is to be noted that τ is an average value over the entire film, since not all of the particles are sliding the same amount at any given time.

From (3.8) and (3.19) one can use the measured change in inverse quality factor and frequency shift to calculate the total impedance Z_{tot} and from that the slip time and

interfacial slippage. For a sliding adsorbed film without the surrounding vapor, the determination of τ becomes simpler. The resistive and reactive components of Z_2 are

$$R_2 = \frac{\rho_2 \omega^2 \tau}{1+\omega^2\tau^2} \qquad (3.21)$$
$$X_2 = \frac{\rho_2 \omega}{1+\omega^2\tau^2}$$

Plugging in (3.21) into (3.8) and dividing one can obtain

$$\delta\left(\frac{1}{Q}\right) = 2\tau\delta\omega \qquad (3.22)$$

It is clear to see that in order to determine interfacial slippage, one must measure the quality factor shifts and resonance frequency shifts simultaneously. To accomplish this task the quality factor shifts must be quantified. What follows is an analysis of how the amplitude of oscillation can be used to measure the change in quality factor.

3.1.7 Experimentally Observing Quality Factor

The equation of motion for a damped driven harmonic oscillator, and its analogous electrical equation are

$$m\frac{d^2x}{dt^2} + b\frac{dx}{dt} + kx = F_0 \cos(\omega t) \qquad (3.23)$$
$$L\frac{d^2q}{dt^2} + R\frac{dq}{dt} + \frac{1}{C}q = V_0 \cos(\omega t)$$

where m is the total mass of the crystal and film, b is the damping constant, and $\sqrt{k/m}$ the natural frequency of the crystal. These equations show a connection between the mechanical quantities with the electrical equivalents in a circuit containing L, R, and C in

series with an alternating emf. Substituting the solution of $x = A\cos(\omega t - \phi)$ into (3.23) one obtains

$$A(\omega) = \frac{F_0}{\sqrt{\left(k - m\omega^2\right)^2 + c^2\omega^2}} \tag{3.24}$$

with the phase angle as

$$\phi = \arctan\left(\frac{c\omega}{k - m\omega^2}\right) \tag{3.25}$$

where *A(ω)* is a mechanical amplitude (in meters) of oscillation. Using $\omega_0 = \sqrt{k/m}$ and $Q = \frac{m\omega_0}{c}$, (3.24) can be rewritten as

$$A(\omega) = \frac{F_0 / m}{\sqrt{\left(\omega_0^2 - \omega^2\right)^2 + \left(\frac{\omega_0\omega}{Q}\right)^2}} \tag{3.26}$$

A simplification occurs when the QCM is driven at its resonance frequency. Therefore, (3.26) becomes

$$A(\omega_0) \cong \frac{F_0}{m}\left(\frac{Q}{\omega_0^2}\right) \tag{3.27}$$

The change in the amplitude with frequency and the change in amplitude with quality factor are shown to be

$$\frac{\partial\left(\frac{1}{A}\right)}{\partial\left(\frac{1}{Q}\right)} = \frac{m}{F_0}\omega_0^2 \quad \textit{and} \quad \frac{\partial\left(\frac{1}{A}\right)}{\partial\omega} = \frac{m}{F_0}\left(\frac{\omega_0}{Q}\right) \tag{3.28}$$

Substituting the experimental values, $\omega \approx 10^8$ Hz and $Q \approx 10^5$, one can obtain

$$\frac{\partial\left(\frac{1}{A}\right)}{\partial\left(\frac{1}{Q}\right)} \cong 10^{13} \frac{\partial\left(\frac{1}{A}\right)}{\partial(\omega)} \tag{3.29}$$

This illustrates that changes in the mechanical amplitude of vibration are independent of changes in frequency. Since the voltage of the oscillating signal is proportional to the mechanical oscillation at the surface[60], amplitude changes in the voltage output may be used to directly measure changes in the quality factor.

Measuring the QCM amplitude and ring down decay curves are two ways to monitor ΔQ^{-1}. Using (3.10) one can use a gas like N_2 or He in the high pressure range to get a proportionality constant between $\partial(1/A)$ and $\partial(1/Q)$ since neither gas will adsorb onto the QCM at room temperature. Fig. 3.2 shows a typical N_2 calibration from this work with the measured $\delta(1/A)$ of the output signal vs. pressure and $\delta(1/A)$ vs. $\delta(1/Q)$. The conversion from pressure to $\delta(1/Q)$ can be calculated from the ideal gas law and plugging R from (3.10) into (3.8). This graph shows a linear relationship allowing for future amplitude shifts on a calibrated QCM to be converted to quality factor shifts for layers adsorbed onto the surface[61]. If gases cannot be used to calibrate the QCM (like at cryogenic temperatures where He will form a liquid on the surface) then a ring down technique must be implemented[62].

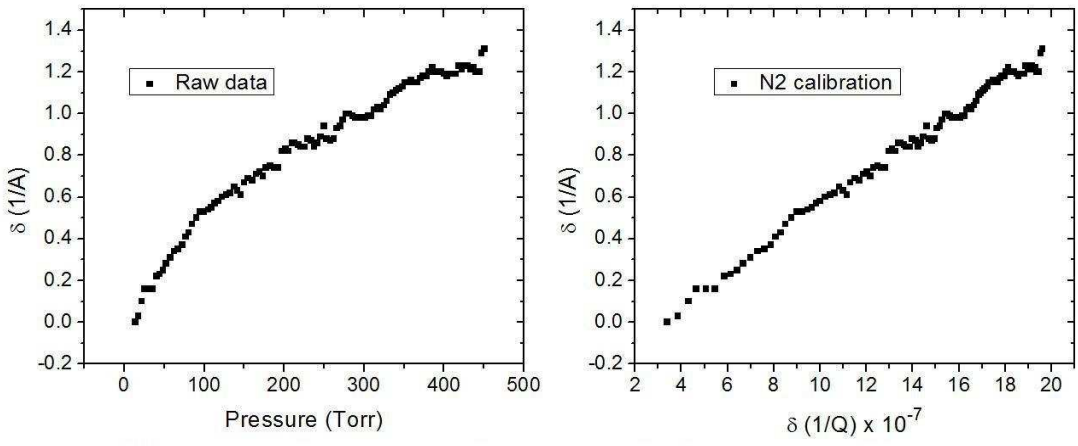

Fig. 3.2 shows the raw data for the inverse amplitude vs. pressure and the inverse amplitude vs. the inverse quality factor for the same sample calibration of nitrogen gas. A clear linear relationship is seen between the inverse quality factor and the inverse amplitude. Data taken from file 9-19-08n2.txt

When power is switched off to the QCM, the voltage at the electrodes decays exponentially as

$$A(t) = A_o e^{-t/\tau} \sin(\omega t + \phi) \tag{3.30}$$

where A_o is the driven amplitude, τ is the decay time constant, and ϕ is the phase. The inverse quality factor is related to τ as

$$\frac{1}{Q} = \frac{2}{\omega\tau} \tag{3.31}$$

Both ω and *1/Q* can be measured from a numerical fit to (3.30). All of the calibrations implemented in this study were used via N_2 calibration curves.

3.1.8 Applications of a QCM

a) Slip time comparison:

The slip time of a sliding layer can be a useful tool for comparing one monolayer on various substrates, different monolayers on the same substrate, or even the same monolayer at different coverages and in different phases. As such was the case of liquid versus solid monolayers of Kr on Au, where the solid monolayers possessed a larger slip time (corresponding to a lower coefficient of friction) than the liquid monolayers[63]. In a modeling effort using phonons as the dissipative mechanism, this counterintuitive result was attributed to a more commensurate liquid layer with the substrate than the solid layer. Bruschi et al. in Fig. 3.3 showed an immediate transition from a pinned monolayer to a sliding one not only with an increase in the crystal amplitude but also an increase in coverage[64].

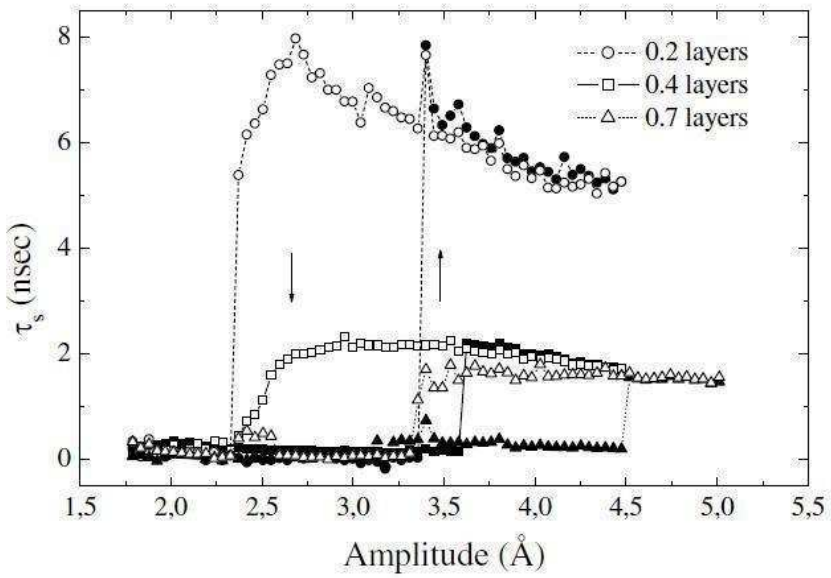

Fig. 3.3 shows the slip time τ as a function of amplitude showing a discrete jump in the slip time from a no-slip condition to a slip condition with increasing amplitude. Reproduced from fig. 2 in Ref. 64.

A comparison to macroscale phenomena was seen with QCM studies of tricresyl phosphate (TCP) adsorbed on Fe and Cr in the presence of oxygen. Two distinct behaviors were seen on the atomic scale showing a slip time value of zero for TCP/Cr and a non-zero value for TCP/Fe. These results were correlated to the macroscale where TCP/Cr contacts exhibit poor tribological properties and TCP/Fe contacts demonstrate very low friction coefficients. A look at these situations has provided a unique perspective on the fundamentals of friction at the atomic scale, but how can a QCM be used to directly measure applicable quantities?

b) Contact replenishment:

For liquid lubrication to occur in a real contact the liquid (or monolayer in this case) must be able to diffuse into the contact area which was once wiped clear of

lubricant. Clearly, the amount of surface diffusion is critical to determine the time for surface replenishment to occur. The rate of increase in surface area of a drop of liquid in contact with a surface which it can wet depends on the interfacial friction and the film spreading pressure, ϕ, obtainable from an integration of the vapor pressure isotherm. Defining a spreading diffusion coefficient as

$$D_S = \tau\left(\frac{\partial\varphi}{\partial\rho_2}\right)_T \tag{3.32}$$

which is measured in area per unit time and can be experimentally calculated. The QCM is uniquely suited to probe these conditions. Values of D_s range from 0.2 - 2 cm^2/s for liquid nitrogen and krypton on gold.

A different lubrication model involving the single particle diffusion *D* which is not directly measured by the QCM due to island formation at low adsorbent coverages, was developed to span a wide range of cyclical contacting systems from magnetic hard disk drives (MHDD) to micro-electro-mechanical systems (MEMS) to industrial machines. This model incorporated the area and frequency of contact, *D*, which can have values of 10^{-3} cm^2/s at room temperature, and the fraction of lubricant removed per stroke. It explained the need for an oil mist with industrial machines, which cannot rely on surface diffusion alone and the theoretical size limitations of MHDDs. A QCM with a mobile lubricant adsorbed onto the surface in conjunction with a scanning tunneling microscope (STM) showed that clearer images from the STM can be obtained while the QCM is oscillating. The top half of Fig. 1.5a showed an STM image of a non-oscillating

QCM, and the bottom half shows an image while oscillating. This situation was explained by this model as a non-lubricating regime where the lubricant does not have enough time to diffuse into the contact due to the MHz oscillations of the QCM. A non-lubricating regime is ideal in this case since the mobile lubricant is getting in the way of the STM tip.

c) A QCM in contact:

A limitation of many other nanotribological devices is their contacting speed. For an atomic force microscope (AFM) or a surface forces apparatus (SFA) one might expect nanometer resolution but only a top lateral speed of up to 10 microns per second. Higher speeds many orders of magnitude greater than that are needed to accurately portray technical situations. The QCM's surface, however, can easily reach speeds in the tens of cm/s and even a few m/s with higher frequency oscillators. The STM-QCM situation was the first QCM-probe technique used to look at friction. Since then a number of probes have arisen in connection to the QCM. Specifically, a sphere with a radius of 3.5mm was used in contact with a QCM via a piezoactuator. Another QCM-probe technique involved a nanoindenter possessing the ability to accurately quantify the normal force and area of contact. Having a 0.5 mm radius of curvature tip, no slippage occurred in this situation. However, the contact was well defined and the possibility of slip being observed with other QCM-probe techniques was assured.

Microparticles have been utilized with a QCM to determine the force of adhesion and the strength of the bond. Breaking of the bond was witnessed acoustically by increasing the drive voltage and was dependent on the size of the particle and the strength of the bond. Using an optical microscope, latex spheres have been observed to traverse the surface of an oscillating QCM independent of gravity. Static and kinetic friction play an integral role in determining when bonds break and how far these spheres can move.

d) Measurement of electronic friction:

Electronic friction has been theorized to play an integral part of energy dissipation in a conducting contact. The theory is that energy is transmitted to conduction band electrons while in sliding contact before being transferred to the bulk as phonons. The first instance of an experimental measurement of this theorized electronic friction occurred while using a QCM with a superconductive electrode. Krim et al. in 1998 and 2006 used various gases (N_2, He, and H_2O) adsorbed on liquid He-cooled Pb electrodes to observe the change in slip time at the superconductive transition[6566]. In this case the friction coefficient decreased by a factor of two while in the superconductive regime where electronic portion of friction is absent. An interesting phenomenon has been observed recently on the macroscale with steel sliding on a high temperature superconductor (Yttrium Barium Copper Oxide- YBCO)[67] sparking new questions about the fundamentals of friction and making the QCM a unique tool for nanotribology.

3.2 Macroscopic Reciprocating Tribometry performed at the Naval Research Laboratory:

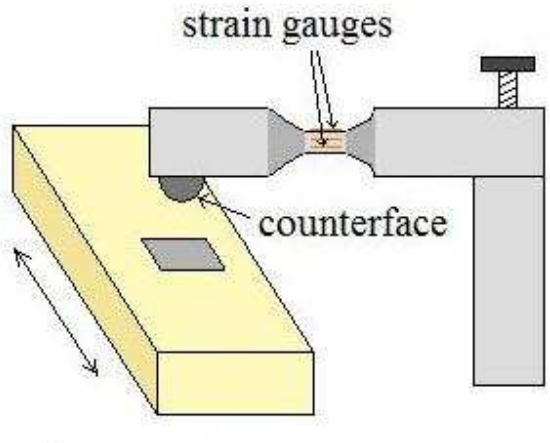

Fig. 3.4 shows an illustration of the experimental setup for the macroscopic reciprocating tribometer. The calibrated strain gauges measure the normal and lateral force while the stage oscillates back and forth.

Macroscopic sliding friction tests were performed on a homebuilt reciprocating tribometer with computer operated translation stages in an ambient environment with temperatures in the range of 23-26°C and a relative humidity of 35-42%. The strain gauges on the counterface arm shown in Fig. 3.4 were measured with a Wheatstone bridge and calibrated by hanging known weights at the counterface for the normal load calibration and using a pulley system for the lateral load calibration. A schematic of a Wheatstone bridge is shown in Fig. 3.5. Using Kirchhoff's laws one can use the voltage difference at V to calculate the resistance of X, which varies with strain. Loads of 0.5 N were applied to a spherical sapphire counterface (radius 3.175 mm), resulting in mean Hertzian contact stresses of 0.35 GPa. Each sample oscillated against the sapphire

counterface for 100 cycles along a 5 mm track at a rate of 1 mm/s in ambient laboratory conditions. Lateral force data were collected and averaged per sliding cycle and reported as friction coefficient (lateral/normal force). In addition, higher loads of 1 N and 2 N were performed for one specific case only.

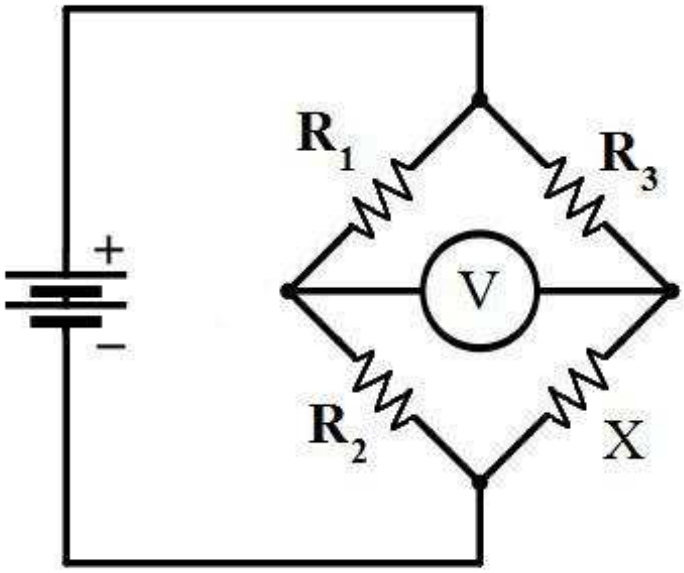

Fig. 3.5 shows a schematic of a Wheatstone bridge used for determining mechanical strain.

Similarly, a silicon counterface was used on a TCP coated sample without the bound lubricant. Various loads from 0.3 – 1 N were applied to the counterface (radius 3.175 mm), resulting in mean Hertzian contact stresses of 0.23 – 0.35 GPa. Each sample oscillated against the Si counterface for a maximum of 1000 cycles (or until failure) along a 2mm track at a rate of 1 mm/s in ambient conditions. The counterface and wear

track were optically imaged using a white light interferometer. Wear scars (or lack thereof) were imaged and recorded for certain characteristic data runs.

3.3 Microscopic Reciprocating Tribometry performed at the Naval Research Laboratory:

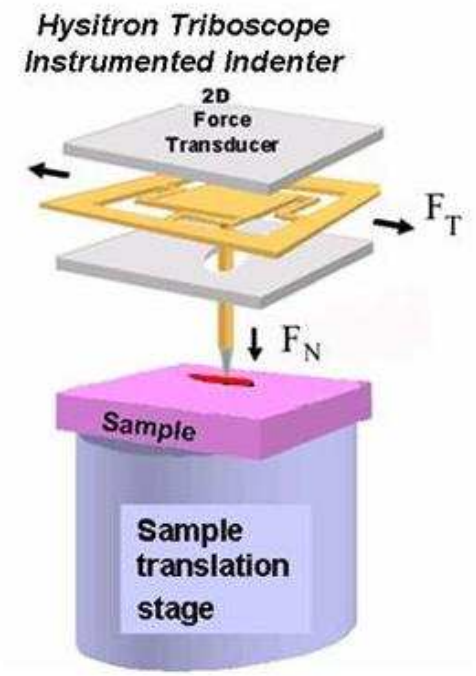

Fig. 3.6 shows an illustration of the setup for the micro-tribometer. The sample stage oscillated forward and backward creating a reciprocating contact.

Microscopic friction tests were completed in a controlled environment of 30-50% relative humidity and a temperature range of 22-25°C using a scanning nanoindenter (Hysitron Triboscope) illustrated in Fig. 3.6 that utilizes a two dimensional electrostatic driven force transducer and capacitive displacement sensing to simultaneously apply normal force while measuring lateral force during sliding. In these measurements, a 400

µN load was applied to a parabolic polished diamond counterface, ~8 µm radius, resulting in a mean Hertzian contact stress of ~1.8 GPa. The tip oscillated for 40 cycles along an 8 µm track at a rate of 4 µm/s.

3.4 Atomic Force Microscopy performed at North Carolina State University:

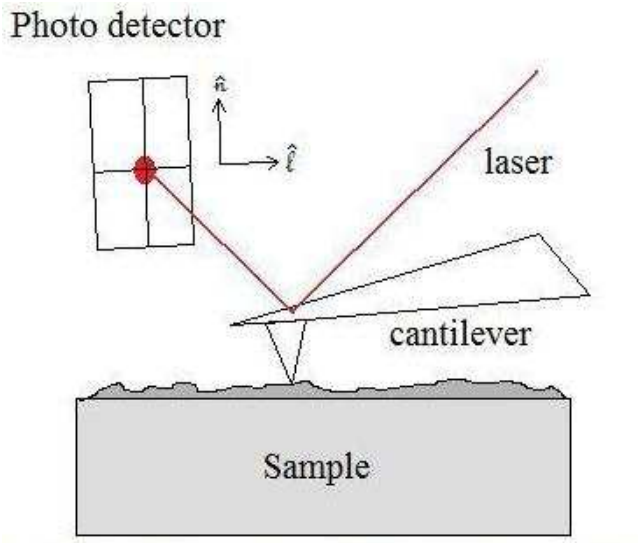

Fig. 3.7 shows an AFM in lateral force mode. The laser deflection in normal and lateral directions is used for frictional force calibration.

Friction behavior was measured with an Atomic Force Microscope (AFM) (Asylum Research, Santa Barbara, CA) illustrated in Fig. 3.7 under ambient conditions at 22°C and 44% relative humidity. Olympus OMCL-RC800 rectangular (20 x 200 micron) SiN levers with pyramid silicon nitride tips (Si_3N_4, Olympus, Tokyo, Japan) having nominally a 20 nm tip radius and 0.05 N/m cantilever spring constants were used in as-received condition for experiments. Friction data as a function of applied load was obtained by scanning in contact mode while simultaneously ramping the normal force

setpoint from positive (compressive) to negative (tensile) load until the tip separated from the surface. The adhesive force of the tip-sample junction was defined as the magnitude of the tensile force at pull-off while the lateral friction force was defined as the half-width of the friction force loop at each load. Normal and lateral forces were calibrated according to methods outlined in [68] and [69], respectively. The normal force calibration relies on the resonant frequency, quality factor, and geometry of the cantilever. The lateral force calibration uses a commercially available grating with planar facets simplifying the calibration. Cantilever-tilt compensation was employed to reduce coupling with sample topography[70]. One SAM coated and one TCP/SAM coated Si wafer were tested at multiple points per wafer. Using 20 nm as the tip radius, a Hertzian contact pressure of 2.0 GPa is calculated at the maximum load (~6 nN including adhesion).

Microscopic single-asperity interactions typically resulted in friction being a nonlinear function of load — and sphere-on-SAM interactions can be particularly complex[71,72,73], so it was not entirely appropriate to use the metric "coefficient of friction" in this context. Instead an *approximate* friction coefficient, defined as a linear fit to the data *in the positive loading regime only* was reported. This definition was justified on the bases that (1) nonlinear effects were more pronounced in the tensile regime, compromising the fitting process and (2) other sliding tests in this study were performed at positive load, so this usage best facilitated cross-technique comparison.

3.5 Vacuum System

The QCM data and the generation of TCP samples were performed in the vacuum chamber illustrated in Fig. 3.8. This chamber was modified from an existing chamber to fit the needs of the present studies. These modifications include a liquid nitrogen-cooled (LN_2) trap to condense any errant TCP vapor before contamination of the pump and its eventual release into the laboratory environment, the addition a leak valve to allow alcohol adsorption, and a transfer arm to manipulate samples inside the chamber. There are three stages of pumps on this system to achieve high vacuum (HV). The first is a roughing sorption pump which was used to go from atmospheric pressure (760 Torr) to a point where the turbomolecular pump (turbo) may be used (mTorr). The sorption pump is a LN_2-cooled chamber filled with a high surface area zeolite which acts as an adsorption site for gases to condense in the liquid phase. The turbo is a mechanical turbine which creates a pressure gradient and can operate in the mTorr range reaching a pressure of $\sim 10^{-6}$ Torr. Due to the small size of the vacuum chamber, the sorption pump was used to back the turbo without fear of saturation. At this point the valve to an operating ion pump was opened and the pressure was able to reach $\sim 10^{-8}$ Torr with a bake of the chamber to 150°C. The pumping speed of the ion pump and the high occluded areas of the vacuum chamber limit the base pressure of the vacuum system to $\sim 10^{-8}$ Torr.

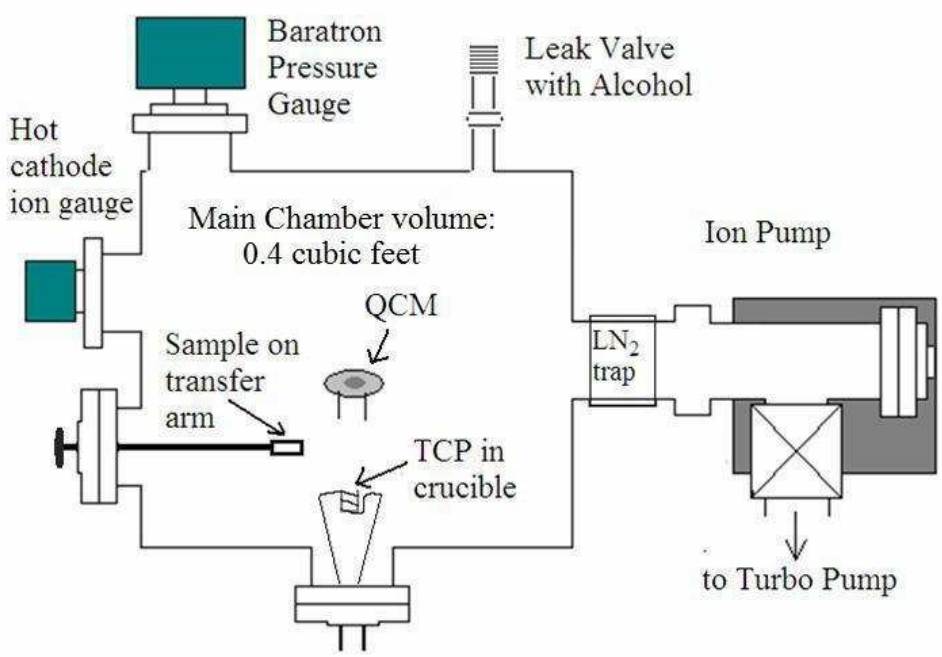

Fig. 3.8 shows a schematic of the custom modified vacuum system showing pressure gauge, various pumps, and sample manipulators (not to scale).

3.6 QCM electrode preparation

MEMS devices are currently fabricated from silicon and aluminum[74], so these surfaces (in addition to a SAM) were used as electrodes on a QCM. All of the silicon coated QCMs were obtained from Maxtek, Inc (now Inficon) and have a Cr/Au interlayer for adhesion. They possess a fundamental resonant frequency of around 5 MHz and oscillate in AT-cut transverse shear mode. Aluminum was also chosen for the electrode surface because in an ambient air environment it possesses a native surface oxide similar to that of silicon; this native oxide termination on the QCM was needed for the SAM to chemisorb to the crystal surface[75]. The aluminum and SAM coated QCMs were grown

ex situ in a vacuum chamber dedicated for metal deposition. They were fabricated by thermally evaporating titanium and aluminum layers *in vacuo* onto both sides of commercially available, blank 8MHz AT-cut quartz crystals, obtained from Colorado Crystal Corp. An additional QCM acting as a rate monitor was placed beside the blank crystals to infer the desired amount of evaporant achieved on the samples. The titanium layer was 20 nm thick and acted as an adhesion layer for the 50 nm thick aluminum coating.

3.7 SAM deposition onto QCMs and Si Wafers

The SAM, perfluorodecyl-trichlorosilane (PFTS) $CF_3(CF_2)_7(CH_2)_2SiCl_3$, was coated onto P-type, boron doped, silicon (111) (obtained from WaferWorld, West Palm Beach, FL) substrates using standard literature liquid deposition techniques[76] is illustrated in Fig. 3.9. All samples were cleaned by first rinsing in de-ionized water followed by a methanol rinse. To assure deposition uniformity, all the substrates were UV-ozone cleaned for 15 min and placed in subsequent baths of water, isopropanol (IPA), and trimethylpentane (TMP) for 5 min each. Following these surface preparation steps, the samples were immersed for two hours into a bath of PFTS/anhydrous TMP solution contained within a dry nitrogen environment; this procedure has been reported to provide a densely-packed monolayer of PFTS on silicon oxide[76]. Next, following the referenced procedure, the samples were placed into subsequent baths of TMP, IPA, and water for 5

min each to remove any unbonded silane chains. The same procedure was used to coat the aluminum and silicon crystals used in QCM measurements.

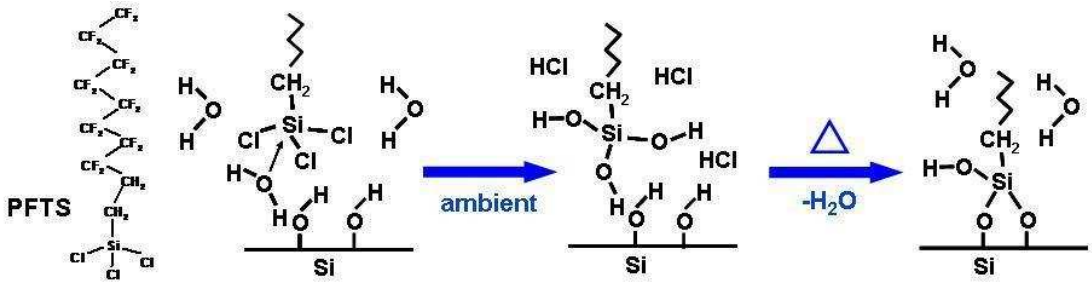

Fig. 3.9 shows an illustration of PFTS and the schematic for its chemisorption to a silicon oxide surface.

One way to determine the wettability of a liquid droplet on a surface is to measure the angle of the edge of the droplet to the center of the droplet. If the contact angle is low, then the liquid is said to wet the surface. If the contact angle is high, then the liquid is said to not wet the surface. This contact angle is shown in Fig. 3.10 of water on SiO_2 (very low ~5°) and on PFTS (very high ~100°). SiO_2 is known to be hydrophilic, and PFTS is known to be hydrophobic. The contact angle is a good measure of whether or not a liquid will form capillary forces. If the contact angle is higher than 90°, then capillaries are forbidden to form.

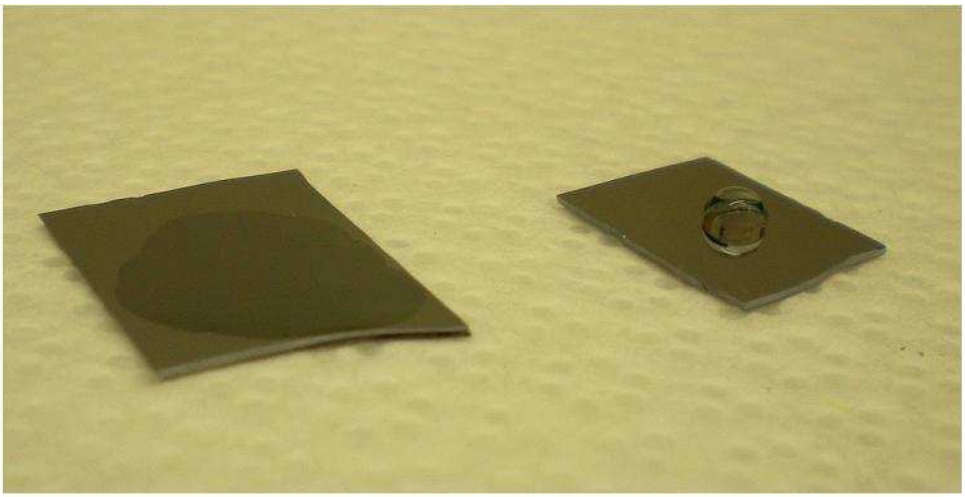

Fig. 3.10 shows the approximate contact angle and wettability of water on a hydrophilic SiO_2 surface (left) and a hydrophobic PFTS surface (right).

3.8 Tricresyl phosphate adsorption onto QCMs and Si Wafers

TCP, obtained from the Naval Research Laboratory, was deposited on the designated PFTS-coated wafers and bare Si wafers using a simple vacuum evaporation technique. Samples (either QCM or Si wafer) were placed in the center of the vacuum chamber directly above a tungsten wire crucible containing TCP shown in fig. 3.7. The vacuum chamber reached a base pressure without a bake (since that would release the TCP into vapor form) of 10^{-7} Torr with an ion pump without vaporization of the TCP. Deposition of TCP was performed by heating the crucible to over 100° C with a current of 3 Amps through the wire basket; heating the crucible was necessary to release TCP into the vapor phase, since TCP has a low vapor pressure at room temperature. During this process, the vacuum pressure was maintained at 10^{-6} Torr with the turbo pump and a

LN_2 trap. A LabView program was used to measure the frequency and amplitude shifts of the QCM during deposition. Prior to QCM friction measurements a high-purity N_2 calibration was performed for quality factor conversions. The QCM was used to standardize the amount of TCP uptake for all wafer depositions.

3.9 Characterization of PFTS and TCP adsorption

To verify the deposition of the PFTS monolayer and the TCP lubricant layer, Fourier transform infrared (FTIR) and X-ray photoelectron (XPS) spectra were obtained from coated Si wafer surfaces. FTIR analyses were performed using a Thermo-Nicolet Magna 760 IR spectrometer with a mercury-cadmium-telluride detector (MCT-B); each spectrum was the sum of 128 scans taken with the resolution setting at 8 (3.857 cm^{-1} data spacing), using a single bounce, germanium crystal, attenuated total reflection (ATR) accessory to probe the surface of the sample. XPS measurements (Thermo VG Scientific Escalab 220i-XL) were performed using a monochromatic Al Kα-source. Survey spectra (1.8 eV analyzer resolution, 1 eV point spacing) as well as high resolution scans (0.3 eV analyzer resolution, 0.1 eV point spacing) were taken at the primary energy regions for carbon (C 1s), silicon (Si 2p), oxygen (O 1s), fluorine (F 1s), and phosphorus (P 2p). Elemental spectrum fitting was completed using a commercially available software package[77] that fits the individual peaks with a convolution of Gaussian and Lorentzian

line shapes after modeling the inelastic electron background with a linear combination of Shirley and polynomial functions.

Both XPS and FTIR confirmed that the deposition procedures produced surfaces containing the bound PFTS and mobile TCP layers, respectively. The XPS survey spectrum shown in Fig. 3.11 of the PFTS coating on silicon and the TCP/PFTS layers on silicon confirmed the presence all the expected surface species (silicon, carbon, oxygen, and fluorine) except for phosphorus from TCP. Although peaks were evident in the P 2p region between 124-144 eV, these could not conclusively be identified as phosphorus since single crystal silicon substrates produce plasmon resonances that directly overlap at the same binding energy. High resolution scans of the C 1s region determined the presence of four peaks in both the PFTS coating and the combination PFTS/TCP layer on silicon. Two of these peaks are characteristic of surface carbon contaminants and the other two are shifted to higher binding energies, typical of two unequivalent carbon-fluorine bonds, $-CF_2$ and $-CF_3$. These latter peaks confirmed the presence of PFTS on the PFTS-coated silicon and the combination PFTS/TCP-layered silicon samples. No chlorine was observed in any of the XPS spectra, assuring that all of the unreacted PFTS had been washed away.

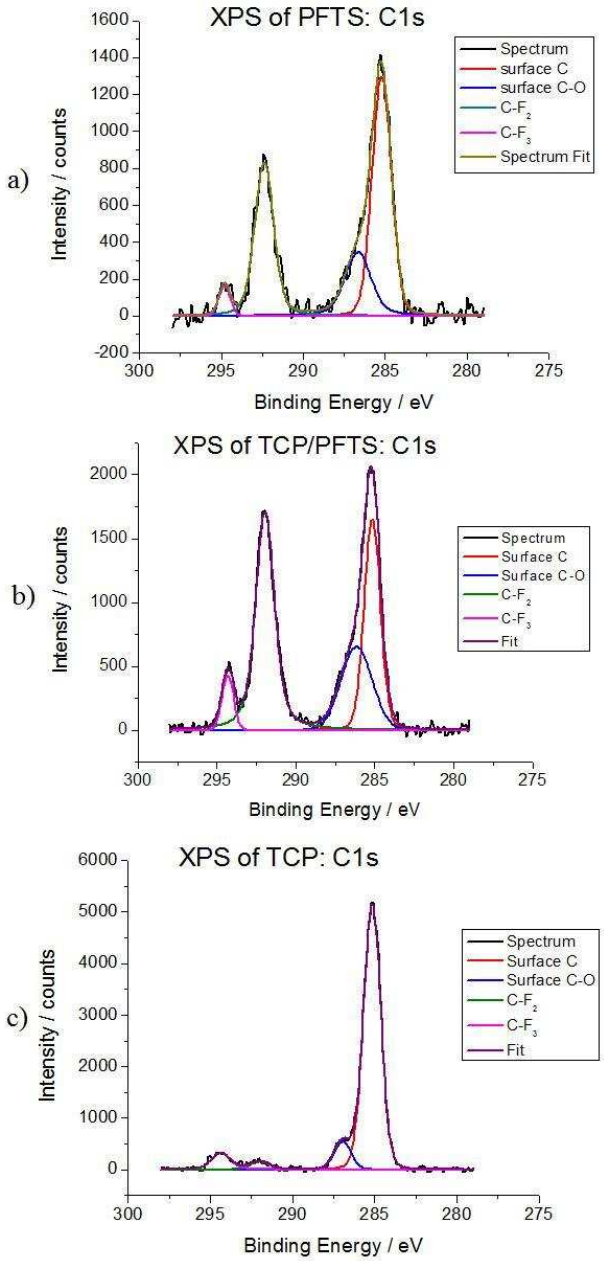

Fig. 3.11 High-resolution XPS spectra of the C-1s region taken of a) the bound PFTS layer on silicon and b) the combined bound PFTS and mobile TCP coating confirmed the presence of the carbon-fluorine bonding, indicative of the $C-F_2$ and $C-F_3$ bonds present in PFTS. An XPS spectrum of the same region of c) the mobile TCP layer deposited on silicon showed minimal C-F bonding.

FTIR spectroscopy of the bound-only PFTS coating shown in Fig. 3.12 on silicon with an uncoated silicon wafer as a reference revealed only the phonon absorption bands typical of uncoated silicon. Since the penetration depth of the evanescent wave in a single bounce Ge ATR accessory is approximately 300 nm, the signal from the lattice vibrations of the silicon substrate with its own native oxide greatly exceeded the signal from the single monolayer PFTS coating (~3 nm thick) that possessed Si-O and C-F bonding species [Ross Boyle, "FT-IR Measurement of Interstitial Oxygen and Substitional Carbon in Silicon Wafers", Application Note #50640, Thermo Fisher Scientific, Madison, WI].

Thus, the signal of the PFTS monolayer did not contain a species that possessed a distinct, strong infrared absorption profile to distinguish it from the absorption of the silicon substrate. Absorption peaks from the underlying silicon substrate were also evident in the combined PFTS/TCP coating on silicon. However, the combination bound PFTS/mobile TCP layer on silicon had numerous absorption bands from 1700 cm^{-1} – 500 cm^{-1}. These peaks correspond directly to the expected absorption bands of liquid TCP[78]. Thus, FTIR spectroscopy verified TCP was in fact deposited during the evaporation procedure.

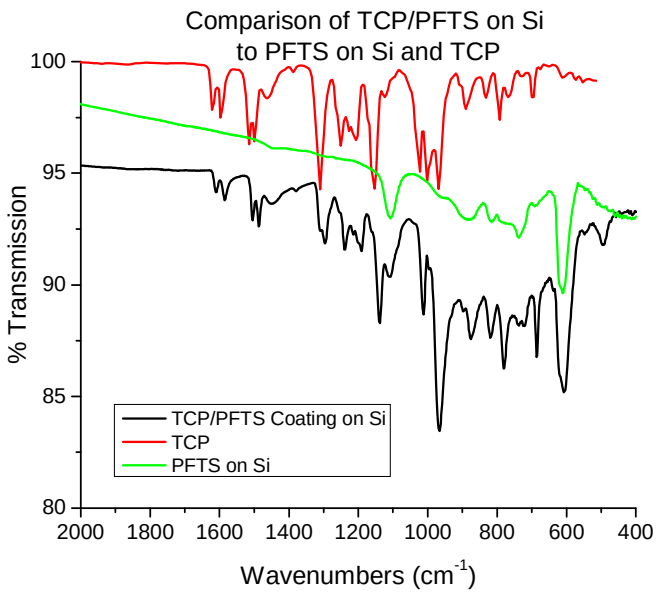

Fig. 3.12 Using an ATR accessory, FTIR spectra were taken of the combined bound PFTS/mobile TCP coating on silicon (black) and PFTS on silicon (blue). The PFTS on silicon showed on absorption phonons from the underlying silicon substrate. Comparing these spectra to reference FTIR spectra of liquid TCP (red), confirmed that the spectrum of the bound PFTS/mobile TCP coating possessed absorption bands consistent with both TCP and silicon.

3.10 Alcohol Adsorption onto QCMs

The QCM samples, with silicon, aluminum or PFTS/aluminum electrodes, were placed into said vacuum chamber in fig. 3.7. Adsorbate gases were then slowly leaked into the chamber while amplitude and frequency shifts of the QCM versus pressure were recorded. The saturated vapor pressures of ethanol, TFE, and pentanol are 45, 60, and 2 Torr respectively, so corrections to the amplitude and frequency for gas damping were

performed in advance of analyzing the data to obtain slip times. The pumpout of the vacuum chamber post alcohol adsorption was also performed while the LabView program was running. Calibration of the amplitude data was performed before each data run by leaking high purity N_2 into the chamber.

Ethanol and pentanol were obtained from Fisher Scientific, and trifluoroethanol (TFE) was obtained from Alfa Aesar. To purify the alcohols each of them was frozen with LN_2 in an enclosed vial connected to the vacuum chamber. After freezing they were opened to the chamber and pumped on with the turbo pump. The alcohols were warmed to room temperature after closing the valve to the chamber. This distillation process was repeated three times. Numerous data sets were collected for the various systems examined here. Representative data sets for each system are presented in the following results section.

3.11 Electronics

The QCM in vacuum is electrically connected via feedthrough to an oscillating circuit outside the vacuum, specifically a Pierce Oscillator circuit shown in Fig. 3.9 reproduced from [79]. The circuit drives the crystal at its fundamental resonant frequency by applying an alternating voltage to the electrodes of the QCM. There is a variable capacitor, resistor, and inductor to tune the circuit. The variable capacitor was tuned to maximize the output signal, the variable resistor controlled the power transferred to the

QCM, and the variable inductor was changed to match the output impedance of the circuit to a 50g load. The Pierce circuit is specifically designed to oscillate a QCM at its fundamental frequency only, i.e. no overtones.

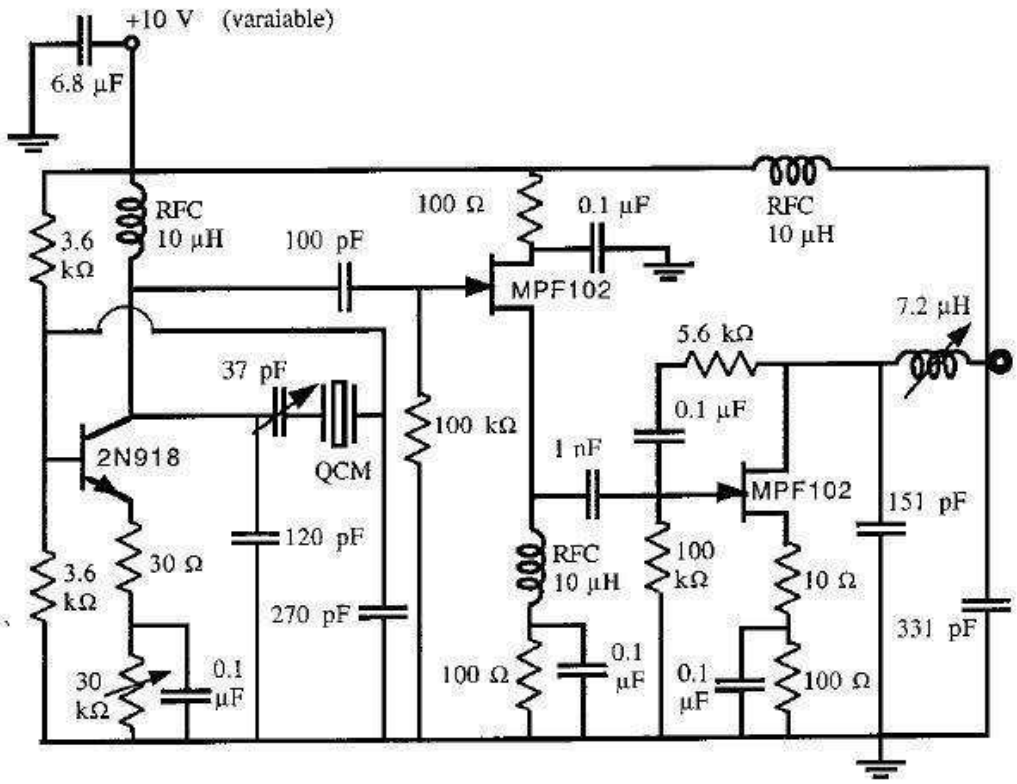

Fig. 3.13 shows the schematic of a Pierce Oscillator circuit.

The sinusoidal output signal of the Pierce circuit mimics the mechanical motion of the QCM and has been shown to be proportional to that motion[60]. Since the amplitude of a MHz signal is not easily measured with precision, a mixing circuit was employed to change the MHz signal to a KHz one. This mixing circuit, shown in Fig. 3.10 and reproduced from [79], was used with a stable reference QCM also driven by a Pierce circuit.

The mixing circuit multiplies the two signals and a sum and difference signal is created from the relation

$$\cos\omega_{\text{ref}}t\cos\omega_{\text{exp}}t=\frac{1}{2}\cos\left(\omega_{\text{ref}}+\omega_{\text{exp}}\right)t+\frac{1}{2}\cos\left(\omega_{\text{ref}}-\omega_{\text{exp}}\right)t \qquad (3.33)$$

A Low-pass filter was set in place to attenuate the sum signal and pass the difference signal.

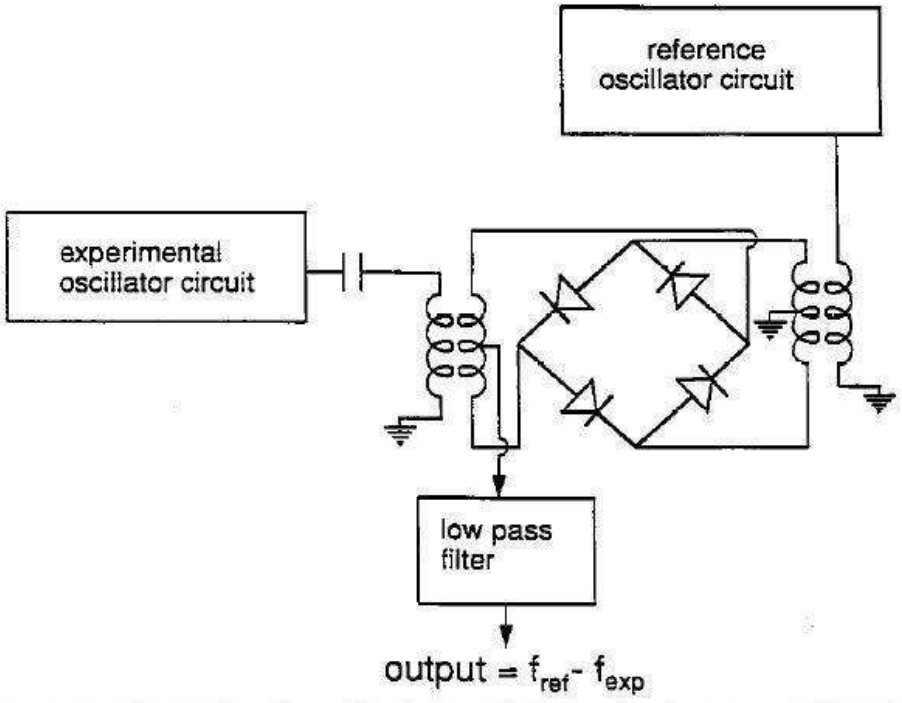

Fig. 3.14 shows the mixer circuit from the two signals generated by Pierce circuits. The low pass filter attenuates the sum of the two signals and passes the difference.

The mixed signal was sent to a frequency counter and a Keithley digital multi-meter, both of which are connected to a laboratory computer through a GPIB card. The capacitance manometer pressure heads were also connected via GPIB. A LabView

program was designed to take these inputs every six seconds and output a six column text array. An Origin program used this array to calculate the slip time as a function of coverage. The program accounted for all of the hurdles previously described in the QCM derivation to accurately determine the slip time.

---

[55] B.P. Miller and J. Krim, "Quartz Crystal Microbalanc (QCM) Applications to Tribology" Enc. Trib. Submitted.

[56] G. Z. Sauerbrey, Z. Phys. 155 (1959) 206.

[57] J. Krim and A. Widom, "Damping of a crystal oscillator by and adsorbed monolayer and its relation to interfacial viscosity" Phys. Rev. B 38 (1988) 12184.

[58] C. D. Stockbridge, Vacuum Microbalance Tachniques (Plenum, New York, 1966), Vol. 5.

[59] L. Bruschi and G. Mistura, "Measurement of the friction of thin films by means of a quartz microbalance in the presence of a finite vapor pressure" Phys. Rev. B 63 (2001) 235411.

[60] B. Borovsky, B. L. Mason, J. Krim, "Scanning tunneling microscope measurements of the amplitude of vibration of a quartz crystal oscillator", J. App. Phys. 88 (2000) 4017.

[61] E. Watts, J. Krim, A. Widom, "Experimental observation of interfacial slippage at the boundary of molecularly thin films with gold substrates" Phys. Rev. B 41 (1990) 3466.

[62] M. Rodahl, B. Kasemo, "A simple setup to simultaneously measure the resonant frequency and the absolute dissipation factor of a quartz crystal microbalance" Rev. Sci. Instrum. 67 (1996) 3238.

[63] J. Krim, D.H. Solina, R. Chiarello, "Nanotribology of a Kr monolayer: A quartz-crystal microbalance study of atomic-scale friction", PRL 66, 181 (1991).

[64] L. Bruschi, A. Carlin, G. Mistura, "Depinning of Atomically Thin Kr Films on Gold" PRL 88, 046105 (2002).

[65] A. Dayo, W. Alnasrallah, J. Krim, "Superconductivity-Dependent Sliding Friction" PRL 80, 1690 (1998)

[66] M. Highland, J. Krim, "Superconductivity Dependent Friction of Water, Nitrogen, and Superheated He Films Adsorbed on Pb (111)" PRL 96, 226107 (2008).

[67] Q. Ding, C. Li, L. Dong, M.Wang, Y. Peng, X. Yan, "Preparation and properties of $YBa_2Cu_3O_{7-\delta}$/Ag self-lubricating composites" Wear 265, 1136 (2008).

[68] Sader, J. E., Chon, J. W. M., and Mulvaney, P.: Calibration of rectangular atomic force microscope cantilevers. Rev Sci Instrum 70, 3967-3969 (1999).

[69] Varenberg, M., Etsion, I., Halperin, G.: An improved wedge calibration method for lateral force in atomic force microscopy. Rev Sci Instrum 74, 3362-3367 (2003).

[70] Cannara, R. J., Brukman, M. J., Carpick, R. W.: Cantilever tilt compensation for variable-load atomic force microscopy. Rev Sci Instrum 76, 053706 (2005).

[71] Brukman, M. J., Marco, G. O., Dunbar T. D., Boardman, L. D., Carpick, R. W.: Nanotribological Properties of Alkanephosphonic Acid Self-Assembled Monolayers on Aluminum Oxide: Effects of Fluorination and Substrate Crystallinity. Langmuir 22, 3988-3998 (2006).

[72] Chandross, M., Lorenz, C. D., Stevens, M. J., Grest, G. S.: Simulations of Nanotribology with Realistic Probe Tip Models. Langmuir 24, 1240-1246 (2008).

[73] Flater, E. E., Ashurst, W. R., Carpick, R. W.: Nanotribology of Octadecyltrichlorosilane Monolayers and Silicon: Self-Mated versus Unmated Interfaces and Local Packing Density Effects. Langmuir 23, 9242-9252 (2007).

[74] Hornbeck, L. J.: The DMD (TM) projection display chip: A MEMS-based technology Source. MRS bulletin 26, 325-327 (2001).

[75] Devaprakasam, D., Sampath, S., Biswas, S. K.: Thermal Stability of Perfluoroalkyl Silane Self-Assembled on a Polycrystalline Aluminum Surface. Langmuir 20, 1329-1334 (2004).

[76] Srinivasan, U., Houston, M. R., Howe, R. T., Maboudian, R.: Alkyltrichlorsilane-Based Self-Assembled Monolayer Films for Stiction Reduction in Silicon Micromachines. J MEMS 7, 252-260 (1998).

[77] Hesse, R., Chassé, T., Szargan, R.: Peak shape analysis of core level photoelectron spectra using UNIFIT for WINDOWS. Fresenius' J Anal Chem 365, 48-54 (1999).

[78] Bertrand, P.A.: Reactions of tricresyl phosphate with bearing materials. Trib Lett 3, 367-377 (1997).

[79] Chris Daly. Ph.D. Dissertation, Northeastern University, 1996.

Chapter 4: Alcohol Raw data

4.1 Alcohol Raw Data[80]

Fig. 4.1-4.9 presents raw data for the three alcohols on PFTS, Si, and Al along with their respective N_2 calibrations. The calibrations shown as *R* vs. inverse amplitude (1/A) are the upper plots, 1/A vs. the pressure are the middle plots, and the negative change in frequency ($-\Delta f$) are the lower plots.

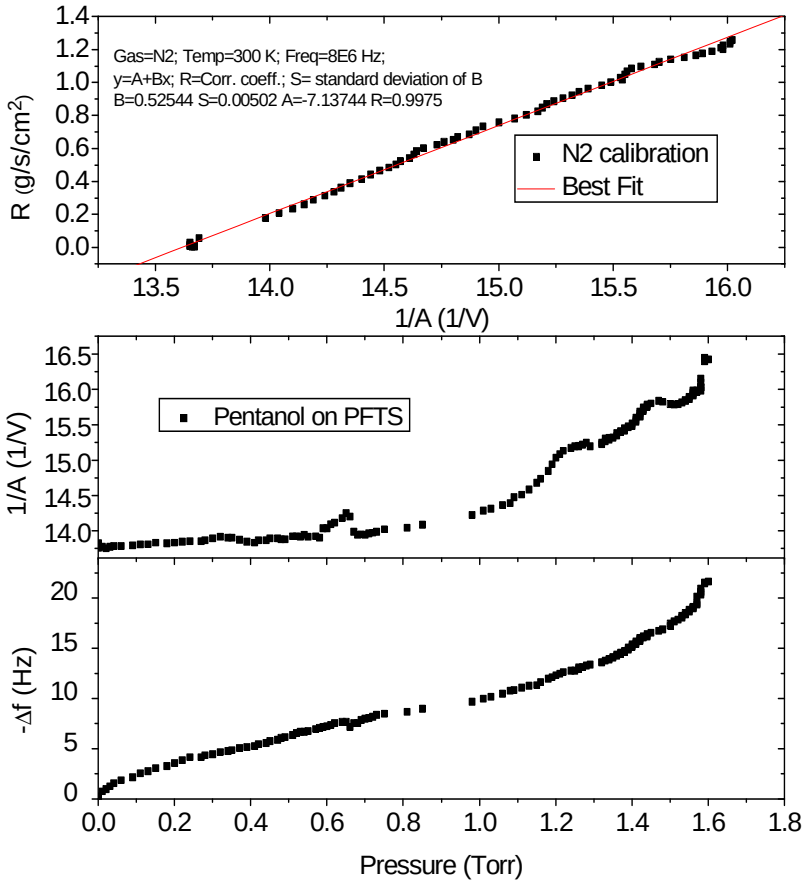

Fig. 4.1 shows the raw data for pentanol adsorbed onto PFTS. The calibration is from file: 6-20-07n2.txt and the pentanol uptake is from file: 6-20-07 pent_PFTS.txt

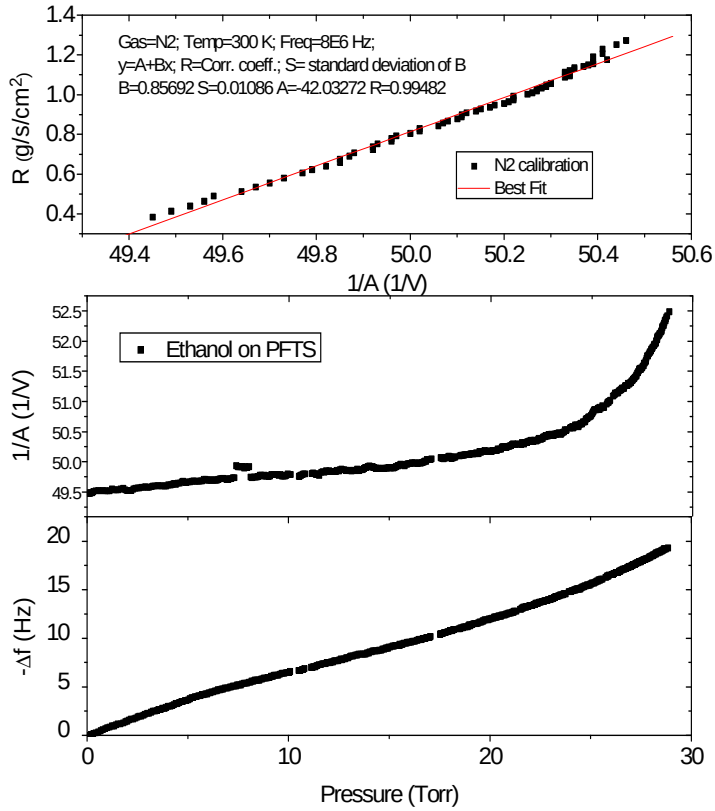

Fig. 4.2 shows the raw data for ethanol adsorbed onto PFTS. The calibration is from file: 8-3-07n2.txt and the ethanol uptake is from file: 8-3-07 EOH_PFTS.txt

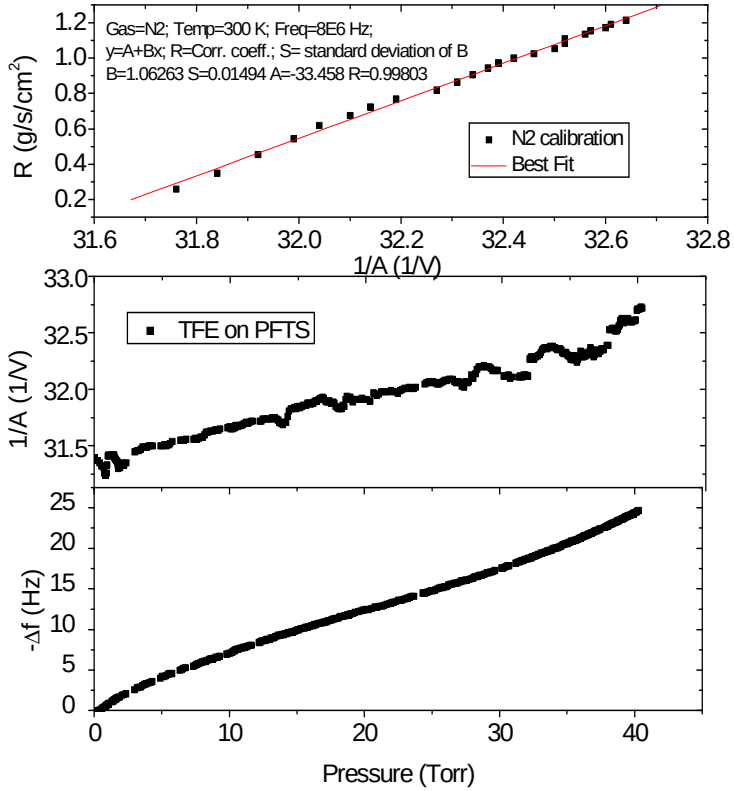

Fig. 4.3 shows the raw data for TFE adsorbed onto PFTS. The calibration is from file: 7-20-07n2.txt and the TFE uptake is from file: 7-20-07 TFE_PFTS.txt

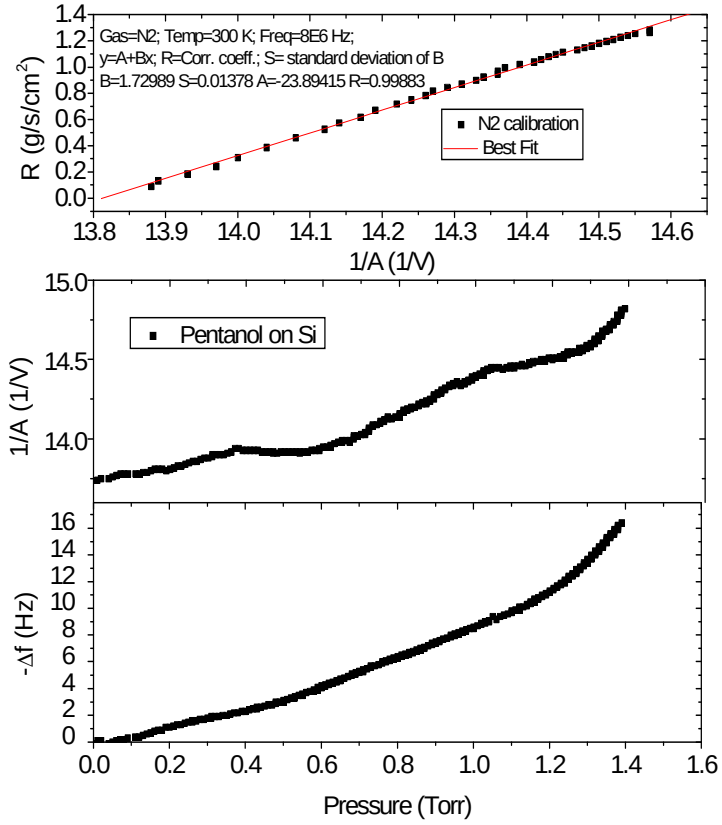

Fig. 4.4 shows the raw data for pentanol adsorbed onto Si. The calibration is from file: 1-7-08n2.txt and the pentanol uptake is from file: 1-7-08 pent_Si.txt

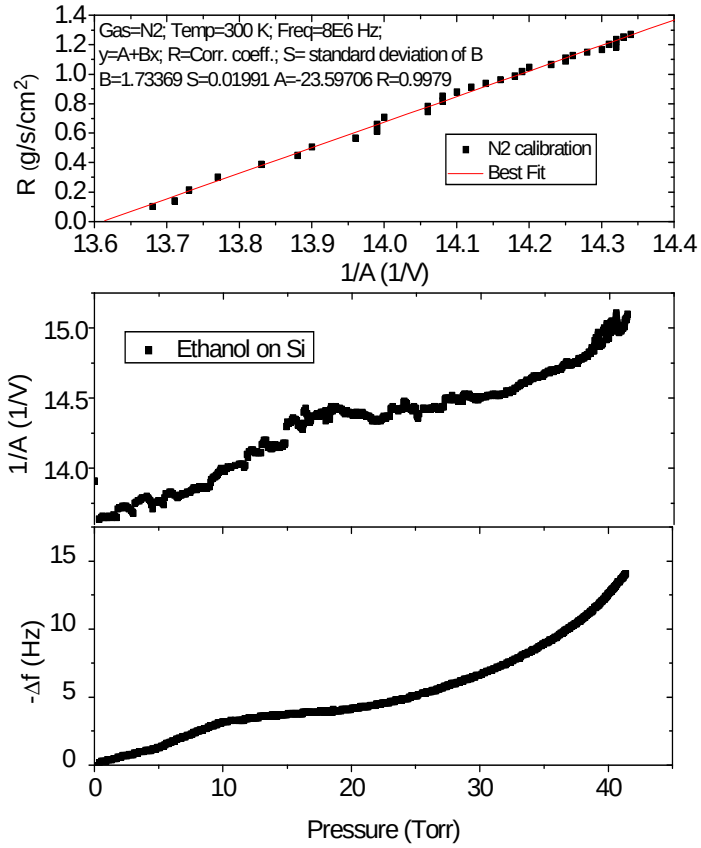

Fig. 4.5 shows the raw data for ethanol adsorbed onto Si. The calibration is from file: 1-2-08n2.txt and the ethanol uptake is from file: 1-2-08 EOH_Si.txt

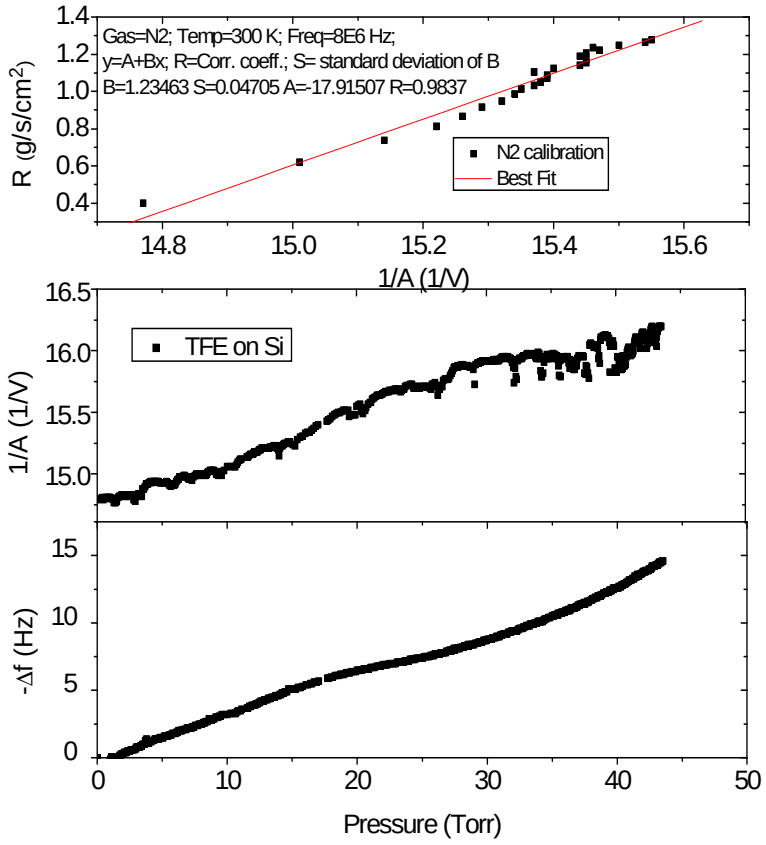

Fig. 4.6 shows the raw data for TFE adsorbed onto Si. The calibration is from file: 12-21-07n2.txt and the TFE uptake is from file: 12-21-07 TFE_Si.txt

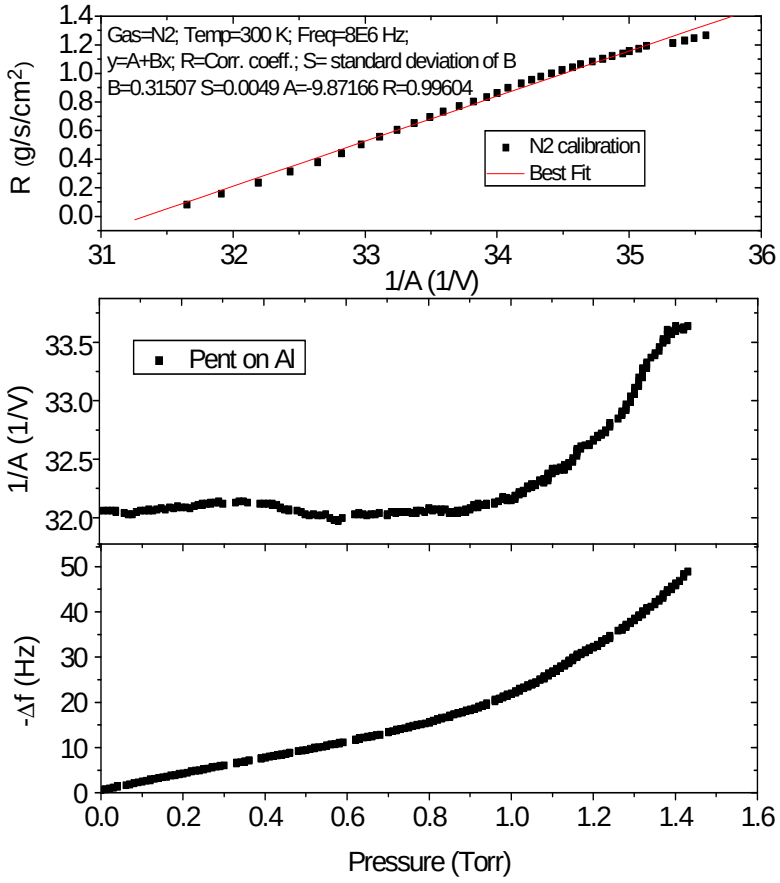

Fig. 4.7 shows the raw data for pentanol adsorbed onto Al. The calibration is from file: 12-6-07n2.txt and the pentanol uptake is from file: 12-6-07 pent_Al.txt

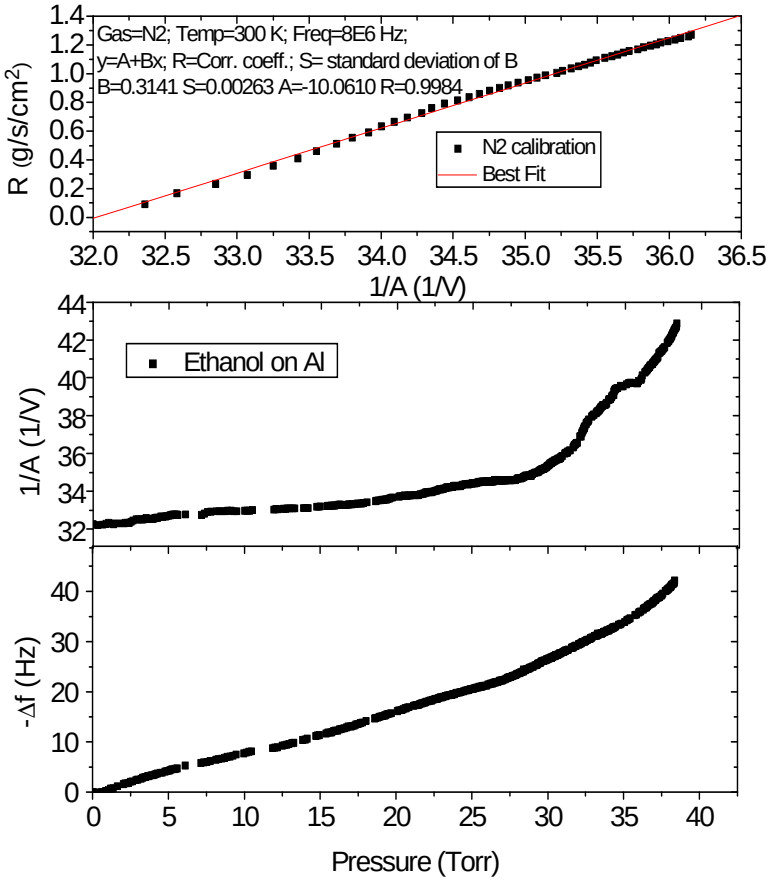

Fig. 4.8 shows the raw data for ethanol adsorbed onto Al. The calibration is from file: 12-11-07n2.txt and the ethanol uptake is from file: 12-11-07 EOH_Al.txt

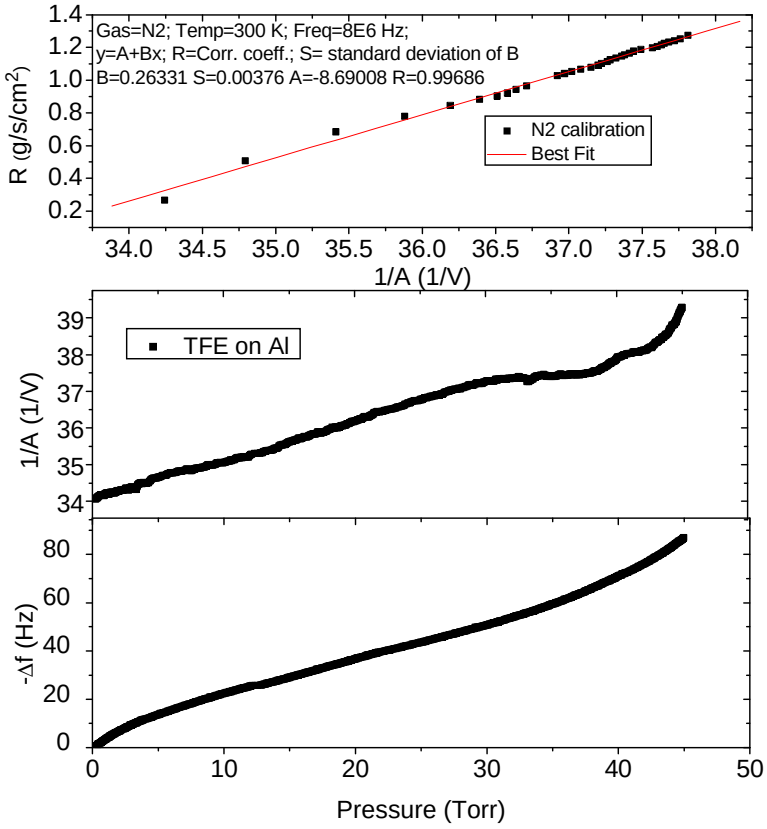

Fig. 4.9 shows the raw data for TFE adsorbed onto Al. The calibration is from file: 12-14-07n2.txt and the TFE uptake is from file: 12-14-07 TFE_Al.txt

4.2 Results of alcohol adsorption after pumpout

The results from [80] were taken from the leak in of various alcohols from high vacuum to their vapor pressures. Like many scientific discoveries an interesting result was seen by chance. Hysteretic behavior for the uptake of pentanol on PFTS and non-hysteretic behavior with alcohol uptake on Si was noted, as illustrated in Fig. 4.10 in

which coverage vs. partial pressure was plotted. It is readily seen that the coverage follows the same path on Si regardless of adsorption or desorption.

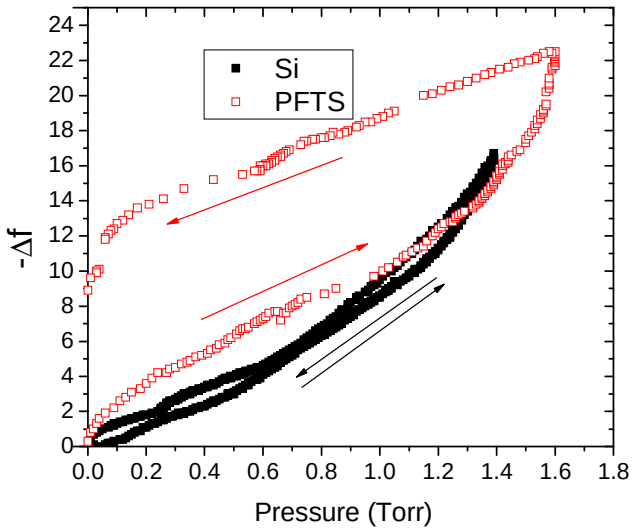

Fig. 4.10 shows the coverage vs. the pressure for pentanol on an 8MHz PFTS QCM and on a 5MHz Si QCM. Arrows indicate increase or decrease of pressure. The results were taken from the same runs as fig. 4.1 and 4.4.

Hysteretic behavior was also seen with the dissipation of pentanol on PFTS and not on Si. This is plotted in Fig. 4.11 as the inverse amplitude (1/A) vs. the pressure in Torr. All three alcohols on Si showed the same non-hysteretic behavior, but a dissimilar result between the alcohols occurred on PFTS.

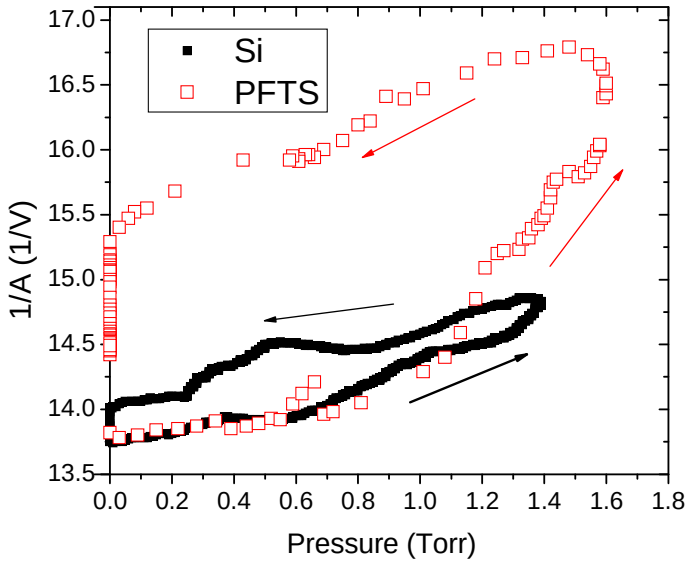

Fig. 4.11 shows the non-zero endpoint for the change in inverse amplitude for pentanol on PFTS compared to the zero endpoint for pentanol on Si after the same amount of pumpout time of 20 minutes.

Looking at TFE on PFTS has provided some insight into why this hysteresis occurs. The PFTS did in fact cause hysteresis with the uptake, but the inverse amplitude returned to its original starting point after pumpout. The raw data for this interesting result is apparent in Fig. 4.12 as time goes to 80 min.

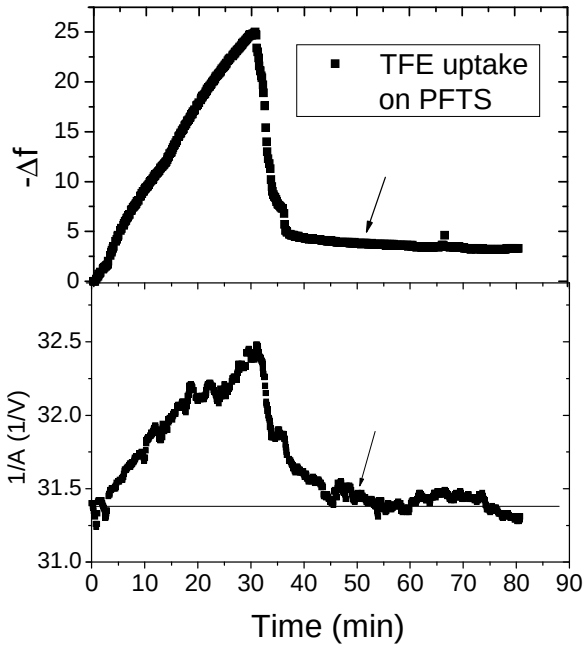

Fig. 4.12 shows the raw data for TFE on PFTS as a function of time. Hysteretic behavior is seen with the frequency but not with the amplitude after the vapor is removed as indicated by the arrows. This data is the same as fig. 4.3.

Results for ethanol and pentanol were repeated on Si with a methanol rinse and UV ozone treatment. The QCM was immediately placed into the vacuum chamber to minimize contamination. Similar results to TFE on PFTS were witnessed. Hysteresis with the frequency of roughly a ½ monolayer on the surface after pumpout without any net change in amplitude is apparent in Fig. 4.13.

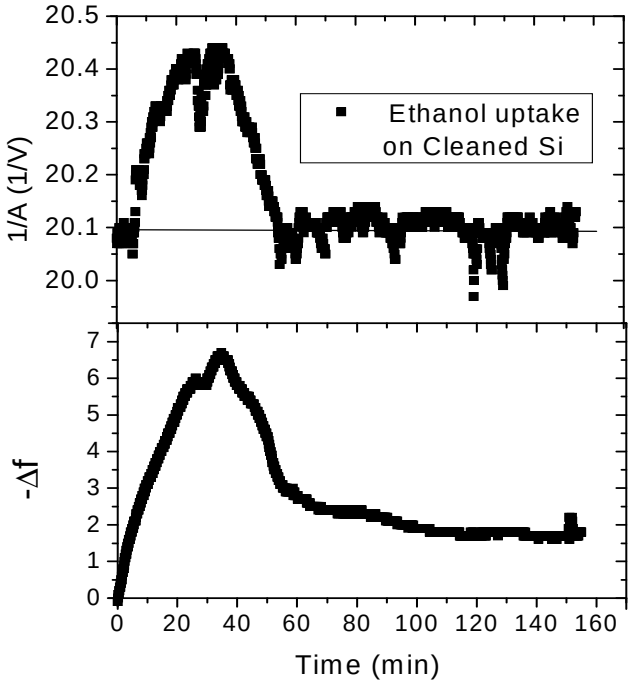

Fig.4.13 shows the raw data vs. time for ethanol on UV Ozone cleaned Si. It is clearly seen that the frequency does not return to zero, but the dissipation does. This data is from file: 9-30-08 EOH_Si.txt

To analyze this data one must account for gas damping effects of the alcohol environment to the amplitude and frequency of the QCM before any surface effects can be determined. Knowledge of the critical viscosity η_c (viscosity when the gas and liquid coexist at the critical temperature T_c) and molecular weight M is needed to calculate the dissipation that occurs strictly from the presence of a 3-dimensional gas to a QCM as discussed in Chapter 3. In addition, the 3-dimensional liquid density ρ_{3liq} is needed to calculate the thickness of an adsorbed monolayer and corresponding frequency shift of that layer. Table 4.1 lists these constants for the three alcohols studied.

Table 4.1 List of constants needed for analysis of QCM adsorption.

	η_c (Poise)	T_c (K)	M (g/mol)	ρ_{3liq} (g/cm^3)
Pentanol	1.853×10^{-5}	586	88.150	0.8144
Ethanol	1.49×10^{-4}	516	46.0684	0.789
TFE	2.7×10^{-4}	499	100.04	1.393

[80] B.P. Miller, J. Krim, J. Low Temp. Phys. 157, 252 (2009).

Chapter 5: Discussion of Alcohol Data

5.1 Analyzed Alcohol Data[81]

The estimated monolayer mass per unit area for pentanol, ethanol and TFE is 45.9, 36.2 and 68.6 ng/cm^2, respectively. This corresponds to a monolayer frequency shift of 13.3 (5.2), 10.5(4.1), and 19.9(7.7) Hz, respectively, for an 8 (5) MHz crystal. These estimates of the monolayer shift treat the molecules as cubes using their molecular weight and liquid density. In particular, pentanol has a molecular weight of 88.150 g/mol and a liquid density of 0.8144 g/cm^3. One can obtain the volume per molecule of pentanol by

$$\frac{88.150g}{\text{mol}}\times\frac{1\text{cm}^3}{0.8144g}\times\frac{1\text{mol}}{6.022\times10^{23}\text{molecules}}\times\frac{\left(1\times10^8\text{Å}\right)^3}{1\text{cm}^3}=\frac{180.\text{Å}^3}{\text{molecule}}$$

Therefore, the thickness of a monolayer was determined to be $\sqrt[3]{180\text{Å}^3}=5.64\text{Å}$. The thickness was used to calculate the mass per unit area of a monolayer $\rho_2=5.64\text{Å}\cdot0.8144\text{ g/cm}^3=45.9\text{ ng/cm}^2$. Using the Sauerbrey equation from (3.2) and multiplying by 2 to calculate the frequency shift of one monolayer of pentanol on *both* sides of a QCM. That calculation is shown for an 8MHz (5MHz) crystal as

$$\Delta f=2\cdot\frac{2\cdot8\text{MHz}^2\left(5\text{MHz}^2\right)\cdot45.9\text{ ng/cm}^2}{2.648g/\text{cm}^3\cdot3.34\times10^5\text{cm}/s}=13.3\text{Hz}\left(5.2\text{Hz}\right)$$

The same calculations were performed for ethanol having a 46.0684 g/mol molecular weight and a 0.789 g/cm^3 liquid density to obtain a volume per molecule of

97.0 $Å^3$/molecule and a thickness of 4.59 Å. The correlated mass per unit area and frequency shift of a monolayer of ethanol is 36.2 ng/cm2 and 10.5(4.1)Hz, respectively. The values used for the molecular weight and liquid density of TFE were 100.04 g/mol and 1.393 g/cm3, respectively. The resulting thickness, mass per unit area, and frequency shift for a monolayer of TFE was calculated to be 4.92 Å, 68.6 ng/cm2, and 19.8(7.7)Hz, respectively.

The presence of a 3D gas has an effect on the frequency and amplitude of the QCM as shown in Chapter 3, specifically equation (3.8) and (3.12). To determine the effects of the adsorbed layer the gas damping effects must be subtracted out. A sample calculation for this subtraction was performed using the ethanol at 10 Torr. The viscosity η is a function of temperature, so at room temperature η is a constant. Using the critical viscosity for ethanol of $\eta_c = 1.49\times10^{-4}$ Poise at the critical temperature $T_c = 516$K, one can extrapolate the viscosity at any given temperature using

$$\eta(T < T_c) = \eta_c \left(\frac{T}{T_c} \right)^{0.71+0.29\left(T_c/T\right)} \qquad (5.1)$$

For T=300K $\eta = 7.7\times10^{-5}$ Poise. Using the ideal gas law and the conversion between Torr and dyne/cm^2 (cgs units) the mass density is calculated at 10 Torr of ethanol to be

$$\frac{1333 \cdot P(\text{Torr}) \cdot M\,(\text{g/mol})}{R_{gas} \cdot T(\text{K})} = \frac{1333 \cdot 10 \cdot 46.0684}{8.314\times10^7 \cdot 300} = 2.46\times10^5 \frac{\text{g}}{\text{cm}^3}$$

where M is the molecular weight. The value for the resistance *R* of a gas at high pressures on a QCM was shown in equation 3.10. However, the viscoelastic effects of a

gas at low pressures must be dealt with since the time for the excess particle momentum to relax is on the order of the oscillation period. This relaxation time is an important quantity obtained from the mean free path λ. Again, an example of ethanol at 10 Torr is used. This effect changes the value of *R* by

$$\sqrt{\frac{\omega\tau_r}{1+(\omega\tau_r)^2}\left(\sqrt{1+\frac{1}{(\omega\tau_r)^2}}+1\right)}\,. \tag{5.2}$$

The quantity τ_r is determined to be

$$\tau_r = 10\cdot\frac{\lambda}{v_{avg}} \qquad \lambda = \frac{1}{\sqrt{2}\pi}\frac{1}{d^2 n_v} \qquad v_{avg} = \sqrt{\frac{8R_{gas}T}{\pi M}} \tag{5.3}$$

where v_{avg} is the average velocity of a particle at a given temperature, *d* is the diameter of the molecule, n_v is the particle density and *M* is the molecular weight. The relaxation time comes to $\tau_r = 8.93\times10^{-8}$ s resulting in a resistance *R* = 0.14 g/cm^2/s. This gas damping was subtracted from the total dissipation obtained from the inverse amplitude resulting in damping from the adsorbed layer. Although the effect was small, gas damping was also performed for the correction to the frequency. Fig. 5.1 shows the correction to gas damping effects. The gas dissipation at 10 Torr was observed to be equivalent to the calculated *R* value of 0.14 g/ cm^2/s. Taking the value for *R* and multiplying by $\frac{4}{\omega\rho_q t_q}$ from eq. (3.8) will equal

$$\delta\left(\frac{1}{Q}\right) = \frac{4}{2\pi\cdot 5\text{MHz}\cdot 2.648\text{g/cm}^3\cdot 0.033\text{cm}}\cdot 0.14\ \text{g/cm}^2/\text{s} = 2.0\times10^{-7}$$

This value for the change in inverse quality factor is equivalent to the red gas damping line in fig. 5.3 at 0.22 P/P_o.

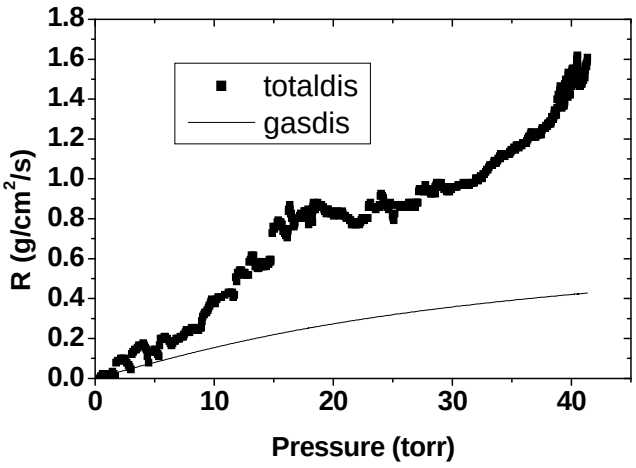

Fig. 5.1 shows the total dissipation of ethanol on Si along with the gas damping curve. The excess dissipation is attributed to slippage of the layer. This is taken from fig. 4.5.

Fig. 5.2 presents data for the three alcohols on PFTS (8MHz) including the adsorption isotherms as the negative change in the frequency versus the pressure normalized to its vapor pressure, P/P_0. The lower graph in fig. 5.2 shows the dissipation from the adsorbed film and the damping from the surrounding gas.

The lines show the contribution from gas damping, and the data points show the total dissipation. On PFTS it is apparent that the data points for TFE line up with the theoretical gas damping line, indicating no measurable interfacial slippage of the adsorbed layer and a zero slip time. Pentanol and ethanol both have excess dissipation from the adsorbed layer and thus a measurable slip time.

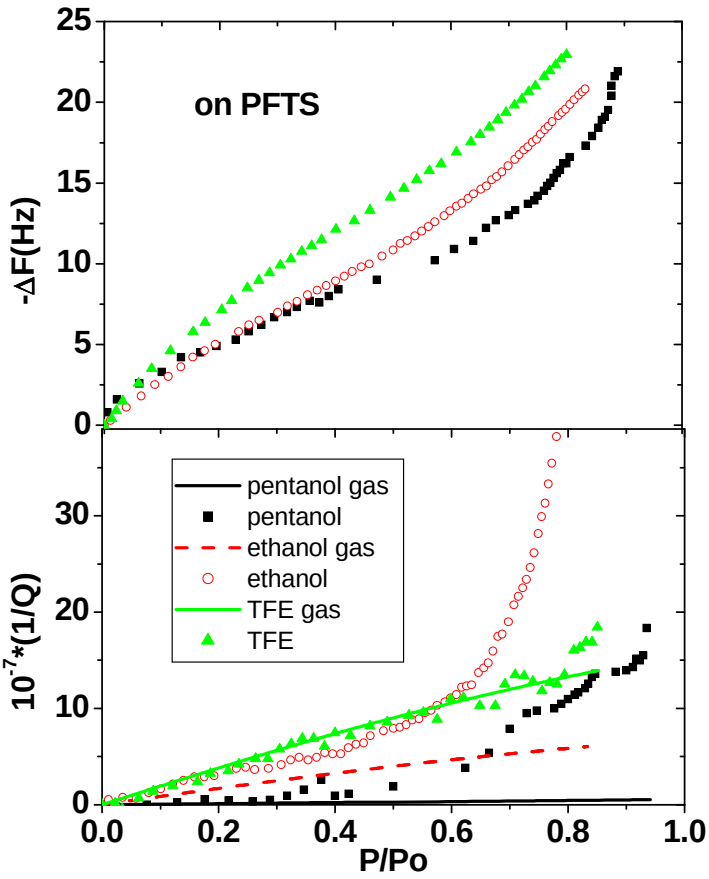

Fig. 5.2 Pentanol, ethanol, and TFE frequency and quality factor shift vs. partial pressure for uptake on PFTS. The lines show theoretical contributions to the gas damping from the vapor phase. Excess dissipation is attributed to interfacial friction from the adsorbed sliding layer. This is taken from fig. 4.1-4.3.

Fig. 5.3 depicts the raw data for the three alcohols on Si. The isotherms on the 5MHz crystal have characteristic knees indicating the formation of a monolayer. The knee at 4Hz for ethanol corresponds very well to the theoretical value, and the knee at 7Hz for TFE also corresponds well to the theoretical value. Since the pentanol molecule is long and straight, the theoretical estimate of a monolayer may be less precise. On the

lower graph there is an excess of dissipation for each of the alcohols corresponding to a measurable amount of slip time.

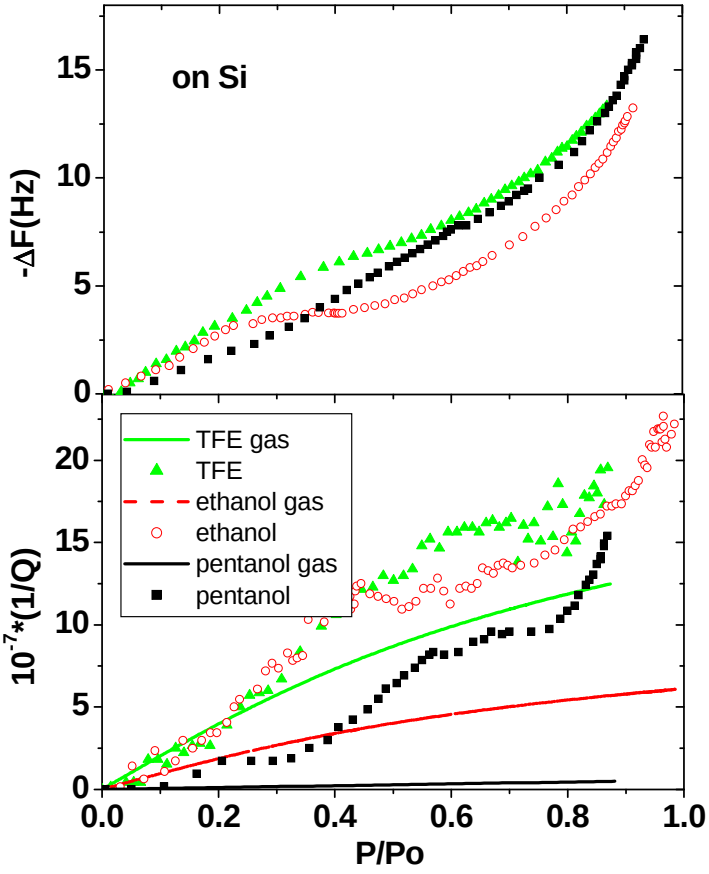

Fig. 5.3 Pentanol, ethanol and TFE frequency and quality factor shift versus partial pressure for uptake on Si. The lines show theoretical contributions to the gas damping from the vapor phase. This was taken from fig. 4.4-4.6.

Plotted in Fig. 5.4 is the raw data for the three alcohols on Al. The isotherms on the 8MHz crystal show considerably more uptake for TFE than pentanol and ethanol, and

there is significantly more uptake for each alcohol compared to the other substrates. On the lower graph neither pentanol nor TFE slips until close to their vapor pressure.

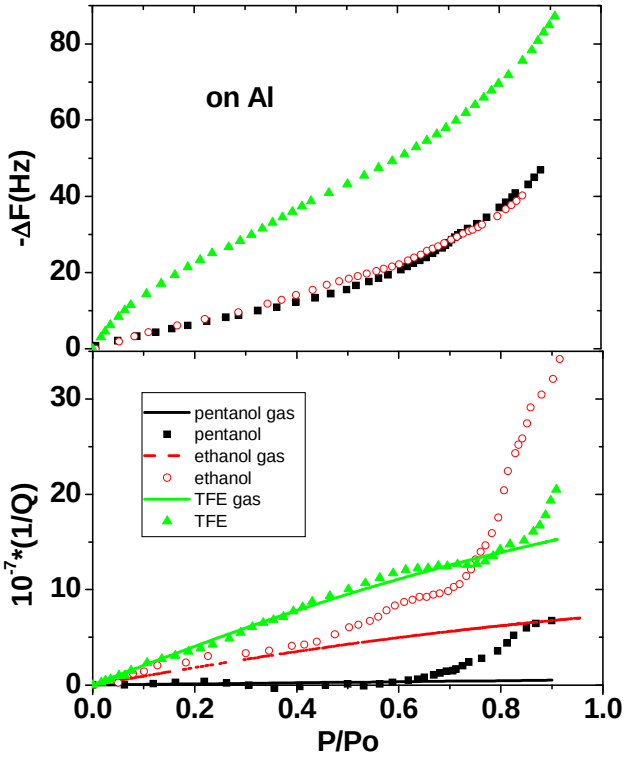

Fig. 5.4 Pentanol, ethanol and TFE frequency shift and quality factor shift versus partial pressure for uptake on Al. The dotted lines show theoretical contributions to the gas damping from the vapor phase. The theoretical frequency shift for a 8MHz QCM for these alcohols are 13.3, 10.5, and 19.9Hz, respectively. This was taken from fig. 4.7-4.9.

The slip time from eq. (3.22) is now measurable using the change in inverse quality factor and change in frequency from $\delta\left(Q^{-1}\right) = -4\pi\tau\delta f$. Fig. 5.5 presents slip time as a function of film coverage for the various systems studied from fig. 5.2-5.4, corrected for gas damping effects in advance of determining the slip time values. The measured

frequency shift Δf was corrected to the frequency shift of a rigidly attached layer Δf_{film} according to

$$\Delta f = \frac{\Delta f_{\text{film}}}{1+(\omega\tau)^2} \tag{5.4}$$

thus giving a more accurate calculation of film coverage normalized to the theoretical frequency shift of one monolayer. On PFTS, both pentanol and ethanol have significant non-zero slip times compared to TFE. This may be attributable to an incommensurate interface with pentanol and ethanol and a more commensurate interface with TFE making TFE less mobile than ethanol or pentanol. Internal shaking motion of the SAMs layer cannot be ruled out as a response to gas uptake rather than a pure slipping motion. The additional dissipation present, however, does indicate an additional degree of system mobility in either case upon condensation of the film.

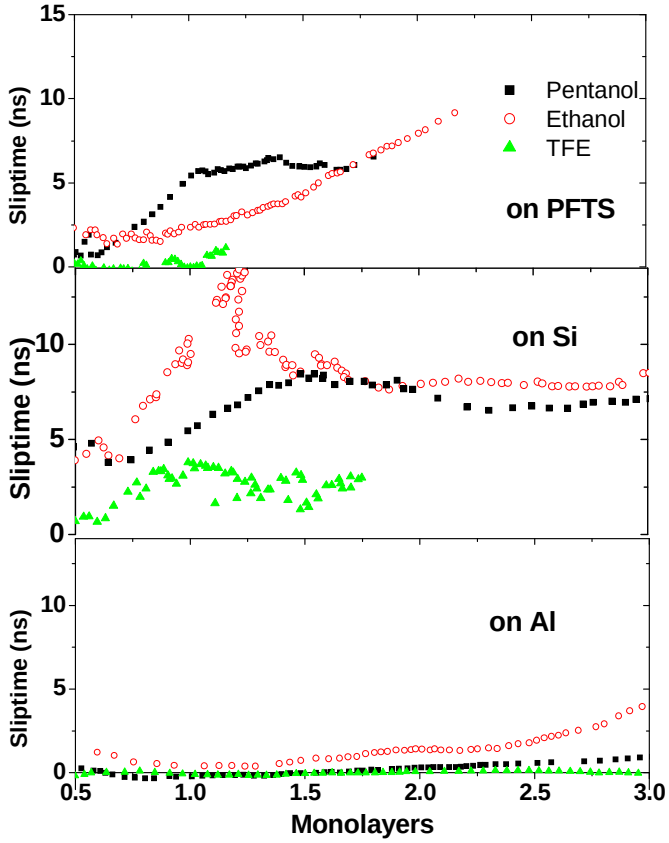

Fig. 5.5: Sliptime versus monolayer coverage corrected by (5.4) for the various systems studied.

A droplet of each of the alcohols were placed onto a PFTS coated Si wafer and a UV Ozone treated Si wafer to look at wetting qualitatively. Fig. 5.6 shows the pictures of these droplets. They each have a smaller contact angle on Si compared to PFTS. TFE had the smallest contact angle of the alcohols on PFTS, and pentanol had the largest contact angle on Si. The contact angles do not seem to have a direct effect on the slip time or diffusion coefficient, but each contact angle is less than 45° indicating wettability.

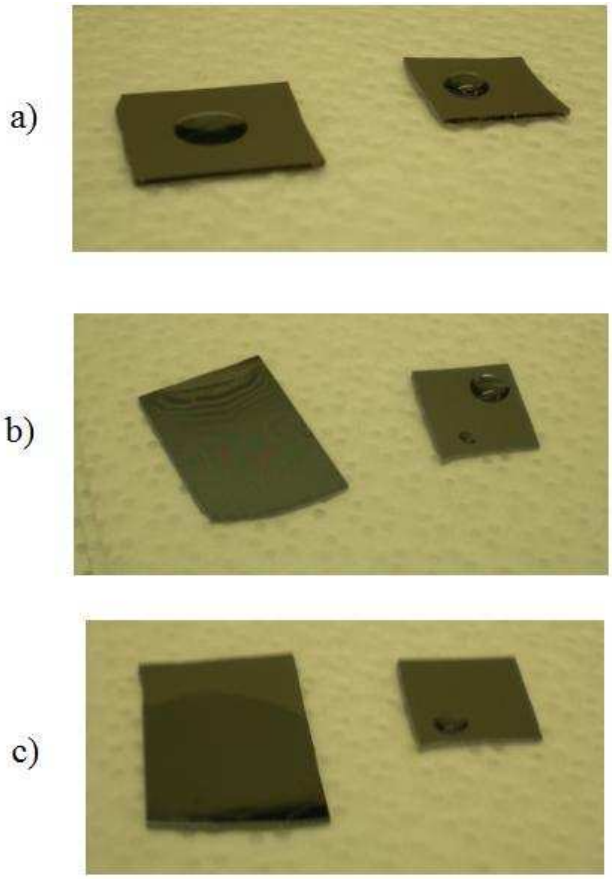

Fig. 5.6 shows the contact angle for a Si wafer (left) and a PFTS wafer (right) for a) pentanol, b) ethanol, and c) TFE.

5.2 Discussion of Alcohol Data[81]

The data was first examined from the viewpoint of a diffusive film spreading treatment of Brenner or Widom, and then from the viewpoint of diffusing islands. Table 5.1 presents slip times and spreading diffusion coefficients for the alcohols on the three substrates at a coverage of one monolayer. The spreading diffusion coefficients, which

are proportional to the slip time, are calculated using eq. (1.12) and (1.13) and range from 0.1 to 9 cm^2/s for the non-zero cases. The values are much higher than self-diffusion values of individual molecules, but quite consistent with the Brenner model numerical result that the refilling rate of an area scratched free of lubricate is orders of magnitude different from the self-diffusion coefficient of the molecules that comprise the film. TFE and pentanol on Al and TFE on PFTS show a value of zero for the spreading coefficient, or at least below the detection limit of the QCM. Pentanol and TFE show similar spreading coefficients on Si while ethanol exhibits higher values. Although TFE shows no mobility on PFTS, since PFTS is scraped off in tribological contact, the TFE might lubricate the silicon layer directly since mobility is indicated in this case.

Table 5.1: Summary of slip time and diffusion coefficient parameters at one monolayer coverage obtained from the QCM adsorption isotherm data. The slip times are obtained from Eq. (2) and (3), correcting for gas damping. The quantity D_s is the film spreading diffusion coefficient obtained from eq. (1.12) and (1.13) employing the slip times listed here for monolayer coverage. Non-zero values indicate high levels of sideways flow are possible if sufficient supply of film material is nearby. The quantity D_i defined by Eq. (6) is listed for hypothetical islands of the various alcohols of size $(0.1\ \mu m)^2$, indicative of the self-diffusion rate of individual islands. It is conceivable that lubrication may occur via this mechanism at very low coverages, where the notion of a spreading pressure for a complete monolayer is not applicable.

	PFTS			Si			Al		
	τ ns	D_s cm^2/s	D_i cm^2/s	τ ns	D_s cm^2/s	D_i cm^2/s	τ ns	D_s cm^2/s	D_i cm^2/s
Pentanol	6	1.2	$5x10^{-5}$	6	1.1	$5x10^{-5}$	0	0	0
Ethanol	4	1.1	$4x10^{-5}$	8.5	9	$1x10^{-4}$	0.5	0.1	$6x10^{-6}$
TFE	0	0	0	3.5	1.3	$2x10^{-5}$	0	0	0

To place the results in context, and to apply the Brenner criterion for contact replenishment, consider a typical MEMS tribometer, i.e. a silicon MEMS devices with rubbing contacts fabricated exclusively for studies of sliding contact. The estimated area of contact in this device is typically 1 μm^2 = $(10^{-4}$ cm$)^2$, or less, depending on surface roughness, with a maximum operational frequency of 100Hz. The removal rate parameter defined in Brenner's multiscale approach is $f\ A_c$ = (100Hz)$(10^{-4}$cm$)^2$ = 10^{-6} cm^2/s. Complete filling of the area scraped free should then require a self-diffusion coefficient that is 1000 times or more greater, or 10^{-3} cm^2/s, which is realistic for these systems. Alternatively, D_s from the QCM adsoption data ranges from 0.1 - 9 cm^2/s for the non-zero cases, which is in all cases large enough to refill the gap at the rate of 10^{-6} cm^2/s. These conditions imply mobility that is more than sufficient for each of these alcohols to replenish areas scraped free of the lubricant, but only if a sufficient supply of thicker or compressed liquid is present. Indeed, vapor phase replenishment of the film appears to be necessary for cases of pentanol lubrication of silicon: when the gas phase is removed, the sample rapidly fails. It is conceivable that all of the mobile lubricants will effectively lubricate a MEMS device, and that the variation in their respective spreading diffusion properties and slip times will only be manifested at temperatures other than room temperature.

Also listed in Table 5.1 are "island" diffusion coefficients obtained using eq. (1.11) employing the experimentally obtained slip times under the supposition of (0.1 $\mu m)^2$ islands, i.e. islands who edge length is about a tenth of that of the contact zone in a

MEMS asperity contact. This specific value for island size was postulated since only one island would be needed to diffuse into the contact area for lubrication to occur. The values were calculated for $D_i = \pi k_B T/(mN) = \pi k_B T/(\rho_2 A)$, from eq. (1.11) setting A = 10^{-10} cm^2 and employing the spacing of molecules in the island to be the same as that in the monolayer (45.9, 36.2 and 68.6 ng/cm^2 respectively for pentanol, ethanol and TFE). Realistically, islands could be smaller and there could be more than just one island, but this estimation is purely to compare values of different diffusion coefficients. Be advised that the slip time value is an average value for the entire surface, so some islands could be diffusing at a higher rate than the calculated values shown in table 5.1. These values are much lower than the values of D_s, but it remains conceivable that lubrication may occur via this mechanism at very low coverages, where the notion of a spreading pressure for a complete monolayer is not applicable. This mechanism, which appears strongest for ethanol films on silicon, but still viable for pentanol and TFE, is entirely distinct from that of a monolayer spreading back into an area of low film density, as it does not require a large reservoir of material of higher density.

5.3 Discussion of Alcohol post-pumpout

The results from Fig. 4.10 was the first insight of a SAM acting as a sponge or ballast holding onto the alcohol and possibly being a reservoir for lubricant to diffuse from and into the contact region. Since TFE was seen to be immobile on the surface of

PFTS, it follows that even if TFE were to stay adsorbed to the surface after pumpout occurs, TFE would not be able to diffuse anywhere. This was clearly witnessed on multiple occasions on multiple crystals. Therefore, if a PFTS-coated MEMS device was dosed with TFE, it would not be able to sustain lubrication since the diffusion coefficient would be zero.

The low slope in the isotherms of the Si data is indicative of a weakly attracted adsorbate to the surface. This weak attraction could be due to a heterogeneous hydrocarbon layer previously adsorbed to the surface lowering the attractive physisorption potential. This prompted more studies on a Si surface limiting the possibility of a heterogeneous hydrocarbon layer. A higher initial slope in the adsorption isotherm was witnessed indicating a higher attraction with the substrate, but a different behavior was seen during the pumpout. Despite the new hysteretic behavior of ethanol and pentanol adsorption on Si, the δ (1/Q) returned to its original value. Since the surface of the QCM is not perfectly flat (and neither is a MEMS contact) the alcohols could be adsorbing to areas of higher potential wells (pits, defects). This would explain why there is no slippage after most of the layer was removed. When the vapor is removed from the environment, lubrication of a Si MEMS device without the SAM would not occur despite the alcohols ability to stay adsorbed to the surface due to the lack of surface diffusion.

The island diffusion coefficient D_s calculated in table 5.2 show a drastic difference between Si vs. PFTS surfaces and TFE vs. pentanol and ethanol. The values of D_s for the non-zero cases are more than an order of magnitude larger than the removal

rate parameter of calculated for a MEMS device in section 5.2. It is possible that these islands of ethanol and pentanol on the surface could lubricate a MEMS device via surface diffusion even at low coverages and with no vapor replenishment.

Table 5.2 shows the slip time for each case after the alcohol was pumped away. Also computed were the values of the island diffusion coefficients D_i similar to table 5.1.

Table 5.2 shows the values for coverage and dissipation after the vapor has removed and the data has reached a steady value. The slip time is calculated from $\delta(1/Q) = 4\pi\tau\delta f$, and the island diffusion coefficients are calculated similarly to table 5.1.

	Si				PFTS			
	mono-layers	$\delta(1/Q)$ x 10^{-7}	τ (ns)	D_i (cm^2/s)	mono-layers	$\delta(1/Q)$ x 10^{-7}	τ (ns)	D_i (cm^2/s) x 10^{-5}
Ethanol	0 - ½	0	0	0	3/10	1.5	4	4.5
Pentanol	0 - ½	0	0	0	½	3.5 - 5	6-9	5.2 - 7.9
TFE	0	0	0	N/A	½	0	0	0

[81] B.P. Miller, J. Krim, J. Low Temp. Phys. 157, 252 (2009).

Chapter 6: TCP Results and Discussion[82]

6.1 TCP Results of manuscript in preparation

All samples were prepared in an identical manner at NCSU by myself and then distributed to the various measurement sites, keeping the QCM samples at NCSU for in-house measurements also taken by myself. Raw QCM data for TCP on Si and PFTS/Si is shown in Fig. 6.2 for a representative set. Also, raw data for TCP on Al and PFTS/Al is shown in Fig. 6.3 for a representative set. It should be noted that the frequency shifts for Al and Si cannot be compared to one another since the Al QCMs are 8MHz and the Si QCMs are 5MHz. A sample N_2 calibration is shown in Fig. 6.1 that depicts the inverse quality factor shift (obtained from the pressure data previously shown in chapter 5) as a function of inverse amplitude shift. Since the following TCP adsorptions will have no effect from a surrounding vapor, the relaxation time calculation (from eq. (5.2)) goes to 1 at high pressures. Hence, this calibration was performed at pressures from 100 -500 Torr. Multiplying the slope of 4.01×10^{-7} to future shifts in the inverse amplitude can be applied for this particularly tuned QCM to obtain inverse quality factor shifts.

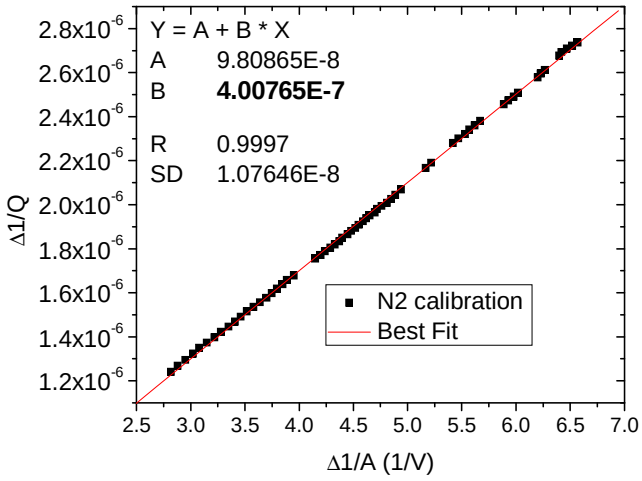

Fig. 6.1 shows the nitrogen calibration for the 8MHz QCM used in fig. 6.3. The slope of the best fit is the proportionality constant for future shifts in the amplitude to be converted to the change in the inverse quality factor. Taken from file: 3-19-07 n2.txt

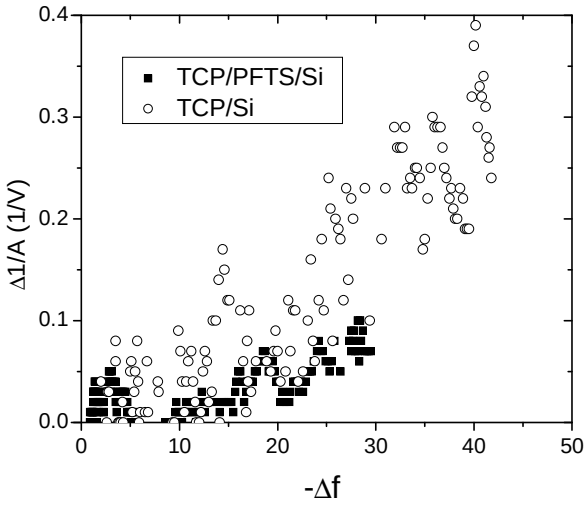

Fig. 6.2 shows the raw data taken with a 5MHz QCM of TCP adsorbed to PFTS/Si and Si substrates. The slope is proportional to the sliptime. Taken from file 5-27-07 TCP_PFTS.txt and 6-25-07 TCP_Si.txt

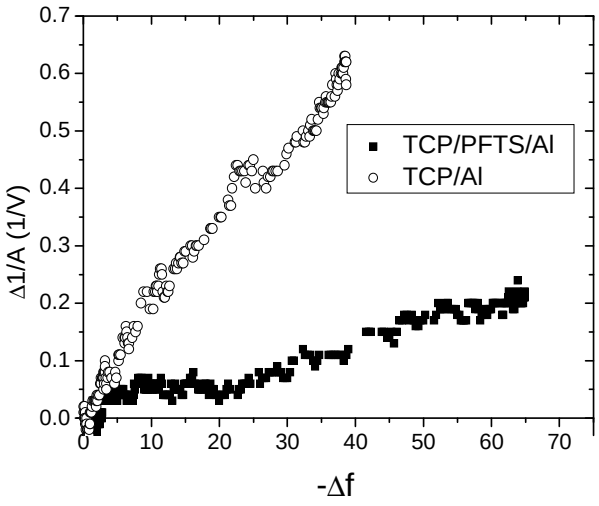

Fig. 6.3 shows the raw data taken with an 8MHz QCM of TCP adsorbed to PFTS/Al and Al substrates. The slope is proportional to the sliptime. Taken from file 3-19-07 TCP_PFTS.txt and 2-26-07 TCP_Al.txt

Analyzed QCM data illustrated a sample run of TCP on one of each of the four substrates (Fig. 6.4). The graph displays the inverse quality factor of the QCM vs. mass per unit area adsorbed to the surface, where the slope was proportional to the slip time. In Table 6.1 are the average slip time and coverages for each of the experiments. One set for TCP on SiO_2 and TCP on PFTS/SiO_2 was performed. Six deposition runs of TCP on PFTS/Al and two deposition runs of TCP onto Al were also performed. The slip time of TCP on SiO_2 set was in very good agreement with Neeyakorn's result of TCP on silicon possessing a native oxide[83]. The slip time of TCP on PFTS/SiO_2 and TCP on PFTS/Al should theoretically be equivalent and were, in fact, in acceptable agreement of 42.3% percent difference. The smaller slip time on PFTS/Al could be attributed to a rougher

substrate before PFTS deposition. Both showed less sliptime than TCP on their respective sublayers.

Table 6.1: Summary of experimental results of TCP slipping on four different substrates. The thicknesses are labeled in units of monolayers.

	Si		PFTS/Si		PFTS/Al		Al	
	thickness	τ (ns)	thickness	τ (ns)	thickness	τ (ns)	thickness	τ (ns)
TCP	3	0.90	3	0.26	4	0.15	3	0.55

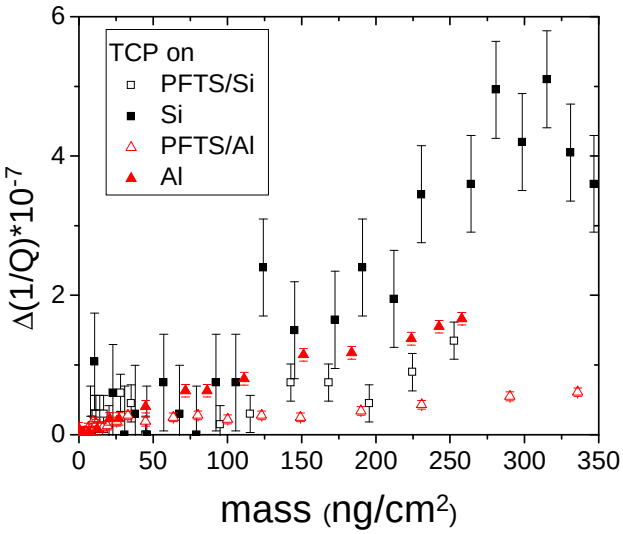

Fig. 6.4 Analyzed QCM results of TCP on Al, PFTS/Al, Si, and PFTS/Si converted to mass per unit area and the change in inverse quality factor. The slope is again proportional to the sliptime. The error bars show the standard deviation of the data to the best fit line. All results exhibit a non-zero sliptime indicating mobility.

AFM friction testing was performed using a single tip to facilitate friction comparisons between samples and tests. First, six unloading friction experiments were performed on the PFTS coated Si wafer and were repeated at another location on the wafer. Then, the sample was exchanged, and six unloading friction experiments were

performed on the TCP/PTFS coated Si wafer and were repeated at another location on the wafer. Finally, six unloading friction experiments were performed on a new location on the initial PFTS coated wafer. Typical plots of frictional force vs. normal load for one test (Fig. 6.5) showed that TCP increased adhesion (and therefore the total applied load[84]) compared to the PFTS layer alone. This increase of adhesion was attributed to capillary effects of a liquid TCP layer in the tip-sample contact. The slope of the averaged linear fits correspond to the approximate friction. Friction for the first two locations on the PFTS coated samples was 0.30±0.03 and on TCP/PFTS coated wafers, 0.13 ± 0.01. After returning to the initial PFTS samples, the friction coefficient was 0.20±0.04.

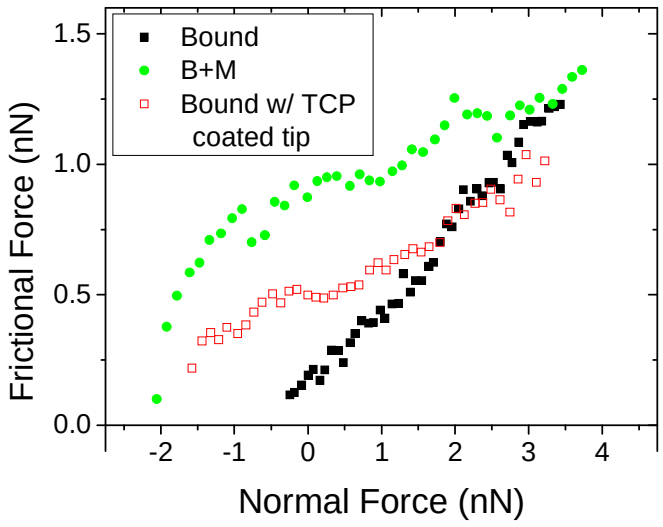

Fig. 6.5 Three characteristic AFM scans in lateral force mode showing a lower coefficient of friction with the mobile lubricant present. The bound with the TCP coated tip shows the mobility of the TCP to transfer to the AFM tip and continue to lubricate a bound-only specimen. Data recorded at NCSU by Matt Brukman. Samples prepared by myself at NCSU.

Microscopic friction experiments did not result in measurable differences between the friction of diamond against uncoated silicon and silicon coated with both PFTS and TCP layers; average friction coefficients were the same, ~0.075, within the measurement error. The average friction coefficient for both samples decreased from ~0.09 to ~0.075 by cycle 10 and was stable for the remainder of the test.

Reciprocating macroscopic sliding experiments revealed repeatable differences among uncoated silicon, the PFTS layer, and the TCP/PFTS layer shown in Fig. 6.6 with an amorphous Al_2O_3 (sapphire) counterface. The average friction coefficient for uncoated silicon began at ~0.24 for eight cycles, followed by an immediate increase in friction coefficient to 0.55-0.65 for the remaining cycles occurring concurrently with the generation of significant wear debris. The average friction coefficient of the bound PFTS layer began high at 0.5, and by cycle 2 was greater than 0.8, combined with the generation of debris. However, the average friction coefficient for the TCP/PFTS was less than 0.2 for between 30 – 80 cycles before increasing to ~0.5 with the generation of wear debris.

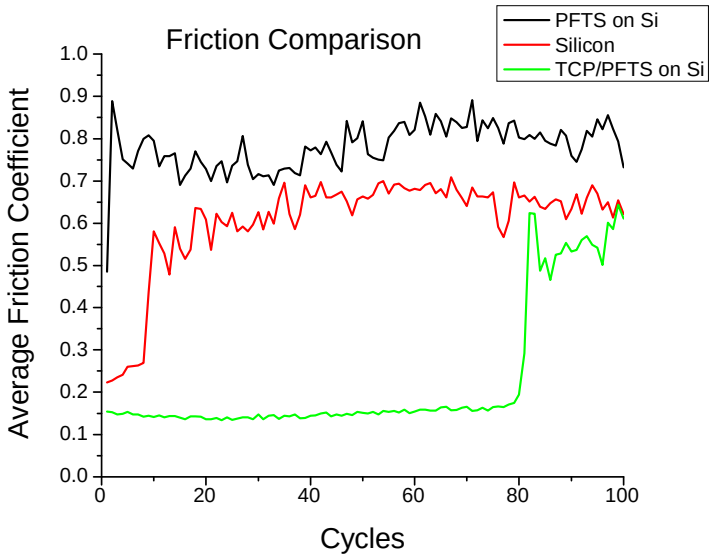

Fig. 6.6 Typical reciprocating macroscopic friction results from uncoated silicon (red), the bound PFTS layer on silicon (black), and the combined TCP/PFTS coating on silicon (green). Data taken by Nimel Theodore at Naval Research Laboratories (NRL). Samples prepared by myself at NCSU.

To better comprehend the frictional differences in the bound and mobile coating observed in microscopic and macroscopic testing, a separate macroscopic experiment was executed to examine the effect of increasing the mean Hertzian contact stress. Loads of 0.5 N, 1 N, and 2 N were applied to a sapphire counterface to produce mean Hertzian contact stresses of 0.35 GPa, 0.44 GPa, and 0.56 GPa, respectively shown in Fig. 6.7. Values used for sapphire and silicon of the Young's modulus were 400 and 160 GPa, respectively, and of the poisson ratio were and 0.29 and 0.27, respectively. With a 0.56 GPa mean contact stress, the average friction increased from 0.27 to 0.55 within 5 cycles. With a 0.44 GPa mean contact stress, the friction remained below 0.2 for 10 cycles, increased sharply to 0.55 during cycle 11, but then recovered to below 0.2 for 15 more

cycles before incrementally increasing up to 0.60. With a 0.35 GPa mean contact stress, the friction remained low for 40 cycles before incrementally increasing similarly to the previous test.

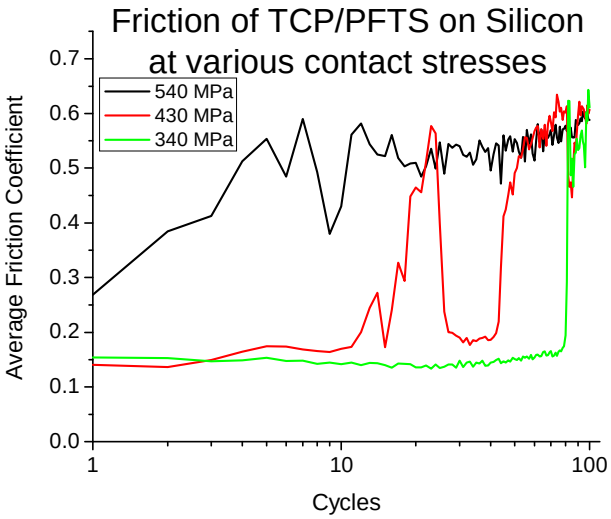

Fig. 6.7 Typical reciprocating macroscopic friction results from the combined TCP/PFTS coating on silicon as the average Hertzian contact stress is increased by raising the applied load from 0.5 N (blue), to 1 N (red) and 2 N (black). The number of cycles at low friction (< 0.2) decreases from about 80 cycles at 340 MPa to 15 cycles at 430 MPa to 0 cycles at 540 MPa. After possessing high friction for ~10 cycles, the friction during the 430 MPa test does recover to low friction for an additional 15 cycles before ultimately remaining at high friction. Data taken by Nimel Theodore at NRL. Samples prepared by myself at NCSU.

6.2 Discussion of manuscript in preparation

Adhesion and poor tribological properties lead to shortened MEMS device lifetimes, which limit their reliability and utility. Currently, one way to minimize

adhesion during the fabrication of MEMS is the addition of a SAM layer to the silicon surface[85]. Others have tried to lower the friction and wear while increasing device lifetimes with that same SAM layer. However, our AFM and macrotribometer results showed that a SAM, PFTS, alone does not provide a low friction and wear contact, agreeing with Hook's conclusion[86]. AFM results determined a high friction coefficient of 0.30 up to its load limit of 4 nN. Macroscopic tests showed that PFTS had worse tribological behavior as uncoated silicon. The friction of PFTS was greater than 0.5 from its onset with the formation of debris in the wear tack; uncoated silicon had friction lower than 0.5 for 8 cycles before the generation of debris.

The addition of a lubricant to a SAM can potentially increase the tribological performance by decreasing friction and wear over a longer period of time than without it. Our AFM and macroscopic tribometry results supported this claim despite the AFM measuring an increase in adhesion. The x-intercepts from the AFM data (Fig. 6.5) showed that adhesion from the PFTS layer was approximately 0.5 nN, and the addition of TCP to PFTS *increased* adhesion to 2 nN. The PFTS layer had a high friction coefficient of 0.30, calculated from the slope of lateral force versus normal force plot and a *decrease* in the friction coefficient to 0.13 with the addition of TCP. Therefore, the mechanism for friction reduction by the addition of TCP is not due to a decrease in adhesion. Since adhesion is a failure mechanism in a MEMS device, the ideal amount of TCP, which will lower the coefficient of friction but limit adhesion, has yet to be determined.

In the macroscale reciprocating tribometry tests on the PFTS layer on silicon, friction was high (>0.5) and significant silicon debris was generated quickly, similar to tests run on uncoated silicon. The addition of TCP, however, protected the underlying silicon substrate and reduced friction for the longest period of time for all of the surface treatments examined here. Thus, these macro-scale tests confirmed that TCP is a lubricant that lowers friction and wear.

Krim et al. have shown that favorable macroscopic tribological properties from a mobile lubricant corresponded to a non-zero sliptime value on a QCM; poor macroscopic tribological properties occurred when QCM sliptime values were zero[87,88]. Our QCM measurements determined that TCP possessed a non-zero sliptime on PFTS, and so TCP may in fact be mobile on the surface of PFTS, which is applicable to MEMS that require high frequencies of oscillation. One example of its mobilty was that the final PFTS data set in the AFM experiment had behavior similar to the TCP/PFTS set despite no TCP present on the sample. This effect was attributed to TCP transferred to the AFM tip from the TCP/PFTS sample, which resulted in lower friction when that same tip was used on the previous PFTS surface. This transfer of TCP from sample to tip also exhibited its mobility. Another example of mobility was in the variable load macroscopic test. Specifically, the test at 0.44 GPa demonstrated that the TCP/PFTS could in fact heal itself to low friction after exhibiting high friction. This replenishment indicated that TCP was transferred from an area of high to low lubricant concentration suggesting mobility. With mobility TCP could move into a region that was wiped clear of lubricant.

To quantify the effect of mobility, Brenner's lubrication model was used. According to Brenner's windshield wiper model, the steady-state center lubricant concentration is a function of three parameters: the contact area, frequency of oscillation, and diffusion coefficient. For a MEMS device, using a 1 μm^2 contact area and a simulated diffusion coefficient of 62.4×10^{-5} cm^2/s for TCP on a SAM[89], the steady-state center lubricant concentration of TCP on PFTS was 55%, assuming that 10% of the lubricant was removed per stroke and that the maximum oscillation frequency was 1000 Hz. The contact area is an integral part of this model, and as that value increases, the steady-state center concentration of lubricant will decrease to an amount insufficient for favorable tribological performance. Our results supported this claim to a certain extent. When the loads during macrscopic tests were incrementally raised – thereby increasing the applied contact area and stress – while holding the oscillation frequency and diffusion coefficient constant, the protective and lubricating performance of the combined TCP/PFTS layer deteriorated, corresponding to a smaller steady-state center concentration of TCP as predicted by the model.

However, comparing the tribological results from the different length scales did not corporately fit into the model. The oscillation frequency and the diffusion coefficient could be the same despite differences in length scale like those in an AFM, microtribometer, and macrotribometer. If these values are fixed, the sole parameter controlling lubricant replenishment and therefore the tribological properties is contact area. Hence, according to this model, macroscopic tests which utilized a counterface

almost 3 orders of magnitude greater than the microscopic tests and almost 5 orders of magnitude greater than the AFM should have possessed the "worst" friction properties. However, our results showed better tribological properties of TCP on PFTS in macroscale tests than in microscale tests where friction was the same on TCP/PFTS and PFTS by itself. Moreover, the average contact stress of the microtribometry tests was 2 GPa, whereas the mean contact stress for the macrotribometry tests was only 0.34 GPa. These results showed that the bound PFTS and mobile TCP coatings may not be effective in a high contact stress environment at these length scales. However, despite applying a similar maximum mean contact stress in the AFM tests (1.8 GPa in the AFM compared to 2 GPa in the microtribometer), the friction of the TCP/PFTS layer was lower by a factor of 2.5 compared to that of PFTS. In the case of TCP/PFTS with the AFM, the Brenner model explains why lubrication occurs at the nanoscale via surface diffusion. Using a frequency of oscillation of 1Hz, a liberal area of $1000nm^2$, and the same diffusion coefficient of 62.4×10^{-5} cm^2/s, one can obtain an S parameter on the order of 10^{-8}. In this case the surface diffusion of TCP on a SAM is more than enough by orders of magnitude to replenish a 1Hz contact in an AFM.

Since the friction measurements of TCP on PFTS from millimeter, micrometer, and nanometer dimensions produced results sorted by contact stress, we propose that in general, the contact stress along with the corresponding contact size should be accounted for when characterizing the tribological properties of lubricants at different length scales.

Table 6.2 summarizes the results of these studies. A (–) indicates friction was lowered, and a 0 indicates friction remained constant with the addition of TCP to a PFTS contact.

Table 6.2 summarizes the length, time, and pressure scales at which the data was recorded with the result of the addition of TCP to the PFTS layer.

	QCM	AFM	Microtribometer	Macrotribometer
Length scale	atomic	nm	μm	mm
Contact frequency	N/A	1Hz	0.5Hz	0.2Hz
Contact pressure	N/A	1.8GPa	2GPa	0.35GPa
Friction with addition of TCP	–	–	0	–

6.3 Results of macroscopic reciprocating tribometer tests of TCP on Si

Additionally, QCM tests shown in fig. 6.4 measured a higher sliptime for just TCP compared to TCP/PFTS on aluminum and silicon oxide. Higher QCM sliptimes indicate greater mobility that is also proportional to a higher diffusion coefficient. Thus, according to the model, TCP without the presence of PFTS would possess the same steady-state center concentrations even at higher oscillation frequencies, and so it could lubricate even better than the combined TCP/PFTS coating. So, the push and pull of mobility and adhesion of TCP alone on silicon was investigated.

Some preliminary reciprocating tests of TCP on Si (without PFTS) were performed with a sapphire counterface, similar to fig. 6.6, showing no wear formation or high friction events up to 1000 cycles. These reciprocating tribometer and QCM results prompted more work investigating the mobility of TCP on Si. Fig. 6.8 shows the friction results of a silicon counterface on TCP deposited onto a bare Si wafer varying with load.

The results did not show a clear regime where lubrication occurred below a certain contact stress and lubrication did not occur above said contact stress. However, there was a definite trend showing a higher probability of failure at larger contact pressures. These results were repeated for different monolayer coverages (2 – 25 monolayers) and showed no dependence.

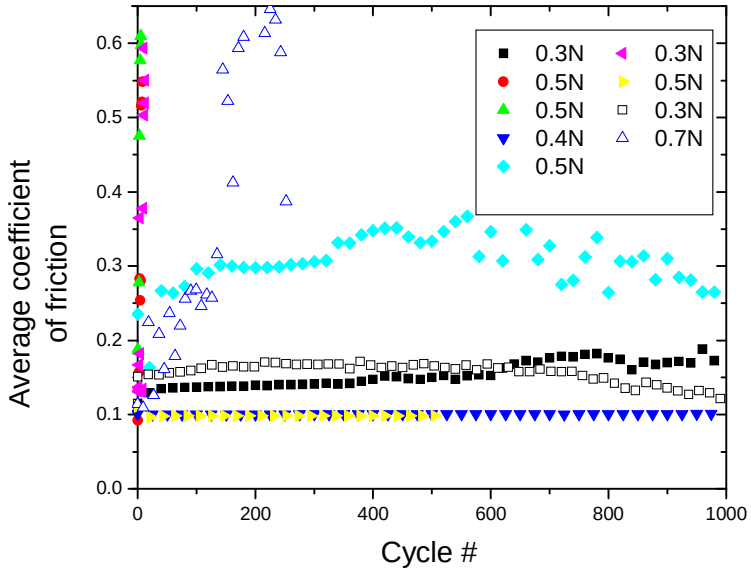

Fig. 6.8 shows the coefficient of friction (COF) for various normal loads of a Si counterface reciprocating on a Si wafer deposited with TCP. Any COF above 0.25 was characterized as failure showing clear wear debris. This data was taken by myself at NRL and prepared by myself at NCSU.

TCP-coated Si counterfaces on TCP-coated Si wafers were used in Fig. 6.9 in contrast to a bare Si counterface. These results in contrast to Fig. 6.8 show a higher and more clear cutoff point where lubrication ceases to occur for normal load of 1N

(corresponding to 0.35 GPa Hertzian contact stress). In addition, similarly to Fig. 6.8 there was no dependence on lubricant thickness in the range studied.

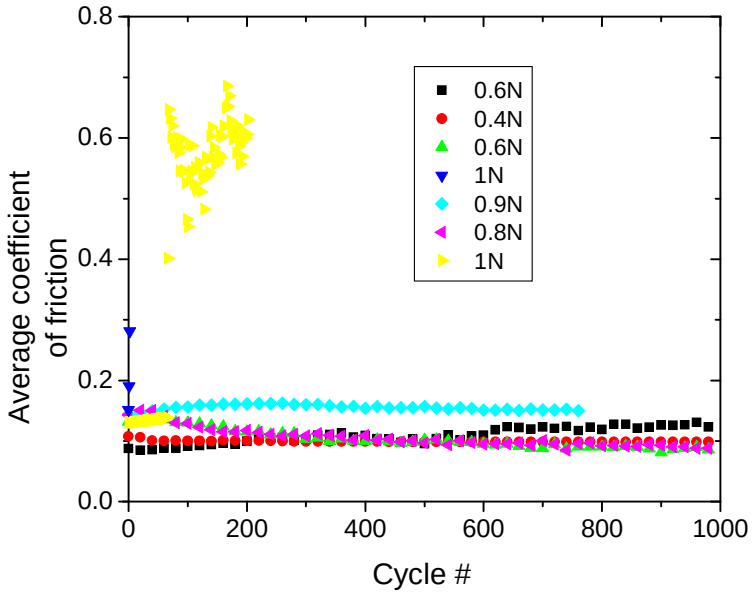

Fig. 6.9 shows the coefficient of friction for TCP-coated Si counterfaces on TCP-coated Si wafers at various loads. All COF below 0.2 were characterized with no noticeable wear. This data was taken by myself at NRL and prepared by myself at NCSU.

An optical image shown in Fig. 6.10 depicts the wear track of a failed test of TCP on Si. Noticeable wear can be seen at the end of the track, and wear scars are visible inside the track. Wear debris and scar are also visible on the silicon counterface. Fig. 6.11 shows an optical image of the successful, wear-free track of a 1000 cycle test.

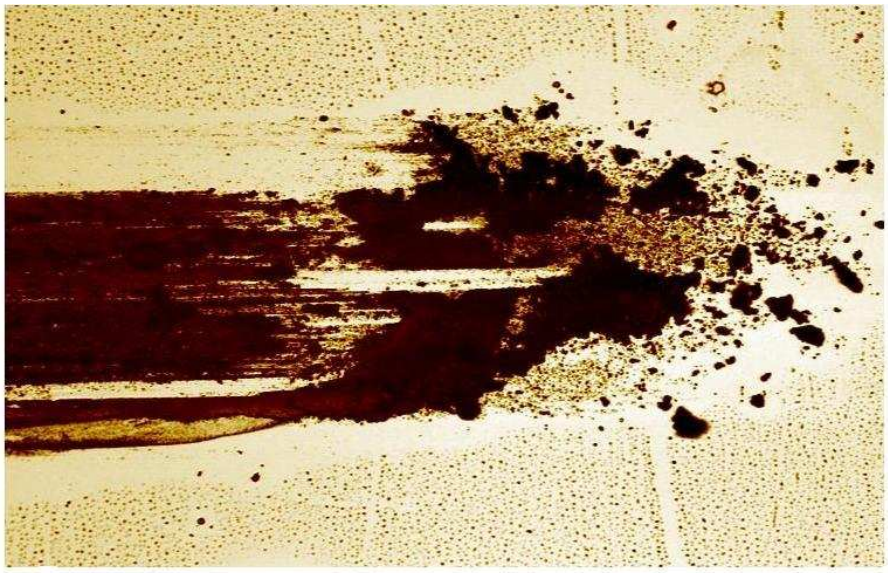

Fig. 6.10 taken at 10X shows the wear track of a failed test. Wear scars can be seen inside the track, and debris is easily seen at the end of the track. This image was taken by myself at NRL with a sample prepared by myself at NCSU.

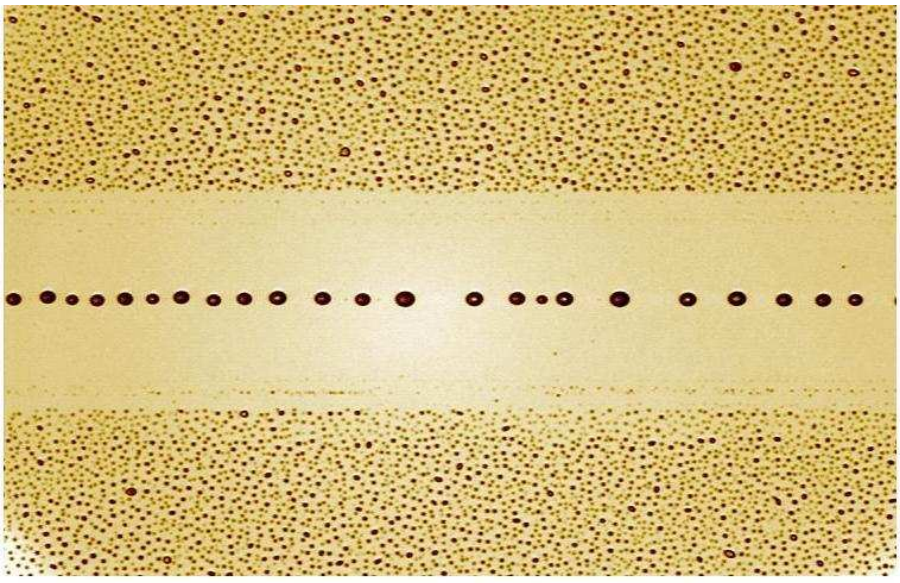

Fig. 6.11 taken at 20X shows the wear track of a 1000 cycle test in which the COF stayed below 0.2 for the entire test. The absence of wear is clearly seen, but dewetting inside and outside the wear track is observed. This image was taken by myself at NRL with a sample prepared by myself at NCSU.

6.4 Discussion of macroscopic reciprocating tribometer tests of TCP on Si

To make a connection with surface diffusion to predicting MEMS effectiveness one must isolate surface diffusion. The first variable is the contact stress. There was a clear dependence on contact stress shown in Fig. 6.7. Keeping the Hertzian contact pressure below that critical range of 430 MPa ensured a direct comparison between a TCP/Si contact and a TCP/PFTS contact. Two different normal forces were used to produce the same Hertzian contact pressure for the two different counterfaces due to their differing Young's moduli. The result that TCP lubricates Si better than PFTS is consistent with both counterfaces. Two separate tests were witnessed with a sapphire counterface having indefinite failure times on a TCP/Si substrate similar to Si counterface on TCP/Si. Conversely, two results showing failure below 100 tests were witnessed with a Si counterface on a TCP/PFTS substrate similar to sapphire counterface on TCP/PFTS. Calculating the removal rate parameter $f A_c$ from Brenner's model requires knowledge of the area of contact. Hertzian contact radius a_o was calculated using

$$a_o = \left(\frac{3F_N R}{4E^*} \right)^{1/3}, \qquad \frac{1}{E^*} = \frac{1-\nu_1^2}{E_1} + \frac{1-\nu_2^2}{E_2}. \tag{6.1}$$

F_N is the normal force, R is the radius of curvature of the counterface, E^* is the combined Young's moduli for the two contacts, and ν is the respective Poisson ratio. A 2mm track with a 4 second period yields $f A_c$ = (0.5Hz)(1.42×10^{-5} cm^2) = 7.13×10^{-6} cm^2/s using a sapphire counterface at 0.5N load. Using the same diffusion coefficient from section 6.2

of 62.4×10^{-5} cm^2/s for TCP on a SAM, one obtains a scaling parameter *S* of 1.14×10^{-2}. For a Si counterface at 1N load one obtains 1.43×10^{-5} cm^2/s (due to a larger area of contact) for the removal rate parameter and 2.16×10^{-3} cm^2/s for the diffusion coefficient from an increase in the slip time by a factor of 3.5. This yields an *S* parameter of 6.64×10^{-3} cm^2/s. For 100% of the lubricant removed per stroke a steady state center concentration of 86% and 75% for TCP/Si and TCP/PFTS, respectively.

These values are very high and could potentially be lower with a smaller value for the diffusion coefficient. It was seen in a modeling effort of TCP on a defected SAM that the TCP had a propensity to remain near a defect[90]. In a real life situation the surface of a SAM cannot be more uniform than the model, so the actual diffusion coefficient could be smaller. These center concentrations could also be lower with a higher frequency of oscillation. The nature of a reciprocating tribometer does not keep the frequency between contacts constant. When the counterface reaches the endpoint it returns instantly making the time between contacts near the endpoints much larger than the middle. This could account for the larger calculated center concentrations. Those values of TCP/Si vs. TCP/PFTS are also not drastically different from each other, but that difference is offset due to the larger area of the Si/Si contact compared to the sapphire/Si contact. Despite the larger removal rate parameter with the Si/Si contact, the larger diffusion coefficient for TCP/Si is large enough to overcome that difference and therefore possess a larger center concentration enabling longer lifetimes without the presence of PFTS due to a higher mobility of TCP on Si than PFTS.

The dewetting inside and outside the wear track seen in Fig. 6.11 is a concern regarding the mechanism of lubricant replenishment. The question arises that TCP will not diffuse around on the surface since the dewetting prevents mobility. An interesting result from these experiments is that TCP *still lubricates* even a low surface coverage where no dewetting is seen to occur. This implies a situation akin to Fig. 1.4(b) and not 1.4(c) where partial dewetting occurs after a few uniform monolayers in contrast to complete dewetting occurring with the absence of any monolayer formation. The lack of a dependence on coverage implies that the first couple of monolayers are indeed diffusing around the surface and the dewetting is a by-product not affecting lubrication. Hence, surface diffusion is still the mechanism for lubrication.

---

[82] Miller, B.P., Theodore, N.T., Brukman, M.J., Wahl, K.J., Krim, J. Trib. Lett. Submitted.

[83] Neeyakorn, W., Varma, M., Jaye, C., Burnette, J. E., Lee, S. M., Nemanich, R. J., Grant, C. S., Krim, J.: Dynamics of Vapor-Phase Organophosphates on Silicon and OTS. Trib Lett 27, 269-276 (2007).

[84] Carpick, R.W., Agrait, N., Ogletree, D.F., Salmeron, M.: Variation of the interfacial shear strength and adhesion of a nanometer-sized contact. Langmuir 12, 3334 (1996).

[85] Maboudian, R., Ashurst, W. R., Carraro C.: Tribological challenges in micromechanical systems. Trib Lett 12, 95-100 (2002).

[86] Hook, D.A., Dugger, M.T., Krim. J.: Monolayer Degradation in MEMS friction devices. J App Phys 104, 034303 (2008).

[87] Abdelmaksoud, M., Bender, J., Krim, J.: Bridging the Gap between Macro- and Nanotribology: A Quartz Crystal Microbalance Study of Tricresylphosphate Uptake on Metal and Oxide Surfaces. Phys Rev Lett 92, 176101 (2004).

[88] Abdelmaksoud, M., Bender, J., Krim, J.: Nanotribology of a Vapor-Phase Lubricant: A Quartz Crystal Microbalance Study of Tricresylphosphate (TCP) Uptake on Iron and Chromium. Trib Lett 13, 179-186 (2002).

[89] D.W. Brenner, D.L. Irving, A.I. Kingon, C.W. Padgett, J. Krim. Lang. 23, 9253 (2007).

[90] Private Communication with D.W. Brenner and D.L. Irving.

Chapter 7: Conclusions and Future Work

7.1 Conclusion

Experimental tests using a QCM, reciprocating tribometer, microtribometer, and an AFM were performed to study the different types of surface diffusion on substrates of interest to MEMS. We used a novel way to determine the diffusion coefficient by measuring the slip time from a QCM. This diffusion coefficient can be used in Brenner's model of lubrication involving surface replenishment of a cyclical contact. Three different types of diffusion coefficients were used in predicting MEMS effectiveness via surface replenishment. The traditional single particle diffusion D deals with the corrugated potential energy barrier resulting from the surface on an atomic scale. The island diffusion coefficient D_i spawns from the experimental observation of gold nanoclusters on graphite and deals with the islands of particles moving together across the surface. The spreading diffusion coefficient D_s involves a layer of mobile particles spreading into a region of lower coverage through internal pressure gradients. This diffusion coefficient can be viewed similarly to a droplet of liquid spreading into a thin film on a surface, which it is known to wet. Each of these diffusion coefficients have the same units (cm^2/s) and will be used in different, appropriate situations.

Adsorption of TCP onto a QCM and using Fig. 1.4 as a reference show that TCP partially wets the surface. This means that TCP is forming a full monolayer before

wetting occurs. The island diffusion coefficient D_i is thus not accurate for this particular case since there is at least a full monolayer of TCP present and lubrication is not coverage dependent. Since the spreading diffusion coefficient D_s is calculated through pressure and coverage measurements and TCP was deposited through thermal evaporation, D_s cannot be implemented for this case. The single particle diffusion can be inferred from the nanomechanics of the QCM compared to the known behavior of a single particle of TCP on a SAM from Brenner's simulations. For TCP on PFTS the discrepancy between Al and Si albeit small was attributed to a larger surface roughness. Fitting these results to a reciprocating tribometer and using Brenner's model for surface replenishment yielded a clear difference in steady-state center concentration of lubricant for the two different counterfaces compared to one another. Table 7.1 shows values for the single particle diffusion coefficient D of TCP on three different substrates calculated from the ratios of the slip time and the theoretically modeled value of 62.4×10^{-5} cm^2/s for TCP on a SAM. The higher value of D for TCP on Si corresponds to a higher steady-state center concentration and, thus, better tribological performance.

Table 7.1 shows the single particle diffusion coefficient of TCP on various substrates.

	TCP on Si	TCP on PFTS/Si	TCP on PFTS/Al
Diffusion Coefficient cm^2/s	2.16×10^{-3}	6.24×10^{-4}	3.6×10^{-4}

Table 7.2 shows values for D_s at one monolayer coverage in an environment of its own vapor for the three alcohols on three different surfaces relevant to MEMS. Despite the lack of mobility with TFE on PFTS, lubrication should still occur with a MEMS device due to replenishment occurring from the vapor phase. Once the vapor is removed, however, and surface coverage decreases to sub-monolayer levels, vapor replenishment is discarded and spreading diffusion is no longer valid. Since surface coverage post vapor removal is assumed to be non-uniform, island diffusion takes over. The lack of mobility of TFE on PFTS is now pertinent to lubrication; therefore failure in a MEMS device is predicted.

Table 7.2 shows the spreading diffusion coefficient at one monolayer and the island diffusion coefficient at roughly half a monolayer post vapor removal. The N/A signifies a complete removal of the surface adsorbates, and thus no surface diffusion is possible.

	Pentanol		Ethanol		TFE	
	Si	PFTS	Si	PFTS	Si	PFTS
Ds (cm^2/s)	1.1	1.2	9	1.1	1.3	0
Di (cm^2/s)	N/A	6.5×10^{-5}	N/A	4.5×10^{-5}	N/A	0

The main caveat with the Brenner model involves the contact stress. From tests involving different contact sizes I witnessed a dependence on contact pressures contradictory to the Brenner model. Specifically, the microtribometer possessed a smaller contact size and therefore less area needed for the lubricant to diffuse into, but did not lubricate a TCP or TCP/PFTS contact due to its larger contact stress compared to

the macroscale tribometer, which was lubricated. Contrastingly, the smallest contact having a similar contact stress to the failed microtribometer did show lubrication with the addition of TCP. It was found that the Brenner model works for contact stresses below a critical failure limit.

7.2 Preliminary studies

Some preliminary studies of ethanol uptake onto the surface of a Au QCM with a fluorinated thiol (instead of a silane on Si) previously chemisorbed to the surface. Thiols are known to form more tightly packed monolayers than silanes. This QCM data set showed significantly less adsorption on a thiol surface. There was a coverage of ½ monolayer at 16 Torr of ethanol onto the Thiol/Au QCM compared to 1 monolayer on PFTS/Al and 1½ monolayers of ethanol on UV Ozone clean Si. In addition, there was no hysteresis during the pumpout of ethanol for the coverage or dissipation indicating full removal of the layer in contrast to both PFTS and Si.

7.3 Future Work

For liquid lubrication to occur under conditions needed for MEMS contacts the liquid lubricant must possess these characteristics. Since an environment of gas is not feasible for MEMS, the calculated diffusion coefficient must be high enough to sustain

lubrication via the Brenner model. The lubricant must have a low vapor pressure to ensure surface coverage. The lubricant must also wet the surface so replenishment can occur, and the lubricant must not increase the adhesion. TCP was an ideal candidate except for the increase of adhesion, which is not enough to change macroscale tribometry tests, but is high enough to cause stiction in a MEMS friction tester.

To better understand the relationship between the diffusion coefficient and the slip time, more tests must be performed comparing different factors in the scaling parameter. The first method would be to vary the frequency and area of contact of the reciprocating tribometer to fit Brenner's model. This would lock in on a more accurate value for the fraction of lubricant removed per stroke and center concentration needed for lubrication. The second method would be to obtain slip times of an adsorbate on different surfaces and compare that adsorbate's ability to lubricate a reciprocating contact. This method would elucidate a direct comparison from the slip time to a diffusion coefficient without the need for modeling every case. Finally, future studies on a MEMS device are paramount for being able to use a QCM for quick and efficient ways to predict MEMS effectiveness.